Aus der Klinik für Nephrologie und Rheumatologie

(Prof. Dr. med. M. Zeisberg)

der Medizinischen Fakultät der Universität Göttingen

Oxidative stress in the pathogenesis of renal injury: the effect of the antioxidant danshensu on renal fibrosis

INAUGURAL-DISSERTATION

zur Erlangung des Doktorgrades

der Medizinischen Fakultät der

Georg-August-Universität zu Göttingen

vorgelegt von

Hannah Maria Neuenhofer

aus

San Francisco

Göttingen 2022

Dekan: Prof. Dr. med. W. Brück

Betreuungsausschuss

Betreuer: Prof. Dr. rer. nat. H. Dihazi

Ko-Betreuer: Prof. Dr. rer. nat. M. Müller

Prüfungskommission

Referent Prof. Dr. rer. nat. H. Dihazi

Ko-Referent:

Drittreferent/in:

Datum der mündlichen Prüfung:

Hiermit erkläre ich, die Dissertation mit dem Titel „Oxidative stress in the pathogenesis of renal injury: the effect of the antioxidant danshensu on renal fibrosis“ eigenständig angefertigt und keine anderen als die von mir angegebenen Quellen und Hilfsmittel verwendet zu haben.

Göttingen, den …… ……

(Unterschrift)

Table of Contents

List of Figures

List of Tables

List of Abbreviations

α-SMA	Alpha-smooth muscle actin
AGE	Advanced glycation end-product
APS	Ammonium persulfate
BMP	Bone morphogenetic protein
BSA	Bovine serum albumin
CHAPS	3-((3-cholamidopropyl) dimethylammonio)-1-propanesulfonate
CKD	Chronic kidney disease
CM-H_2DCFDA	Chloromethyl dichlorodihydrofluorescein diacetate acetyl ester
Col1	Collagen 1
DAPI	4',6'-diamidino-2-phenylindole
DCF	2',7' dichlorodihydrofluorescein
ddH_2O	Double-distilled water
DMEM	Dulbecco's Modified Eagle Medium
DMSO	Dimethyl sulfoxide
DSS	Danshensu
DTT	Dithiothreitol
ECM	Extracellular matrix
EMT	Epithelial mesenchymal transition
FACS	Fluorescence-activated cell sorting
FCS	Fetal calf serum
FN1	Fibronectin 1
GADPH	Glyceraldehyde 3-phosphate dehydrogenase
GFR	Glomerular filtration rate
HBSS	Hank's balanced salt solution
MTT	3-(4,5-dimethylthiazol-2-yl)-2,5-diphenyltetrazolium bromide
NADPH	Nicotinamide adenine dinucleotide phosphate
NO	Nitrogen monoxide
NF-κB	Nuclear factor kappa B
Nrf2	Nuclear factor erythroid 2-related factor 2
PAS	Periodic acid schiff
PI	Propidium iodide
pSMAD2	Phospho-SMA (small body size)/ MAD (mothers against decapentaplegic)
RAAS	Renin-angiotensine-aldosterone system
ROS	Reactive oxygen species
rpm	Revolutions per minute

RRT	Renal replacement therapy
rt-PCR	Real-time polymerase chain reaction
SOD	Superoxide dismutase
SDS-PAGE	Sodium dodecyl sulfate polyacrylamide gel electrophoresis
TDS	Tubular damage score
TEMED	Tetramethylethylendiamine
TGF-β	Transforming growth factor beta
UUO	Unilateral ureteral obstruction
VIM	Vimentin

1 Introduction

Chronic kidney disease (CKD) describes the long-term, progressive failure of renal function due to processes damaging the parenchyma, affecting almost every tenth person worldwide (Hill et al. 2016). CKD is defined as a < 60 ml/min/1.73 m^2 measurable glomerular filtration rate (GFR), meaning the amount of blood filtered by the kidneys in a certain time period, or the presence of kidney damage parameters such as albuminuria, electrolyte abnormalities, or histological irregularities, verifiable over a period of at least three months (Levey et al. 2003). This definition of CKD based on clinical chemistry is independent of the underlying etiologies, whereby most of them merge in the development of renal tissue fibrosis as common manifestation (Liu 2006). Clinically, the furtive nature of the disease makes it difficult for patients to grasp its severity, because unlike a broken bone, patients seldom experience symptoms until the disease has advanced to a terminal stage. This problem of low disease awareness is verified by data revealing that less than 30% of patients with stage 4 – 5 CKD have ever seen a nephrologist, and this rate has not improved in recent years (Jha et al. 2013; Saran et al. 2020). However, an early diagnosis is vital to prevent fibrosis and thus disease progression to irreversible kidney failure, currently treated through complex renal replacement therapy (RRT) such as hemodialysis, peritoneal dialysis, or allogenic kidney transplantation (Levey et al. 2003). Treatment in early stages primarily focuses on minimizing risk factors, calling for a broader spectrum of treatment options. Danshensu (DSS), a representative of traditional Chinese medicine, is such a promising treatment candidate, as it has already been shown to reduce sclerosis and fibrosis development in other diseases such as arteriosclerosis (Chan et al. 2004), cardiac fibrosis (Lu et al. 2014), and hepatic fibrosis (Cao et al. 2019).

1.1 Structure and function of the healthy kidney

Consideration of the anatomy and physiology of a healthy kidney allows an understanding of the pathological processes occurring in CKD. Anatomically, the two kidneys are situated in the retroperitoneal space. Macroscopically, they are divided into an outer cortex and an inner medulla (Figure 1A). Each kidney is perfused by a renal artery emerging from the abdominal aorta with its venous outflow merging into the inferior vena cava. After several arterial divisions, one afferent arteriole finally enters the glomerulus, which, together with the subsequent system of tubules, forms the nephron, the smallest functional unit of the kidney. Filtration occurs in the glomerulus across the endothelium of the glomerular capillaries and through the podocyte filter with its basement membrane, producing up to 150 l of ultra-filtrated, primary urine daily. The

primary urine enters the Bowman capsule and then the system of tubules (Figure 1B), which includes the proximal and distal tubules, the loop of Henle, and the collecting duct. Through osmosis as well as active and passive transport, molecules such as water, glucose, amino acids, and electrolytes are either reabsorbed or excreted across the tubule epithelium until the collecting duct is reached. The collecting ducts ultimately merge into the renal pelvis, and from here, the urine enters the ureter and passes through the lower urinary tract (Gueutin et al. 2012; Scott and Quaggin 2015).

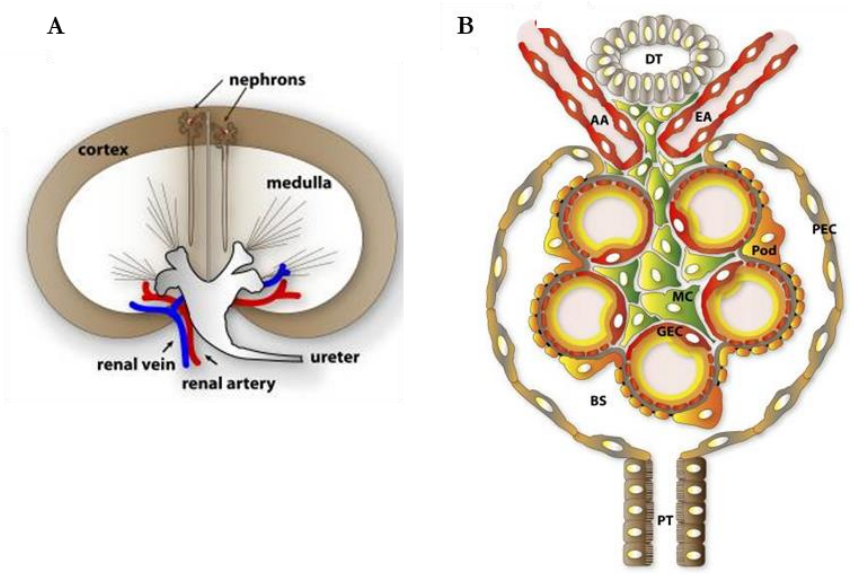

Figure 1: Macroscopic and microscopic anatomy of the kidney. A macroscopic presentation of the kidney (A) shows the division of the cortex and medulla, location of the renal pelvis and ureter, as well as the main supplying vessels, the renal artery and renal vein. The renal glomerulus (B), together with the subsequent system of tubules, builds a nephron, the smallest individually functioning unit of the kidney. The labels are defined as follows: DT= distal tubule; AA=afferent arteriole; EA= efferent arteriole; MC= mesangial cell; Pod= podocyte; GEC= glomerular endothelial cell; PEC= parietal epithelial cell; BS= Bowman space; PT= proximal tubule. (CC BY-NC-SA 3.0; Scott and Quaggin 2015).

Physiologically, the kidneys play a central role in maintaining homeostasis within the human body and are involved in many complex metabolic systems, thus providing a realistic assessment of the clinical consequences of CKD and renal failure. One if the main renal functions is the elimination of water and water-soluble substances, such as metabolites of medication and by-products of metabolic pathways, like urea and uric acid, through the production and excretion of urine. Alongside the maintenance of electrolyte and liquid homeostasis, the kidneys are also responsible for upholding a physiological systemic pH-value through the absorption and elimination of protons (H^+) and bicarbonate (HCO_3^-). Furthermore, the kidneys contribute to blood pressure regulation through activation of the Renin-Angiotensin-Aldosterone-System (RAAS), as renin is synthesized in the juxtaglomerular cells. Other endocrine functions include the synthesis of hormones such as erythropoietin, vital for hematopoiesis, as well as the hydroxylation of once-hydroxylated calcitriol to its active form as 1,25-dihydroxycholecalciferol, important for

calcium homeostasis and upholding bone structure (Gueutin et al. 2012). Thus, proper renal function provides the basis for a healthy body and emphasizes the importance of nephrological research to improve diagnostics and treatment of renal diseases.

1.2 Chronic Kidney Disease

The epidemiology of CKD shows evidence of varying etiologies causing kidney failure, which nonetheless often present a common core pathophysiology. The global prevalence of CKD is estimated to be around 10 – 13% and the prevalence increases with age (Hill et al. 2016). This fact, combined with today's demographic shift toward a continuously aging society, further emphasizes the epidemiologic significance of CKD. Lifestyle-related diseases such as diabetes mellitus and hypertension are the most frequent causes of CKD in the western world, and their increasing incidences cause a corresponding increase in the rate of CKD (Jha et al. 2013). According to the most recent Global Burden of Disease study, diabetes mellitus triggered a 31.9% increase of mortality between 2005 and 2015, which was significantly associated with the prevalence of renal failure (Wang et al. 2016; Jha et al. 2013). In contrast to these lifestyle-related ailments as the main causes of CKD in the western world, glomerulonephritis and infectious diseases due to poor hygienic conditions are the most common causes in developing countries (Jha et al. 2013). In children and infants, urinary tract obstruction, often in the upper tract causing hydronephrosis, is a predominant cause of CKD (Chevalier et al. 2009) and one of the most frequent prenatally detected abnormalities (Nguyen and Kogan 1998). Patients with CKD in all age groups requiring long-term care and treatment lead to an immense socioeconomic burden worldwide, even more so considering the high rate of comorbidities often associated with CKD (Khan and Amedia 2008).

Pathophysiological distinctions of each etiology are evident in initial stages: For instance, in patients with diabetes, chronic hyperglycemia leads to a deposit of sugars on proteins in the vascular basement membrane, forming advanced-glycation end-products (AGEs). These AGEs are only slowly metabolized and stimulate the synthesis of cytokines and the activation of the TGF-β pathway. Consequently, these inflammatory processes in the endothelium lead to basement membrane sclerosis, ultimately resulting in diffuse or nodular diabetic glomerulosclerosis (Sagoo and Gnudi 2020; Zhou et al. 2004). In patients with hypertension, the high pressure acting on the arterial walls causes damage to the endothelium which leads to arteriolosclerosis, or a hyaline thickening of the vascular endothelium (Bidani and Griffin 2004). Overall, this exemplifies sclerosis as a common pathological change in the blood vessels. Progression of the inflammation into the renal parenchyma then leads to fibrosis (Figure 2): Chronic stress,

including oxidative and hypertensive stress forms, stimulates the activation of inflammatory pathways and the synthesis of profibrogenic cytokines, ultimately kindling a process called epithelial-mesenchymal-transition (EMT) (Liu 2011). Hereby, tubular epithelial cells are transformed into contractile, alpha-smooth muscle actin (α-*SMA*)-expressing myofibroblasts which invade the interstitial space (Biernacka et al. 2011). This transformation is physiological in regular wound healing, for example in skin tissue turning keratinocytes into fibroblasts, and after fulling their task of synthesizing scar tissue, the myofibroblasts are normally eliminated through apoptosis (Meran and Steadman 2011). The pathological persistence of myofibroblasts, as it occurs in CKD, leads to an excessive production of extracellular matrix (ECM), especially collagen type I (Col1), type III and fibronectin (FN1, Zeisberg and Neilson 2010). This ECM-buildup leads to tissue fibrosis, a frequent histological and morphological end-stage manifestation of CKD as the fibrosis damages the glomerula and tubules in the kidney (Nogueira et al. 2017). In due course, the kidneys can no longer perform their essential task of hemofiltration: metabolites, toxins, and electrolytes normally excreted in the urine accumulate in the blood, disturbing metabolism, pH and electrolyte homeostasis and leading to life-threatening complications. A form of continuous RRT, such as hemodialysis, peritoneal dialysis, or a kidney transplant, becomes necessary to keep the patient alive.

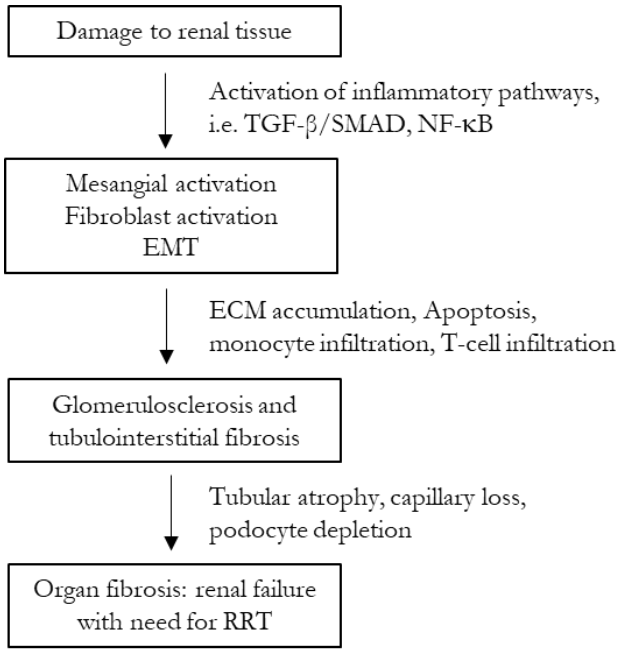

Figure 2: Overview of the pathogenesis of renal fibrosis. The terms in the boxes name the general processes occurring in the kidney, while the words to the right of the arrows further describe structural, histologic, and molecular changes that take place. Damage to renal tissue activates inflammatory pathways such as the TGF-β pathway. Subsequently, these pathways lead to mesangial and fibroblast activation and ultimately to EMT. Hereby, a buildup of ECM, leukocyte and lymphocyte infiltration, and apoptosis cause glomerulosclerosis and tubulointerstitial fibrosis. Finally, these processes lead to organ fibrosis and failure of function (based on Liu 2006, adapted with kind permission from Elsevier Publishing, RightsLink® License No. 4985970182827).

Awareness of the risk factors causing CKD allows appropriate preventive, lifestyle-based measures to be taken before RRT becomes necessary, since aside from kidney transplantation, no curative treatment for chronic kidney disease currently exists. Therefore, the treatment of CKD is primarily symptomatic, based solely on eliminating risk factors, halting disease progression, and treating the complications, such as occurs in Disease Management Programs for diabetes mellitus (Mehring et al. 2017). This includes treating renal anemia with erythropoietin and initiating hemodialysis or peritoneal dialysis to prevent complications from uremia, hypervolemia and electrolyte dysregulation (Ketteler et al. 2017). In turn, the prognosis of patients with CKD varies immensely depending on factors such as etiology, rate of albumin excretion, age, and socioeconomic status (Said et al. 2015). While RRT increases overall expected lifespan in CKD patients, the time spent on dialysis treatment is correlated with an increase in patient mortality; for example, the United States Renal Data System revealed data from the year 2012 of patients undergoing hemodialysis, showing an approx. 30% increase in mortality between two and five years after the start of dialysis (Figure 5.2.a, 2019). Concomitantly, preexisting renal dysfunction is also associated with a poorer outcome for patients with cardiovascular comorbidities, worsening the prognosis after a myocardial infarction (Moukarbel et al. 2014).

The poor prognosis of the disease and the lack of a causal treatment emphasize the importance of an early diagnosis using sensitive biomarkers as well as the development of specialized treatments to halt disease progression. Therefore, a thorough understanding of the molecular pathogenesis of renal fibrosis must be achieved to prevent or even reverse it.

1.3 Molecules, proteins, and pathways in the pathogenesis of tissue fibrosis

Despite the wide spectrum of pathologies leading to the development of kidney disease, such as hypertension, diabetes mellitus, or toxins, research has identified independent common molecular pathways that consistently play a key role in the pathogenesis of renal fibrosis. These pathways stimulate processes such as fibroblast activation, EMT, apoptosis, and macrophage and T-cell infiltration (Liu 2006).

1.3.1 TGF-β signaling and its role in tissue fibrosis

One of the most potent pathways within in the pathogenesis of tissue fibrosis is the TGF-β pathway (Liu and Desai 2015). Because of its stimulation of ECM protein synthesis, TGF-β is essential in all cases of tissue repair and tissue homeostasis; however, excessive activation leads to pathological buildup of ECM, thereby causing organ dysfunction (Branton and Kopp 1999). In the canonical TGF-β pathway, TGF-β binding to a complex of Typ I and Typ II

serine/threonine-protein receptor kinases on the cellular membrane kindles the phosphorylation of transcription factors SMADs (small mothers against decapentaplegic) 2 and 3, which, in their phosphorylated forms, build a complex with a common-mediator SMAD (co-SMAD) and can thereby translocate into the nucleus, bind their targeted DNA sequence, and regulate gene expression such as the expression of ECM proteins (Massagué 2012).

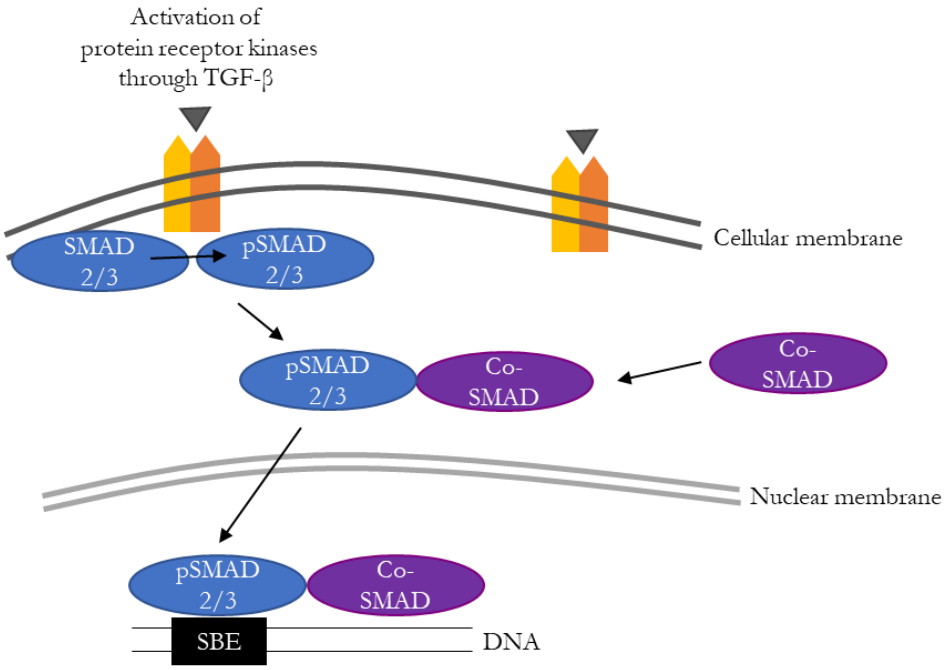

Figure 3: Canonical TGF-β signaling pathway with focus on the pro-fibrogenic players. The binding of TGF-β to a serine/threonine receptor kinase (yellow-orange structure in the cellular membrane) catalyzes the phosphorylation of SMAD to pSMAD. pSMAD passes through the cytoplasm, binds to a co-SMAD, and translocates into the nucleus. In the nucleus it binds to an SBE-sequence (SMAD-binding element) on the DNA and influences the transcription of certain genes (adapted from Massagué 2012).

TGF-β can also influence fibrosis development via various SMAD2/3-independent, non-canonical pathways. Some representatives include the p38-mitogen-activated protein kinase (MAPK) pathway (refer to Figure 4), shown to be involved in the regulation of gene expression i.e. leading to Col1 synthesis in scleroderma-related fibrosis, or leading to the phosphorylation of further transcription factors promoting kidney fibrosis development (Finnson et al. 2020).

Additionally, TGF-β and its downstream pathways lead to a dysregulation of the redox system which further promotes tissue fibrosis. The production of reactive oxygen species (ROS) in the mitochondria increases, while simultaneously the antioxidant system is suppressed by TGF-β signaling (Liu and Desai 2015). The increasing oxidative stress leads to the activation of pro-fibrotic signaling pathways and stimulates EMT (see 1.4).

Via the canonical and non-canonical signaling pathways, the cytokine TGF-β promotes tissue fibrosis through upregulation of ECM proteins and by disturbing intracellular redox balance, thus furthering inflammatory processes. While TGF-β undoubtedly plays a central role in fibrosis development, other signaling pathways are also involved, synergistically potentiating the detrimental effects.

1.3.1 NF-κB signaling and its role in tissue fibrosis

Nuclear factor-κB (NF-κB) embodies a family of proteins that act as transcription factors influencing the regulation of inflammatory responses (Liu et al. 2017). As chronic inflammation plays a fundamental role in the development of organ fibrosis, pro-inflammatory NF-κB signaling is highly relevant to understand the molecular pathogenesis of CKD. Without stimulus, NF-κB remains in the cytoplasm bound to inhibitory κBs (IκBs) (Zhang and Sun 2015). After activation, NF-κB translocates into the nucleus, binds to κB sequences in promoter or enhancer regions of the target genes and regulates gene transcription (Hayden and Ghosh 2004). Target genes regulated through NF-κB include inflammatory cytokines such as interleukins 1 and 8 (IL-1 and IL-8) and tumor necrosis factor alpha (TNF-α), and the family of superoxide dismutases (SOD) (Zhang and Sun 2015; Rojo et al. 2004).

The canonical NF-κB signaling pathway is tightly linked with the TGF-β pathway: a TGFβ-activated kinase triggers the release of NF-κB from IκB, leaving it free to enter the nucleus and leading to the mentioned transcriptional expression changes (Zhang and Sun 2015). This molecular relationship between NF-κB and TGF-β (refer to Figure 4) signaling greatly intensifies the stimulus of inflammatory processes. Furthermore, it emphasizes the complexity of cellular communication, in which a network of pathways must be considered to accurately understand pathogenetic processes.

The molecular mechanisms mentioned above underline data showing the involvement of NF-κB in fibrosis development. In the pathogenesis of tubulointerstitial fibrosis, urinary obstruction leading to tubular stretch is known to stimulate NF-κB (Zeisberg and Neilson 2010). *In-vivo* experiments support this data showing that EMT and fibrosis in a mouse UUO (unilateral ureteral obstruction) model was reduced through inhibition of NF-κB signaling (He et al. 2019). Additionally, activation of NF-κB has been linked to hydrogen peroxide (H_2O_2) -induced EMT in endothelial cells, emphasizing its part in oxidative inflammation leading to fibrosis (Montorfano et al. 2014).

Alongside TGF-β, NF-κB is a central mediator of inflammatory processes. Its connection to ROS and the TGF-β pathway make it an important player in the pathogenesis of renal fibrosis.

1.3.2 Up-regulated proteins as markers of tissue fibrosis

Several proteins are upregulated in the case of tissue fibrosis through the activation of the pathways presented (Liu 2011). α-SMA is one of the proteins that is differentially biosynthesized in the pathogenesis of CKD. In healthy kidney, strong α-*SMA* gene expression is limited to vascular smooth muscle cells (Novakovic et al. 2012). During chronic inflammation of the kidney, however, α-SMA biosynthesis occurs in activated fibroblasts and in the newly formed interstitial myofibroblasts after undergoing TGF-β induced EMT, with incorporation of α-SMA into intracellular stress fibers as well as secretion into the interstitial space (Zhou and Liu 2016; Meran and Steadman 2011). In a clinical study increasing amounts of interstitial α-SMA correlates with decreasing renal function in patients with glomerulonephritis, one of the many causes of CKD (Novakovic et al. 2012). Through this specific change in the tissue proteome, its connection to TGF-β signaling, and its correlation with renal function, the protein α-SMA is a valuable marker of pathological fibrosis in the kidney. Because of its direct involvement in renal fibrosis tissue synthesis, the fraction of α-SMA in the ECM enables the methodological quantification of fibrosis in a specific tissue (He et al. 2019).

The gene *vimentin* (*VIM*) also displays differential expression during the development of tissue fibrosis. The protein VIM is a type III intermediate filament in the cytoskeleton expressed in mesenchymal cells and has a molecular weight of approx. 54 kDa (Steinert and Roop 1988). While it is essential for cell viability and homeostasis, a pathologic accumulation is observed in tissue fibrosis, as seen in the *de novo* synthesis of VIM in kidney myofibroblasts after undergoing EMT (reviewed by Liu 2011). An upregulation of renal *VIM* expression has been shown in a model of fibrosis induction through UUO, as well the inverse reduction of Col1 deposition and fibrosis in *VIM* knockout mice (Wang et al. 2018). Furthermore, it is known that at least four different subtypes of VIM with different molecular weights and functions exist, and that changes in the expression ratio of each type were especially shown to help protect kidney fibroblasts against osmotic stress and apoptosis (Buchmaier et al. 2013). These two facets of VIM – pathologically as a fibrosis protein and beneficially as a cell defense mechanism in renal tissue – require further research to fully understand its function in the kidney.

Fibronectin (FN1) plays an important role in physiological wound healing by building scar tissue after injury. It is a glycoprotein in the extracellular matrix of tissues and is one of the largest proteins in the human body, consisting of two subunits of about 250 kDa (Potts and Campbell

1996). One of its main functions is connecting the cells via the cytoskeleton to the ECM by binding to integrin proteins (Pankov and Yamada 2002). Pathologic accumulation of FN1 within the extracellular space is also pathognomonic for tissue fibrosis in most organs, as TGF-β directly induces the transcription of *FN1* mediated by SMAD3 (reviewed by Pohlers et al. 2009; Meng et al. 2015). Furthermore, in the process of fibrogenesis, the scaffold protein FN1 plays a central role by facilitating the deposition and accumulation of other proteins, e.g. COL, thereby potentiating its pro-fibrotic effect (Genovese et al. 2014; Pankov and Yamada 2002).

α-SMA, VIM, and FN1 are all physiological proteins whose expressions are increased after fibroblast activation and whose accumulation is observed in tissue fibrosis. The quantification of these proteins therefore allows an appraisal of the degree of tissue damage under fibrotic conditions.

1.4 Oxidative stress in the pathogenesis of renal fibrosis

The relevance of oxidative stress in the pathogenesis of various chronic diseases, including tissue fibrosis such as in the kidney, has steadily gained significance (Ighodaro and Akinloye 2018).

1.4.1 Oxidants and oxidative stress in the kidney

The main group of free radicals causing oxidative stress in human tissues are oxygen-based and named thereafter. This group includes the superoxide ion (O_2^-), H_2O_2 and the peroxyl radical (HO_2), all summarized in the following as ROS. Low levels of ROS are physiological, and required for the stimulation of cellular pro-survival processes, cell proliferation and growth (Ratliff et al. 2016). Kidney tissue naturally has a high concentration of ROS, in part due to the endogenous production through stimulation of RAAS and the subsequent angiotensin II-mediated activation of nicotinamide adenine dinucleotide phosphate (NADPH) oxidases (Hitomi et al. 2007). As byproducts of metabolic processes, ROS molecules are usually inactivated by the cellular defense systems, resulting in a homeostasis between pro-oxidant and anti-oxidant systems (Ozbek 2012). Under certain conditions, this balance is disrupted, leading to the accumulation of ROS and oxidative stress with subsequent tissue damage. The accumulation of AGEs in diabetic nephropathy (described in section 1.2) is an example of such a pathological shift in the oxidant-antioxidant balance. AGEs possess oxidative potential and cause direct oxidative damage to cells and cellular macromolecules, such as vascular endothelium, DNA, lipids, and proteins, thereby impairing their structure and function (Xu et al. 2016). Furthermore, they interact with receptors and disturb metabolic and immunologic pathways, leading to the release of cytokines and increasing inflammatory processes (Okamura and Pennathur 2015). Oxidative stress has been recognized as one of the primary etiologic links between cardiovascular disease and

CKD, aside from the more traditional risk factors including hypertension and hypercholesterinemia: Through mutual pathophysiologic processes occurring systemically in the vascular endothelium and focally in the kidney, ROS cause ischemia through spasms of the vascular smooth muscle cells and impairment of vascular nitrogen monoxide (NO) synthesis (Podkowińska and Formanowicz 2020). Moreover, ROS in the kidney are known to contribute to renal injury by inducing apoptosis, for example in the podocytes, damaging the glomerular filter function, disturbing tubuloglomerular feedback mechanisms, and promoting acute and chronic inflammatory processes through increased expression of cytokine genes (Haugen and Nath 1999; Podkowińska and Formanowicz 2020).

ROS plays a central role in fibrosis development by influencing different molecular signaling pathways, leading to the processes described above (Figure 4).

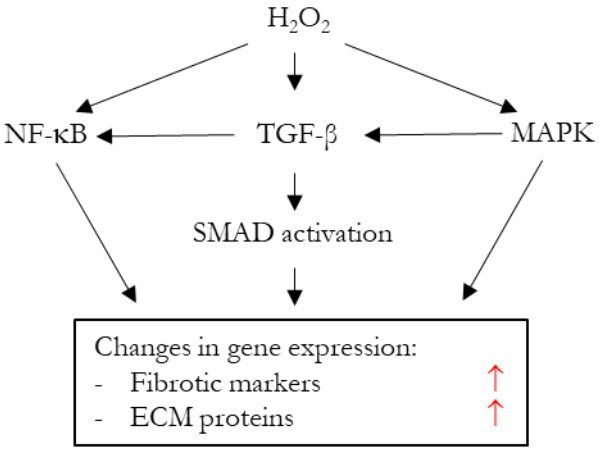

Figure 4: Oxidative stress as a stimulant for fibrosis. The figure gives an overview of the connection between H_2O_2 and the TGF-β, NF-κB, and MAPK signaling pathways, resulting in gene expression changes of endothelial markers, fibrotic markers, and ECM proteins. NF-κB acts directly as a transcription factor while TGF-β uses the SMAD protein family for differential gene expression. MAPK pathways can be activated as well, leading to non-canonical TGF-β signaling or to the stimulation of further pathways also leading to differential gene expression (Based on Montorfano et al. 2014, adapted with kind permission from Springer Nature Publishing, RightsLink® License No. 4980730583616).

ROS act as mediators of EMT by activating MAPK (Amann and Haas 2006) and thereby activating the SMAD-independent, non-canonical TGF-β signaling pathway (Liu and Desai 2015; Biernacka et al. 2011). In addition, the canonical TGF-β pathway and the NF-κB signaling pathways are also directly activated by H_2O_2, leading to the transcriptional changes described in section 1.3 (Montorfano et al. 2014). Alongside the direct stimulation of pathways, TGF-β as the central fibrosis mediator can also indirectly activate NF-κB, increasing its inflammatory potential (Montorfano et al. 2014). This illustrates how intertwined ROS and the activation of inflammatory pathways are, and how quickly this cycle can gain intensity.

1.4.2 Antioxidant mechanisms in the kidney

Various enzymatic and non-enzymatic mechanisms contribute to maintaining oxidative homeostasis in the kidney and thus play a pertinent role in preventing inflammation and fibrosis development. Non-catalytic molecules such as vitamin C, vitamin E, and uric acid act as radical scavengers and influence the balance in the redox system (Ighodaro and Akinloye 2018). When considering enzymes, the SOD family comprises the first line of defense against oxidative stress in the kidney, catalyzing the dissociation of superoxide into oxygen and H_2O_2 (Ratliff et al. 2016). Three SOD isoforms exist which are all found in renal tissue, although SOD1, a Cu/Zn-SOD, composes the majority with up to 80% of all SOD expression in the kidney (Podkowińska and Formanowicz 2020). The next reduction of ROS is performed by the thioredoxin family, catalases, and glutathione peroxidase which convert the newly formed H_2O_2 into oxygen and water (Okamura and Pennathur 2015).

Further interactions between SOD1 and H_2O_2 have been identified. For example, increased intracellular H_2O_2 levels lead to stabilization of *SOD1* mRNA and augmented *SOD1* expression (Dell'Orco et al. 2016). This has been most thoroughly researched in regard to amyotrophic lateral sclerosis (ALS), a neurodegenerative disease based on a *SOD1* mutation (Miao and St Clair 2009). Additionally, it was shown that H_2O_2 kindles the translocation of SOD1 into the nucleus where it acts as a transcription factor and induces the transcription of further genes involved in oxidant regulation and DNA repair (Tsang et al. 2014).

Clinical data has determined a correlation between *SOD1* expression and the advancement of CKD. In early stages of CKD, SOD1 has been shown to assist in maintaining NO availability by scavenging ROS and thereby attenuating CKD progression (Podkowińska and Formanowicz 2020). Concomitant with this pathophysiological relevance of SOD1, clinical research in advanced CKD stages presents data that SOD1 protein concentration is significantly decreased in patients undergoing RRT although *SOD1* gene expression is increased, thereby hinting at an augmented SOD1 protein degradation within the pathogenesis of CKD (Pawlak et al. 2007) and thus highlighting the relevance of SOD1 in renal protection from oxidative stress.

Research finds SOD1 to be a highly important enzyme in the first line of antioxidant defense, influencing inflammation and playing a role in the progression of different diseases. Further data is needed to truly understand its part in these pathogenetic processes.

1.5 Danshensu

Danshensu (3-(3,4-dihydroxyphenyl) lactic acid), also called salvianic acid A, is a phenolic acid and one of the major water-soluble pure components extracted from the plant Salvia

miltiorrhizae (Figure 5A), otherwise known as red sage or danshen (Zhao et al. 2008). Normally found in compound form as danshensu sodium salt, its molecular formula is $C_9H_9O_5$ (Figure 5B) and it has a molecular weight of 220.156 g/mol.

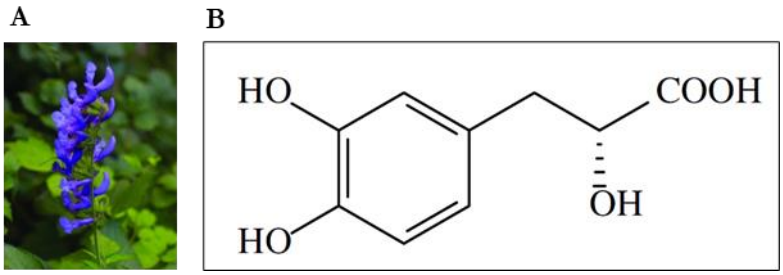

Figure 5: Illustration of Salvia miltiorrhizae and molecular structure of DSS. Image A shows a picture of Salvia miltiorrhizae, a plant found worldwide but mainly used for medicinal purposes in China (CC BY-NC-SA 3.0; Li et al. 2018). Image B shows the 2D molecular structure of DSS, one of the main active components in Salvia miltiorrhizae (Zhao et al. 2008). Reproduced with kind permission from Elsevier Publishing; RightsLink® License No. 4985970511748.

DSS, alongside salvianolic acid B, the other major compound in Salvia miltiorrhizae, have long since been used as therapeutic agents in traditional Chinese medicine especially to treat morbidities based on vascular pathologies such as cerebral ischemia, myocardial infarctions or renal sclerosis (Zhou et al. 2005). The medicinal benefits of salvianolic acid B have been more thoroughly researched, but recent studies show similar effects of DSS (Zhao et al. 2008; Zhang et al. 2019). Vasodilation is one observed effect of DSS examined in coronary and basilar arteries (Zhou et al. 2012; Zhou et al. 2005). Additionally, DSS has been shown to inhibit platelet aggregation, improve microcirculation, and protect the myocardium from reperfusion injury after an ischemic episode (Zhou et al. 2005). The antioxidant properties of DSS have also been analyzed, demonstrating a protective effect against H_2O_2-induced apoptosis and a reduction of ROS production after induced myocardial infarction in rats (Zhou et al. 2012; Li et al. 2016). Furthermore, this antioxidative effect was shown to ameliorate diabetic nephropathy and reduce the degree of tissue fibrosis (Xu et al. 2016).

To understand the underlying molecular mechanisms of DSS, fundamental research has been performed providing evidence of differential regulation of pathways involved in oxidative stress and inflammation. Firstly, it was shown that DSS decelerates the progression of cardiac fibrosis by influencing the ROS/p38 MAPK-axis (refer to Figure 4), leading to an upregulation of antioxidant proteins such as SOD1, SOD2, and NADPH-Oxidases 3 and 4 (NOX 3 and NOX4) and thus a reduction of overall ROS concentration (Lu et al. 2014). Furthermore, DSS influences the TGF-β pathway with a downregulation of TGF-β and pSMAD 2/3, as shown in a mouse model of diabetic nephropathy (Xu et al. 2016).

Its properties of vasodilation, angiogenesis and as an antioxidant make DSS a promising candidate for treatment of CKD. The TGF-β downregulation shows DSS to influence one of the central signaling pathways involved in fibrosis development, making the prevention or reversal of renal fibrosis an intriguing prospect. Further research is required to understand the effect of DSS on different etiological entities of CKD and to uncover the primary underlying mechanisms as basis for the observed molecular and clinical outcomes.

1.6 Research Purpose

To enhance treatment opportunities and improve the prognosis for an increasing number of patients with CKD, advancement of nephrological research is necessary to more thoroughly understand the pathogenetic processes involved in fibrosis development and to examine new therapeutic candidates. Based on research showing positive effects of Salvia miltiorrhizae plant extracts on fibrosis in other organ tissues, DSS, as one of the primary extracts, may pose such a therapeutic option. This study aims to investigate the influence of DSS on the pathogenesis of renal fibrosis with focus on oxidative stress and fibrotic pathways such as the TGF-β signaling pathway. Initially, an *in-vitro* model using the TK173 renal cell line is applied firstly to assess the impact of DSS on cells affected by oxidative stress using a cell viability assay and FACS quantification of ROS, and secondly on the synthesis of pertinent fibrosis and antioxidant proteins as determined in Western blot. Furthermore, the influence of DSS on the morphology of renal tissue using periodic acid Schiff (PAS) stains and on fibrosis-related protein synthesis in immunohistochemical stains in the *in-vivo* mouse model of unilateral ureteral obstruction, leading to characteristics of interstitial fibrosis as is common in final stages of CKD, is analyzed. This allows the translation of possible effects of DSS in the genetically modified cell line onto a mammalian model organism and reflects urinary obstruction as one of the main pediatric causes of CKD.

2 Material and Methods

2.1 Material

2.1.1 Chemicals and Enzymes

Table 1: List of chemical reagents

Chemical	Manufacturer
Acrylamide 30%	PanReac AppliChem ITW Reagents, Darmstadt/Germany
Bromphenolblue	Sigma-Aldrich Corporation, St. Louis/USA
Bovine serum albumin (BSA)	Sigma-Aldrich Corporation, St. Louis/USA
3-((3-cholamidopropyl) dimethylammonio)-1-propanesulfonate (CHAPS)	Carl Roth GmbH + Co. KG, Karlsruhe/Germany
Citric Acid Trisodium Salt, dihydrate	Sigma-Aldrich Corporation, St. Louis/USA
Citric Acid, monohydrate	Merck KGaA, Darmstadt/Germany
CM-H_2DCFDA	Thermo Fischer Scientific, Waltham/USA
DMEM	gibco® by life technologies™, Carlsbad/USA
DPBS	gibco® by life technologies™, Carlsbad/USA
DSS	Sigma-Aldrich Corporation, St. Louis/USA
Dithiothreitol (DTT)	Sigma-Aldrich Corporation, St. Louis/USA
EDTA	Merck KGaA, Darmstadt/Germany
Ethanol	Chemsolute® by Th. Geyer GmbH & Co. KG, Renningen/Germany
FCS	gibco® by life technologies™, Carlsbad/USA
Gentamicin	gibco® by life technologies™, Carlsbad/USA
Glycerine	Merck KGaA, Darmstadt/Germany
Glycine	Carl Roth GmbH + Co. KG, Karlsruhe/Germany
Goat serum	Sigma-Aldrich Corporation, St. Louis/USA
Isopropanol	Merck KGaA, Darmstadt/Germany
Hydrogen Chloride	Merck KGaA, Darmstadt/Germany
Hydrogen peroxide 30%	Merck KGaA, Darmstadt/Germany
L-glutamine	Sigma-Aldrich Corporation, St. Louis/USA
Mayer's hematoxylin solution	Carl Roth GmbH + Co. KG, Karlsruhe/Germany
Mercaptoethanol	FLUKA, Sigma-Aldrich Corporation, St. Louis/USA
Methanol	Carl Roth GmbH + Co. KG, Karlsruhe/Germany
Natriumdodecylsulfate (SDS)	FLUKA, Sigma-Aldrich Corporation, St. Louis/USA
N,N,N',N'-Tetramethylethylenediamin (TEMED)	Sigma-Aldrich Coporation, St. Louis/Missouri
Penicillin/Streptomycin	gibco® by life technologies™, Carlsbad/USA

Chemical	Manufacturer
Periodic Acid Solution 1%	Carl Roth GmbH + Co. KG, Karlsruhe/Germany
Ponceau S solution	SERVA Electrophoresis GmbH, Heidelberg/Germany
Powdered milk	Carl Roth GmbH + Co. KG, Karlsruhe/Germany
Precision Plus Protein All Blue Standards	Bio-Rad Laboratories, Hercules/USA
Protein Assay Dye Reagent Concentrate	Bio-Rad Laboratories GmbH, Munich/Germany
Schiff's Reagent	Carl Roth GmbH + Co. KG, Karlsruhe/Germany
Sodium chloride (NaCl)	Merck KGaA, Darmstadt/Germany
Sodium hydroxide (NaOH)	Merck KGaA, Darmstadt/Germany
Tris(hydroxymethyl)-aminomethan (Tris)	Carl Roth GmbH + Co. KG, Karlsruhe/Germany
Trypsin	gibco® by life technologies™, Carlsbad/USA
Tris(hydroxymethyl)-aminomethan (Tween® 20) 0,1%	Carl Roth GmbH + Co. KG, Karlsruhe/Germany
Urea	Sigma-Aldrich Coporation, St. Louis/USA
Xylene	Chemsolute® by Th. Geyer GmbH & Co. KG, Renningen/Germany

2.1.2 Antibodies

Table 2: List of primary antibodies with target antigen, host species, and applied dilution

Antigen	Host	Experiment	Dilution	Manufacturer
VIM	Mouse	Western blot	1:5000	Dako Denmark A/S, Glostrup, Denmark
SOD1	Rabbit	Western blot	1:1000	Abnova, Thermo Fischer Scientific, Waltham/USA
FN1	Rabbit	Western blot	1:10,000	Abcam, Cambridge/ United Kingdom
β-actin	Mouse	Western blot	1:5000	Sigma-Aldrich, Steinheim/Germany
GAPDH	Rabbit	Western blot	1:5000	Sigma-Aldrich, Steinheim/Germany
α-SMA	Mouse	Immunohistochemistry	1:200	Sigma-Aldrich Corporation, St. Louis/USA
pSMAD2	Rabbit	Immunohistochemistry	1:100	Cell Signaling Technology, Cambridge/United Kingdom
Col1	Mouse	Immunohistochemistry	1:150	Abcam, Cambridge/ United Kingdom

Table 3: List of secondary antibodies with target antigen, host species, and applied dilution

Antibody	Host	Experiment	Dilution	Manufacturer
Alexa Fluor anti-mouse, 555 nm	goat	Immunohistochemistry	1:500	Thermo Fischer Scientific™, Waltham/USA
Alexa Fluor anti-rabbit, 488 nm	goat	Immunohistochemistry	1:500	Thermo Fischer Scientific™, Waltham/USA
Alexa Fluor anti-mouse, 647 nm	goat	Western blot	1:2000	Thermo Fischer Scientific™, Waltham/USA
Alexa Fluor anti-rabbit, 647 nm	goat	Western blot	1:2000	Thermo Fischer Scientific™, Waltham/USA

2.1.3 Used kits and composition of buffers and solutions

Table 4: List of used kits

Method	Kit	Manufacturer
MTT	Cell Proliferation Kit I (MTT)	Roche Applied Sciences, Mannheim/Germany

Table 5: List of solutions and buffers.

Solution or buffer	Components
Bromophenol blue solution	Tris-HCl pH 8.8 (1.5 M), 0.25% (w/v) bromophenol blue
Cell culture DMEM	DMEM, 10% FCS, 1% L-glutamine, 1% penicillin/streptomycin and 1% gentamicin
Electrophoresis buffer (5x)	30 g Tris, 144 g glycine, 10 g SDS in 2 l ddH_2O
Lysis buffer	9.5 M Urea, 2% (w/v) CHAPS, 1% (w/v) DTT, 2% (v/v) Bio-Ampholyte
Medium for TK173 cells	DMEM-Medium, 10% (v/v) FCS, 1% (v/v) L-glutamine, 1% (v/v) penicillin/ streptomycin, 1% (v/v) gentamicin
Milk blocking buffer	Washing buffer (1x), 5% (w/v) powdered milk
Sample buffer (4x)	4.3 ml ddH_20, 2.5 ml 0.5 M Tris/HCl pH 6.8, 5 ml glycerine, 8 ml 10% SDS, 200 µl 1% (v/v) bromophenol blue solution, 2% (v/v) 2-mercaptoethanol added directly before use
Separation gels (12%)	14 ml ddH_2O, 10 ml 1.5 M Tris/HCl pH 8.8, 16 ml acrylamide, 200 µl 10% (w/v) APS, 400 µl 10% (w/v) SDS, 30 µl TEMED
Stacking gels (4%)	15 ml ddH_20, 6.3 ml 0.5 M Tris/HCl pH 6.8, 3.9 ml acrylamide, 125 µl 10% (w/v) APS, 250 µl 10% (w/v) SDS, 25 µl TEMED

Solution or buffer	Components
Transfer buffer (1x)	20% (v/v) transfer buffer (5x), 20% (v/v) methanol, ddH_2O
Transfer buffer (5x)	30.3 g Tris, 144 g glycine, 5 g SDS, filled with ddH_2O to reach 2 l
Trypsin/EDTA	0.825 g EDTA, 10% (v/v) Trypsin (2.5%), filled with DPBS to reach 500 ml
Washing buffer (5x)	12.11 g Tris, 58.16 g NaCl, 2 l ddH20, pH 7.4, 10 ml Tween® 20

2.1.4 Disposable Material and Laboratory Equipment

Table 6: List of disposable material used

Material	Type or Model	Manufacturer
Cell culture flasks	150 ml T75	Sarstedt, Nümbrecht/Germany
Cell culture plates	6-well plates 96-well plates	BD Falcon™, Durham/USA Zell Kontakt GmbH, Nörten-Hardenberg/Germany
Cover slips	24x60 mm #1	Menzel, Braunschweig/Germany
Cuvette	10x4x45 mm	Sarstedt, Nümbrecht/Germany
Delicate Task Wipers, 1-Ply	Kimtech Science™ Kimwipes™	Kimberly-Clark Professional, Reigate/United Kingdom
Filter paper		Bio-Rad Laboratories GmbH, Munich/Germany
Gloves	Sizes S, M, L	Rösner-Mautby Meditrade GmbH, Kiefersfelden
Nitrocellulose membrane	0,45µm Amersham Protran Premium	GE Healthcare Europe GmbH, Munich/Germany
Object plate	Menzel-Gläser Super-frost Plus 25x75x1mm	Thermo Fischer Scientific, Waltham/USA
Pasteur Pipettes, glass		Brand, Wertheim/Germany
Pipettes	5 ml 10 ml 25 ml	Sarstedt, Nümbrecht/Germany
Pipette tips	10 µl 200 µl 1000 µl	Sarstedt, Nümbrecht/Germany
Pipetus® - PIPETBOY		Hirschmann Laborgeräte GmbH & Co. KG, Eberstadt/Germany
Reference Pipettes	10 µl 100 µl 200 µl 1000 µl	Eppendorf AG, Hamburg/Germany
Roundbottom tubes	10 ml 50 ml	BD Falcon™, Durham/USA
Scalpel	Disposable Scalpel No.21 pfm (sterile)	Feather Safety Razor Co. Ltd, Osaka/Japan

Table 7: List of technical equipment und reusable material

Equipment	Model	Manufacturer
Autoclave	Type 83 714 A	Integra Biosciences, Tecnomara Deutschland GmbH, Fernwald/Germany
Biomedical Freezer	MDF-U5312	Panasonic Healthcare, Tokyo/Japan
Biomedical Freezer	Ultra-low Temperature Freezer, MDF-U76V	Panasonic Corporation, Tokyo/Japan
Cell Culture Hood	BSB4A	GELAIRE® Flow Laboratories, Sydney/Australia
Cell Culture Hood	Class II	NUAIRE, Plymoth/USA
Centrifuges	1-15PK 3-18K	Sigma Laborzentrifugen GmbH, Osterode am Harz/Germany
Cooling unit	4°C, K 3710 Index 20B/001	Liebherr, Kirchdorf/Germany
Electrophoresis Set	Mini-PROTEAN® 3 Cell	Bio-Rad Laboratories GmbH, Munich/Germany
Electrophoresis Power Supply	E815	Consort bvba, Turnhout/Belgium
Electrophoresis Power Supply	PS3002	Life Technologies, Carlsbad/USA
Elisa Reader	PHOmo	autobio, Zhengzhou/China
Fleece sponge		Bio-Rad Laboratories GmbH, Munich/Germany
Flow cytometry	FACS Canto™ II	BD Biosciences, Franklin Lakes/USA
Fluorescence Laser scanner	FLA-5100	Fujifilm life science, Stamford/USA
Heated magnetic stirrer	IKAMAG RCT	IKA®-Werke GmbH & CO. KG, Staufen/Germany
Incubator	NAPCO Series 5400 CO_2	Thermo Fischer Scientific™, Waltham/USA
Incubator	Heraeus	Thermo Fischer Scientific™, Waltham/USA
Incubator	Model 400	Robbins Scientific Corp, San Diego/USA
Microscope	IX71	Olympus, Tokyo/Japan
Microscope	Axiovert 25 inverted	Carl Zeiss Microscopy, Jena/Germany
Microtome	Reichert-Jung 2040 AutoCut Microtome	Leica Microsystems GmbH, Wetzlar/Germany
Multipipette	M4	Eppendorf AG, Hamburg/Germany
pH-meter	Basic Meter PB-11	Sartorius, Göttingen/Germany
pH Electrode	InLab Routine	Mettler Toledo, Columbus/USA
Power supply	U-RFL-T Fluorescence	Olympus, Tokyo/Japan
Scale	Universal	Sartorius, Göttingen/Germany

Equipment	Model	Manufacturer
Shaker	Model 3014	GFL (Gesellschaft für Labortechnik), Burgwedel/Germany
Shaker and water bath	Model 1083	GFL, Burgwedel/Germany
Spectrophotometer	Lambda 25 UV/VIS	Perkin Elmer, Waltham/USA
Thermal Cycler	Mastercycler Personal	Eppendorf, Hamburg/Germany
Thermo Shaker	Modell Kühner	B. Braun, Melsungen/Germany
Vortex Mixer	REAX 2000	Heidolph Instruments GmbH & Co.KG, Schwabach/Germany
Water-repellent pen		Dako Denmark A/S, Glostrup/Denmark

2.1.5 Software

Table 8: List of digital software used

Program	Manufacturer
AUTOsoft Control and Evaluation Software	Autobio, Zhengzhou/China
Cell D 3.4	Olympus, Hamburg/Germany
iCys® 3.4.12.	CompuCyte Corporation, Westwood/USA
FACSDiva™ Version 6.1.3	BD Biosciences, Franklin Lakes/USA
GraphPad PRISM 9	Graphpad Prism Software, Inc., San Diego/USA
Image J	National Institute of Health LOCI, University of Wisconsin
Microsoft Word 2010	Microsoft Corporation, Redmond/USA
Microsoft Excel 2010	Microsoft Corporation, Redmond/USA
Microsoft PowerPoint 2010	Microsoft Corporation, Redmond/USA
Image Reader FLA-5000 Version 3.0	Fujifilm life science, Stamford/USA

2.2 Methods

2.2.1 Cell line and culture procedure

In-vitro experiments were performed using TK173 cells. TK173 is a renal fibroblast cell line developed in the University Medical Center in Göttingen, Germany by transfection-induced immortalization with the plasmid pSV3gpt from Simian virus 40. The cells originally derive from human renal tissue and maintain typical morphological and biochemical properties of renal interstitial fibroblasts (Müller et al. 1995).

Morphologically, the fibroblasts display their pathognomonic structure with a spindle, triangle, or rhomboid-shaped form and narrow tails extending to the sides (Figure 6). In this way, the fibroblasts gain contact to neighboring cells and form stable clusters.

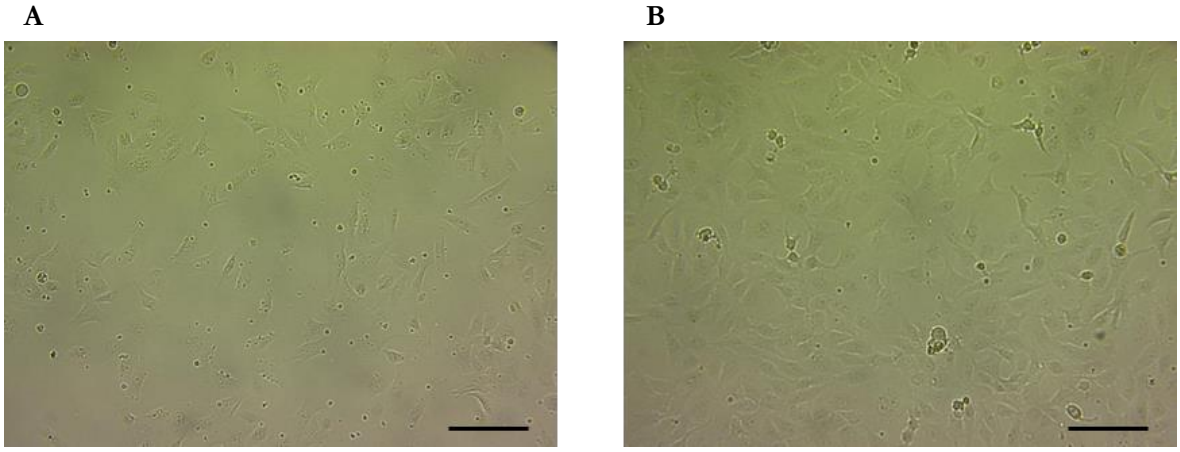

Figure 6: TK173 cells under standard conditions. The light microscopical image show TK173 cells one day after seeding in a well of a 6-well plate at 100x magnification (A). Individual cells can be identified and, as expected directly after seeding, there is little to no contact between the fibroblasts. The kidney fibroblasts are recognizable by their spindle, triangle or rhomboid-shaped form with narrow tails extending to different sides. Two days after seeding, the fibroblasts have begun to form clusters, organizing themselves into a stable complex of cells (B). Scale bar: 150 μm.

The cells were routinely kept in T75 cell culture flasks and cultured in a humidified incubator with a 95% air/5% CO_2 atmosphere at 37°C. They were grown in Dulbecco's Modified Eagle Medium (DMEM) supplemented with 10% fetal calf serum (FCS), 1% L-glutamine, 1% penicillin/streptomycin and 1% gentamicin, in the following described as "cell culture DMEM". All work with cell cultures was performed under sterile conditions.

When a confluence of approx. 80 – 90% was reached, the cell culture was split to avoid cell stress and apoptosis due to overpopulation. The medium was withdrawn under suction and the cell layer then rinsed with warmed Dulbecco's Phosphate Buffered Saline (DPBS), removing excess medium and dead cells. Subsequently, the cells were dissociated from the floor of the flasks using 2 ml of the trypsin/EDTA stock solution. Inspection under a microscope confirmed dissociation of the cells from the flask under trypsin influence. The cells were then resuspended in cell culture DMEM and divided into the required number of new flasks.

2.2.2 MTT cell proliferation assay

The 3-(4,5-Dimethylthiazol-2-yl)-2,5-diphenyltetrazoliumbromid (MTT) cell proliferation assay is a colorimetric assay to assess cell metabolism and viability based on the presence of NADH or NAPDH-dependent enzymes. Developed in its original form in 1983, the colorimetric MTT assay continues to be the gold standard for assessing cytotoxicity and is most commonly used to assess the cytotoxicity of drugs in varying concentrations (Mosmann 1983). MTT has a lipophilic side and is therefore able to pass the cell membrane and be metabolized intracellularly

(Präbst et al. 2017). This quality allowed a linear correlation between the photometric extinction and the relation to NADPH-dependent metabolism to be drawn: MTT entered all cells independent of active transport and thus indicated the number of living cells. Water-soluble MTT was yellow in its oxidized form whereas reduction through mitochondrial and endoplasmic enzymes yielded the chemical compound formazan, initially found as an intracellular blue-violet crystal. In the final step, the cells were lysed thereby releasing the formazan crystals, and the crystals ultimately dissolved allowing a photometric measurement of the blue-violet color (Präbst et al. 2017). In this way, the quantification of metabolic activity and cell viability could be assessed.

The assay was performed to evaluate the effects of different DSS and H_2O_2 concentrations on the metabolism and viability of TK173 kidney fibroblasts. For the MTT cell proliferation assay, Cell Proliferation Kit I from Roche was used according to the manufacturer's instructions. In 96-well plates, approximately 5000 cells per well were seeded, determined using a Neubauer counting chamber, and the cells then treated directly in the wells.

Each test group was seeded with three technical replicates per 96-well plate, and the test was repeated three times (n = 3). For each test concentration, one negative control well and one well containing no cells and solely the treatment medium was prepared. This "blank control" was necessary to determine the natural extinction caused by the medium. The first treatment approach added DSS diluted in cell culture DMEM in concentrations from 10 – 250 µM in increments of 50 µM. A second approach added H_2O_2 diluted in cell culture DMEM, again in concentrations ranging from 10 – 250 µM in 50 µM increments. To investigate whether the DSS would rescue the cells from the oxidative stress induced by the H_2O_2, a third approach was prepared, allowing the cells to incubate in a 200 µM DSS solution for 24 h before inducing oxidative stress with H_2O_2 in the same concentrations from 10 – 250 µM in 50 µM increments. Measurements were taken after 24 h and 48 h (Table 9). At the given time, 10 µl of MTT labeling reagent was added to each well and incubated for an additional 4 h. The extinction was measured with a PHOmo Elisa Reader at 595 nm.

Table 9: Treatment protocol for MTT cell proliferation assay

Treatment	Treatment concentrations [µM]	Measurement time period
DSS	10, 50, 100, 150, 200, 250	after 24 h and 48 h
H_2O_2	10, 50, 100, 150, 200, 250	after 24 h and 48 h
Combined treatment: DSS for 24h followed by H_2O_2	DSS: 200 H_2O_2: 10, 50, 100, 150, 200, 250	after 24 h and 48 h

2.2.3 Quantification of intracellular ROS using CM-H_2DCFDA and FACS

Fluorescence-activated cell sorting (FACS) allows the quantitative analysis of cell fluorescence of a desired cellular molecule. In this case, chloromethyl dichlorodihydrofluorescein diacetate acetyl ester (CM-H_2DCFDA) was used to indicate intracellular ROS accumulation in TK173 cells after subjecting the cells to oxidative stress using H_2O_2. The probe is non-fluorescent in its reduced form and is able to cross the cell membrane passively (Kristiansen et al. 2009). Upon contact with ROS, it is converted to its highly fluorescent oxidized form, 2',7'-dichlorofluorescein (DCF) and the fluorescence can be measured via flow cytometry (Ameziane-El-Hassani and Dupuy 2013). Only propidium iodide (PI)-negative cells with positive DCF fluorescence were analyzed thereby focusing on ROS in living cells.

TK173 cells were prepared in three treatment groups: "background control" with cell culture DMEM supplemented with 0.9% NaCl in ddH_2O, "untreated" with cell culture DMEM, and "treated" with 200 µM DSS-supplemented cell culture DMEM. Background control was tested to eliminate the possible influence of the 0.9% NaCl in ddH_2O in ROS production, as this was the solvent used to dilute the DSS.

Each group was incubated in its corresponding treatment medium, i.e. cell culture DMEM, cell culture DMEM with NaCl, and cell culture DMEM with DSS, in T-75 cell culture flasks for 24 h at 37°C prior to FACS analysis. Then, the cells were trypsinized, centrifuged in DMEM for 5 min at 1200 rpm, washed with PBS and centrifuged again for 5 min at 1200 rpm. The remaining cell pellet was then resuspended in Hank's balanced salt solution (HBSS) medium supplemented with CM-H_2DCFDA diluted in dimethyl sulfoxide, ultimately attaining a 50 µM concentration of the staining probe. Each treatment group was then divided again into a stressed and unstressed group, each containing two technical replicates. The cells subjected to oxidative stress were treated with 100 µM H_2O_2 and incubated for 40 min (Table 10). Finally, 5 µl PI was added to the tubes.

Table 10: Treatment protocol for FACS quantification of DCF fluorescence

	Treatment Medium Incubation over 24 h	**Unstressed**	**Stressed with 100 µM H_2O_2 Incubation for 40 min**
Background control	Cell culture DMEM + NaCl	x	x
Untreated	Cell culture DMEM	x	x
Treated	Cell culture DMEM + DSS	x	x

FACS was preformed using a FACS Canto™ II cytometer. Unstressed, untreated samples supplied the adjusting values of cell fluorescence through treatment solely with PI or CM-H_2DCFDA. 10,000 events were recorded in each sample. Finally, the mean fluorescence intensity of the events was compared between the unstressed and stressed, and the DSS-treated and untreated samples.

2.2.4 Cell treatment and culture experiments

Applying the results of the MTT assay, TK173 cells were treated directly in culture flasks once reaching a cell confluency of about 75%. Four groups were established that were incubated as follows over a period of 48 h: "control" in cell culture DMEM, "treatment" in cell culture DMEM supplemented with 200 µM DSS, "stressed" in cell culture DMEM supplemented with 100 µM H_2O_2, and a "treated stressed" group undergoing a 6 h pre-incubation in cell culture DMEM supplemented with 200 µM DSS followed by 48 h in cell culture DMEM supplemented with 100 µM H_2O_2.

For protein expression analysis, TK173 cells were harvested via trypsinization (see 2.2.1) after the 48 h treatment incubation period. Next, the cells were twice resuspended in 5 ml of DPBS and centrifuged at 1200 rpm for 5 min in a 3-18K centrifuge. A lysis buffer solution of 9.5 M urea, 2% CHAPS, and 1% DL-Dithiothreitol was added to the pellet and incubated on ice for 30 min. To increase the purity of the cell extract and remove cellular debris, the suspension was centrifuged twice for 30 min at 14000 rpm in a 1-15PK centrifuge, and the supernatant was then harvested and stored at -20°C until use (see 2.2.5).

2.2.5 Western Blot

Western blot, also called immunoblot, is one of the most frequently performed methods in scientific research and allows protein identification as well as the semi-quantitative analysis of protein expression (Mishra et al. 2017).

2.2.5.1 Preparation of protein samples and SDS-PAGE

To quantify the protein concentration after cell lysis, the Bradford method was applied (Bradford 1976). The Protein Assay Dye Reagent Concentrate was diluted to a fraction of 1:5 using ddH_20. BSA dilutions for the calibration curve of extinction were established according to the manufacturer's instructions (Table 11) and the extinction measured at 595 nm using a Lambda 25 UV/VIS spectrophotometer.

Table 11: Protocol for establishing a calibration curve using the Bradford method of protein quantification

BSA solution (1mg/ml) [µl]	Diluted Bradford Protein Assay Dye Reagent [µl]
0	1000
2	998
4	996
6	994
8	992
10	990

BSA, in 2 µl increments, and 1:5 diluted Bradford Protein Assay Dye Reagent were combined to obtain a 1 ml solution. The extinction of the different solutions allowed a calibration curve for the diluted Assay Dye Reagent to be established.

To determine the protein content in our cell extract, 2 µl of the diluted cell lysate (1:10 in ddH_2O) were transferred in 998 µl of protein assay dye and incubated for 10 min on ice. After measuring the extinction, the protein concentration was calculated in accordance with the calibration curve.

The polyacrylamide gels for sodium dodecyl sulfate (SDS)-polyacrylamide gel electrophoresis (PAGE) consist of a separation gel and a stacking gel. By migrating through the separation gel along an electric field, the negatively charged proteins in the sample are divided according to size, i.e. smaller proteins pass through the gel faster and are seen farther down, towards the positively charged anode (Brunelle and Green 2014). 12% separation gels were prepared with a mixture of ddH_2O, 1.5 M Tris/HCl solution (pH 8.8), and acrylamide combined in a glass flask and then exposed to vacuum pressure for 10 min to eliminate air bubbles and lower the risk of ROS production. For polymerization, 800 µl of 10% SDS, 60 µl of tetramethylethylendiamine (TEMED) and 400 µl of 10% ammonium persulfate (APS) were added and mixed gently. Thereafter, the gel was poured into the rack and covered with isopropanol to ensure an even surface. The isopropanol was removed prior to the addition of the stacking gel solution.

The 4% stacking gels were prepared initially with 15 ml of ddH_2O, 6.3 ml of 1.5 M Tris/HCl at a pH of 6.8 and 3.9 ml of acrylamide, and exposed to vacuum pressure for 10 min. For polymerization, 250 µl of 10% SDS, 300 µl of TEMED, and 125 µl of 10% APS were added. This solution was poured on the polymerized separation gel, a comb was inserted to form the pouches, and left to polymerize. The finalized gels were ready to use or stored in a humid environment at 4°C and used within 3 – 4 days.

After determination of the protein concentration using Bradford Protein Assay, 70 µg of protein were diluted in ddH_20 und sample buffer, yielding a final volume of 20 µl. Prepared samples were denaturated at 96°C for 10 min and afterwards placed on ice. Heat and the SDS in the sample buffer denature the proteins, thereby destroying their secondary and tertiary structures, and obtaining a homogenous negative charge on the proteins so that they can pass through the electric field from the cathode towards the anode while migrating through the gels (Brunelle and Green 2014).

Standard BioRad chambers were used to perform SDS-PAGE. The chamber was filled with 1x electrophoresis buffer, covering the gel. The comb was removed, and the samples were applied into the corresponding pouches. Precision Plus Protein All Blue Standards was used as a reference marker in the first lane. The electrophoresis ran at 160 V for 10 min, at 180 V for further 10 min, and finally at 200 V until the marker had reached the bottom of the gel.

2.2.5.2 Performance of Western Blotting

Western blotting was performed according to Towbin et al. (1979) using a 0.45 µm nitrocellulose membrane.

After electrophoresis, the gels were removed from between the glass plates and organized in a Western blot sandwich (Figure 7). Hereby, the nitrocellulose membrane was placed on the gel, and these layers were then surrounded by filter paper and white sponges as protection and to protect the sandwich from drying.

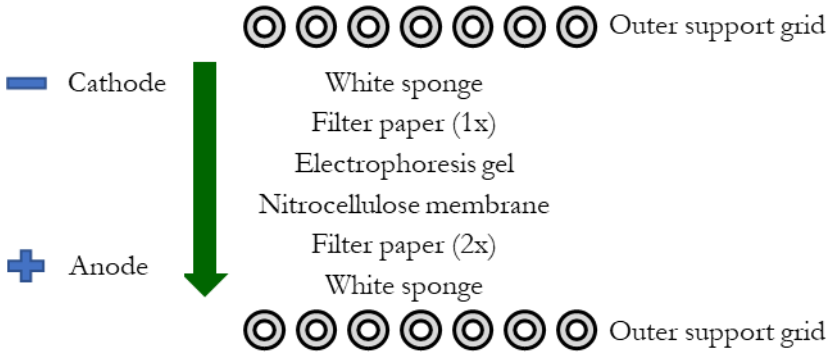

Figure 7: Setup of the Western blot sandwich. As the electricity moves from the cathode towards the anode, it first passes through the upper white sponge and an initial layer of filter paper. When it reaches the electrophoresis gel, the proteins are removed from their binding in the gel and transferred onto the nitrocellulose membrane placed underneath it. The bottom layers consist of another layer of filter paper and the lower white sponge as protection. Outer support grids compress the sandwich and guarantee stability during the blotting process.

A roller compressed the sandwich to eliminate the risk of air bubbles caught between the gel and the membrane, thereby maximizing the contact area. The sandwich was then placed in a standard BioRad chamber for protein transfer and covered with transfer buffer. The protein transfer occurred at 35 V at 4°C overnight. To confirm successful blotting, the nitrocellulose membrane was placed in 0.2% Ponceau S solution for one minute to attain a reversible staining of the transferred protein bands. The Ponceau S solution was removed by washing in 5% acetic acid and then in washing buffer. Finally, the membrane was left to air dry at room temperature.

Excess binding sites on the membrane were blocked to avoid unspecific binding of the antibodies to the membrane. To block the free protein binding sites, the membrane was incubated in blocking buffer (5% skim milk in washing buffer) and placed on a shaker for 2 h at 37°C.

Protein specific antibodies were used for detection of the proteins of interest on the nitrocellulose membrane. β-actin (42 kDa) and glyceraldehyde 3-phosphate dehydrogenase (GAPDH, 35 kDa) were used as housekeeping proteins, depending on the molecular weight of the protein of interest. The primary antibodies were diluted in blocking buffer as recommended by the manufacturer (Table 2) and then poured over the membrane. Incubation with the primary antibodies occurred for 1 h at 37°C and then overnight at 4°C, under continuous shaking. To remove excess, unbound antibodies, the membrane was washed in washing buffer three times for 10 min at 37°C. The secondary antibody was diluted in blocking buffer as recommended by the manufacturer (Table 3), applied to the membrane, and incubated on a shaker at 37°C for 2 h. After incubation of the secondary antibodies, three wash cycles in washing buffer were performed, for 10 min at 37°C each. Finally, the membrane was left to air dry in a darkened space and scanned with a FLA-5100 gel reader at 647 nm.

2.2.5.3 Quantification of protein expression

Protein expression was quantified using the image processing software ImageJ (Figure 8). The band of interest was selected and quantified in accordance with the manufacturer's analysis guidelines. Each band was normalized in respect to the control, and then adjusted for intensity deviations of the housekeeping gene. Thereby, discrepancies in the protein loading were equalized and changes in protein expression because of the treatment could be compared to the untreated control sample.

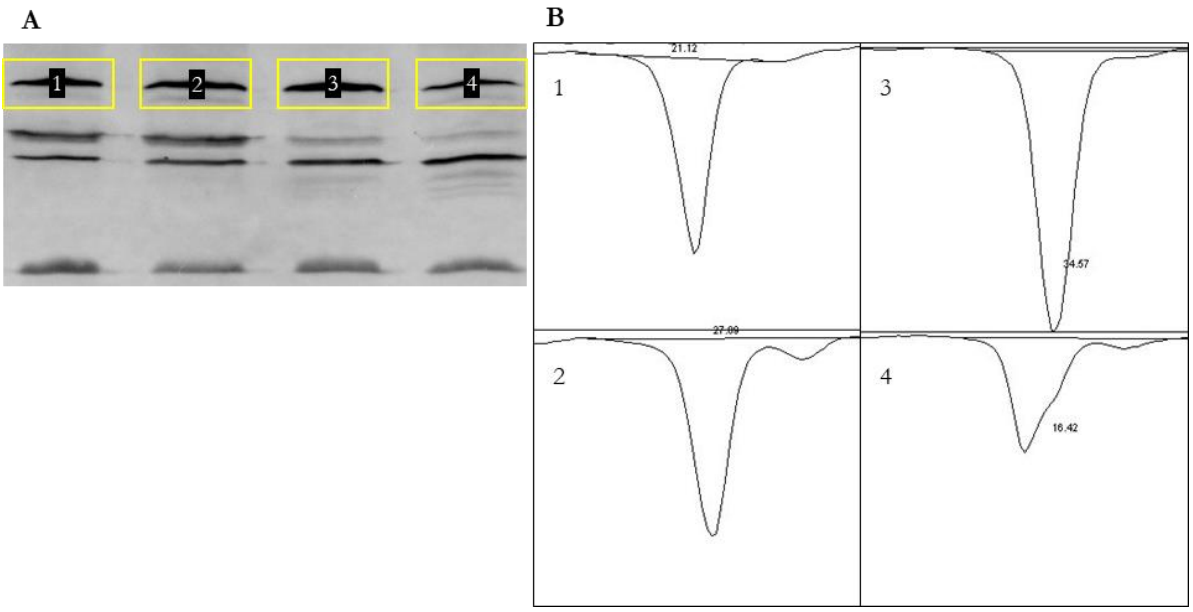

Figure 8: ImageJ analysis of Western blot. The figure illustrates the analysis of an exemplary Western blot as it was applied for all Western blots in this study. The desired lanes are enclosed and thereby defined (A). Next, the software program calculates the change in color intensity compared to a baseline, which correlates with the background color (B). The data is presented as a percentage, with the total intensity of all lanes equal to 100%. This method was applied individually to each protein of interest and the housekeeping gene on the same blot.

2.2.6 *In-vivo* mouse model for renal fibrosis

UUO, an established *in-vivo* model for renal fibrosis, can be performed in different species and the observed histologic interstitial fibrosis as a consequence of the obstruction is a common characteristic of most forms of progressive renal disease (Chevalier et al. 2009). In the surgery, the ureter of the UUO kidney was ligated, causing urinary retention and hydronephrosis, while the other kidney underwent solely a "sham" or placebo surgery without ureter ligation (Figure 9). In this study, the mouse as model organism was chosen to perform UUO and subsequently to investigate possible effects of DSS treatment on the development of the UUO-induced interstitial fibrosis.

2.2.6.1 UUO surgery

Healthy, WT C57B/6 mice were bred in and acquired from the animal facilities of the University Medical Center Göttingen (UMCG). All animal interventions were executed by trained and qualified personnel. UUO and sham surgeries on the mice were performed in the European Neuroscience Institute (ENI), UMCG in cooperation with Dr. Björn Tampe, Department of Nephrology and Rheumatology, UMCG. All experimental procedures were performed according to the German Animal Care and Ethics Legislation (33.14-42502-04-11/0598) (NIH standards) and were approved by the local Ethics Committee of the UMCG, Germany. The mice were anesthetized with 1 – 3% inhalant isoflurane prior to surgery and with 5% isoflurane induction with a precision vaporizer during surgery. The analgesic medication included 0.1 ml subcutaneous buprenorphine shortly before surgery and oral administration of 3 ml/l metamizole in tap water changed every 48 h until 48 h before death.

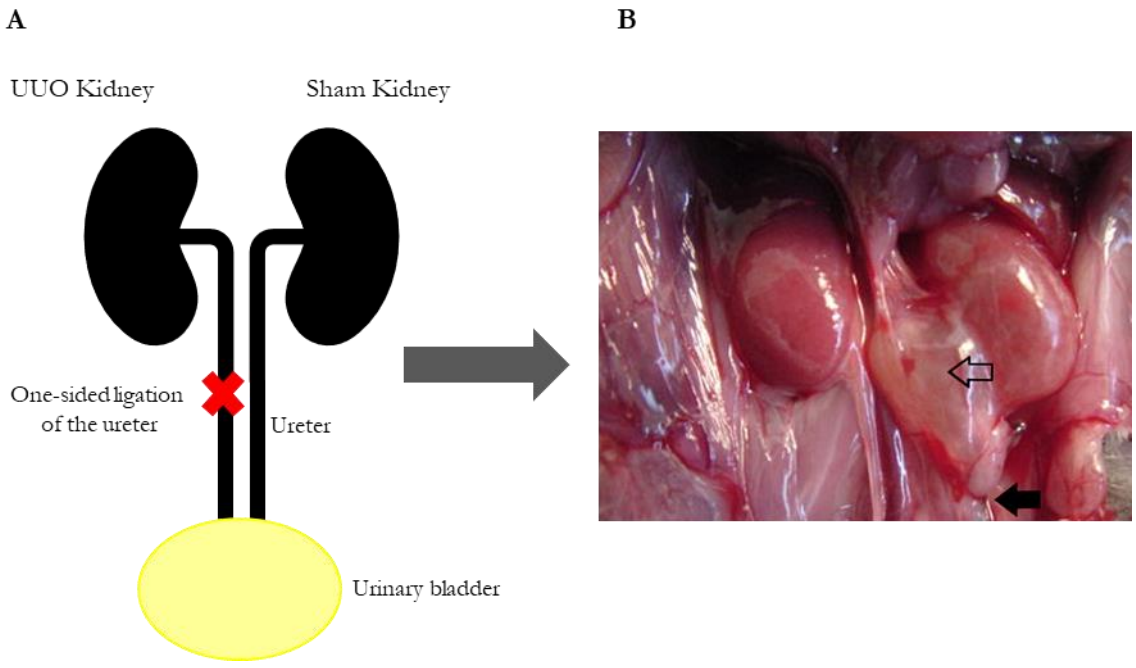

Figure 9: Overview of UUO model. In the UUO model, one ureter is ligated, resulting in unilateral obstruction (A). The other kidney undergoes a sham or placebo surgery. The resulting anatomy is shown in an *in-situ* photograph after a UUO surgery (B), whereby the solid black arrow points towards the ligated ureter and the hollow black arrow draws attention to the dilated renal pelvis filled with urine (Cohen et al. 2007; ©The American Physiological Society 2007). This obstruction leads to inflammation of the renal tissue, stimulating tissue fibrosis. The right kidney has undergone the sham surgery.

2.2.6.2 Treatment protocol

The treatment group received DSS at 30 mg/kg starting two days prior to the surgery until ten days post-surgery. Because the solvent for the DSS was a 0.9% NaCl solution, the control group

received treatment of 50 µl of NaCl in the same time frame (Table 12). Both the DSS and the NaCl were administered intraperitoneally after inhalation of 1 – 3% isoflurane.

After completion of the treatment on day 10 post-surgery, the mice were killed and both kidneys were carefully dissected. From each UUO and sham kidney, half was paraffinized by the Institute of Pathology of the UMCG for histological evaluation and the other half stored at -80°C.

Table 12: Protocol for *in-vivo* mouse treatment with DSS

	Mouse strain	**Group size**	**Intraperitoneal injection**	**Dosage**	**Procedure**
Control (Ctrl)	C57B/6	6	0.9% NaCl	50 µl	UUO Sham
Test	C57B/6	6	DSS	50 µl (30 mg/kg)	UUO Sham

The table provides information about the *in-vivo* mouse experiments performed in this study for both control and treatment groups, including mouse strain, group size, type of intraperitoneal injection, dosage of the applied substance, and the procedure performed on the mice. The same mouse breed and group size were used, and the same procedures performed in both the control and treatment groups.

2.2.7 PAS tissue staining

PAS staining is used to detect polysaccharides in tissues. This staining method was applied to the kidneys of control and DSS-treated mice. As described in section 2.2.6.2, one half of each UUO and sham kidney was paraffinized and stored at 4°C. The fixed kidneys were then sectioned into approximately 5 µM slices using a Reichert-Jung microtome, placed on specimen slides, and re-fixated with paraffin for storage. Slide preparation was carried out by assisting laboratory personnel.

The slides were de-paraffinized by heating at 60°C for 2 h in a Robbins Scientific Incubator. Excess paraffin was removed in xylene, twice for 10 min each. Rehydration occurred in a descending alcohol series, beginning in 100% EtOH twice for 5 min, followed by 96% EtOH, 80% EtOH, 50% EtOH, 30% EtOH and ddH_20 for 5 min, respectively (Table 13).

Table 13: Protocol for rehydration of the specimen in preparation of PAS staining

Solution	Time [min]
Xylene	2 x 10
100% EtOH	2 x 5
96% EtOH	1 x 5
80% EtOH	1 x 5
50% EtOH	1 x 5
30% EtOH	1 x 5
ddH_2O	1 x 5

PAS tissue staining was performed according to the protocol from Carl Roth. After paraffin removal, the slides were treated for 10 min in a 1% periodic acid solution. The slides were then washed for 10 min under running tap water and rinsed in dH_2O twice for 2 min. Subsequently, the slides were incubated in Schiff's Reagent for 20 min and washed for 5 min in lukewarm tap water. Counterstaining occurred for 5 min in Mayer's hematoxylin solution, followed by another 10 min wash-cycle in running tap water. Finally, dehydration of the specimen was performed in an ascending alcohol series so that the mounting medium would adhere to the slide: 1 min in 96% EtOH, 4 min in 100% EtOH, and twice for 5 min in xylene.

PAS-stained slides were photographed with an Axiovert 25 inverted light microscope at 400x magnification. UUO kidneys of control and DSS-treated mice were then evaluated using a tubular damage score (TDS). Sham kidneys were only microscopically evaluated to rule out preexisting renal damage and did not receive a TDS. The TDS for UUO kidneys was determined qualitatively and semi-quantitively based on the degree of tubular dilation and on an evaluation of the condition of the tubular basement membrane. A score of 0 represents healthy renal tissue, attributed to regions with dense tissue, condensed nuclei, and no tubular dilation. A score of 1 represents mild damage reflecting regions with minor tubular dilation. A TDS score of 2 represents moderate damage and 3 represents severe damage with decreasing tissue density, increasing tubular dilation, as well as mounting glomerular basement membrane damage (Tampe et al. 2017).

2.2.8 Immunofluorescent tissue staining

Immunofluorescent tissue staining of mouse renal tissue was performed to enable an *in-vivo* quantification of certain proteins. α-Sma, Col1 and pSmad2 were chosen as proteins of interest.

2.2.8.1 Slide preparation for immunohistochemistry

All specimens were prepared and plated using the same method as described for PAS staining in section 2.2.7.

Prior to staining, the specimens were de-paraffinized by heating in a Robbins Scientific Incubator for 2 h at 60°C. To remove leftover paraffin, slides were incubated with xylene for 20 min twice. Afterwards, the kidneys were rehydrated in descending concentrations of ethanol in water (100%, 96%, and 70% for one minute each) and finally for 5 min in ddH_20 (Table 14).

Table 14: Protocol for rehydration of the specimen in immunofluorescent tissue staining

Solution	Time [min]
Xylene	2 x 20
100% EtOH	1 x 1
96% EtOH	1 x 1
70% EtOH	1 x 1
ddH_2O	1 x 5

An intermediate step for antigen retrieval was required for Col1 and pSmad2 detection. The slides were incubated in a citrate buffer, consisting of citric acid and Tween (pH 6) for 25 min at 65°C in a closed compartment. The slides were left to cool down in the heated citrate buffer for 10 min and were then washed for 5 min in PBS. α-Sma antigen detection did not require any form of antigen retrieval.

Following rehydration, blocking of unspecific antigen binding sites was performed. For blocking, a circle was drawn around each specimen with a water-repellent pen, thereby containing the administered solutions within the circle. Subsequently, all specimens were covered with approx. 30 µl of a 10% goat serum as the blocking reagent and incubated in a dark at room temperature for 1 h. Afterwards, the goat serum was removed with lint-free tissue from all tissue samples.

2.2.8.2 Antibody binding and nuclear staining

Immunohistochemistry was performed to visualize the protein expression of α-Sma, Col1 and pSmad2 in the mouse kidneys. The primary antibodies were diluted in blocking buffer according

to the manufacturer's instructions (Table 2). The blocking buffer consisted of 1% BSA and 0.1% Tween in PBS.

50 µl of the diluted primary antibody were pipetted onto each specimen. As described in section 2.2.8.1, the water-repellent circle around each specimen ensured that no liquid would escape to the sides and the applied antibody concentration would be upheld throughout the incubation process. The specimen slides were then incubated in a dark, humid chamber for 1 h at 37°C and then at 4°C overnight. On the following morning, the antibody solution was removed with lint-free tissue. Unbound antibodies were removed with washing with washing buffer (0.1% Tween in PBS) for 3 x 5 min.

Secondary antibodies were dissolved in the same solvent solution mentioned above (Table 3). 50 µl of the diluted antibody were pipetted onto each specimen and left to incubate for 45 min at 37°C in a humid darkened chamber. After removing the antibody solution with a lint-free tissue, the specimens were washed with the washing buffer as described above.

The final step of the immunofluorescent staining was the 4',6'-diamidino-2-phenylindole (DAPI) nucleic acid staining. Staining the nucleus allowed a differentiation of individual cells during analysis under the microscope. 300 nM of the DAPI staining solution were pipetted onto the specimen and left to incubate for 15 min at 37°C in a humid darkened chamber. The solution was then removed with a lint-free tissue, and the specimen was washed once for 5 min with the PBS solvent solution.

After the final removal of the washing solution, one drop of Mowiol mounting media was pipetted onto each specimen. The cover slip was placed on top, being careful to avoid the formation of air bubbles. Then specimen slide and the cover slip were sealed in an air-tight manner with Eukitt® quick-hardening mounting medium and left in a dark place to dry.

2.2.8.3 Quantitative analysis of fluorescence images

Fluorescence images were taken using an IX71 microscope with a U-RFL-T Fluorescence power supply and iCys Research Imaging Cytometer (Series: 5019 2004) at 400x magnification. The control and test groups with their individual UUO and sham tissues contained three biological replicates, respectively (Table 12). 30 technical replicates were generated photographically from each biological replicate.

A quantitative analysis of the images was performed using ImageJ. Color Thresholding allowed a removal of background noise and a focus on the fluorescent protein of interest. Using a paintbrush tool, artefacts, such as staining of arterial walls when quantifying interstitial α-SMA

expression, were blackened for an objective analysis. Standard size of the images used for analysis was 16-bit and 13.76 cm x 10.32 cm. Conversion to a grayscale image enabled a thresholding of the image, marking the regions exhibiting fluorescence over a defined threshold (Figure 10). The shading yielded an area given in percent of the total area of the image, allowing a quantitative comparison of the protein expression in each mouse. Thus, the mean of each data set with standard deviation could be analyzed.

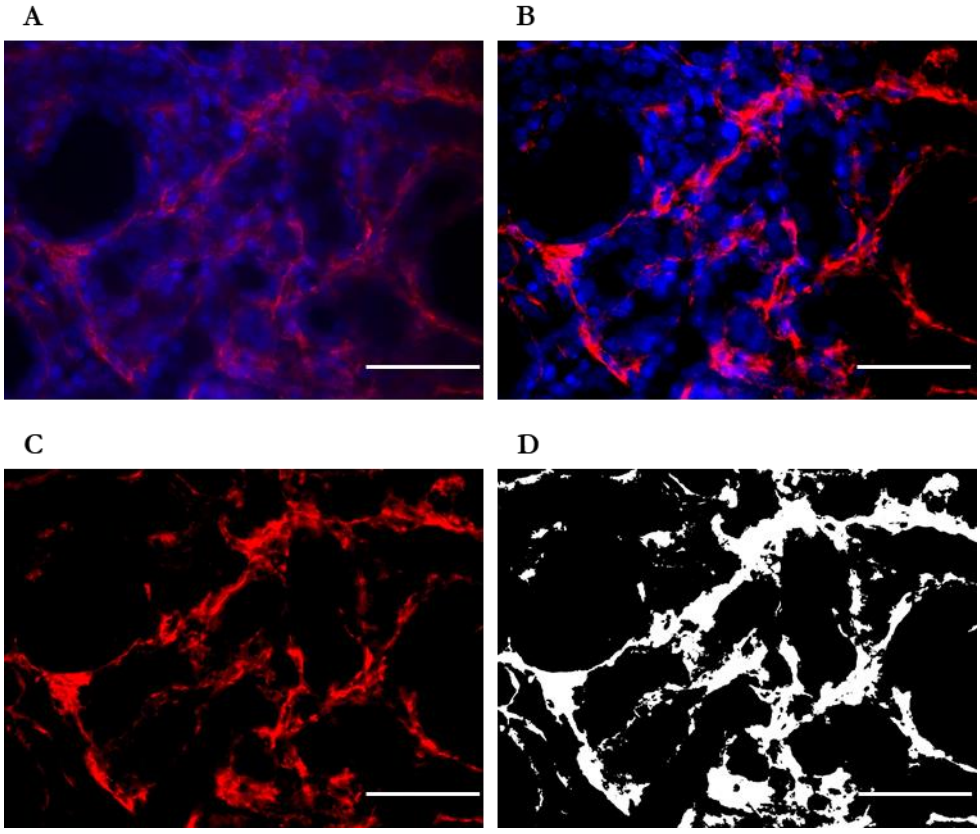

Figure 10: ImageJ Analysis of immunofluorescent tissue staining. The constellation of images demonstrates the analysis process of the immunohistochemical staining performed on mouse renal tissue, shown exemplarily using a picture of a UUO test specimen stained for α-Sma. First, the original fluorescence image of the kidney tissue is shown (A). Adjusting color levels eliminates background noise and artefacts (B). Next, the color channel designated to the DAPI nuclear stain was removed to focus on the protein of interest (C). Finally, the stained areas were converted to a greyscale image (D), then ready for quantification and statistical analysis. Scale bar: 50 µm.

3 Results

3.1 Effect of DSS on the viability and metabolism of renal cell line TK173

The MTT assay was performed to analyze the effect of different DSS concentrations on the viability and proliferation of TK173 human kidney fibroblasts under varying degrees of oxidative stress. As described in detail in section 2.2.2, the extinction in an MTT assay can be used to gauge cell viability and metabolism based on the presence of NADPH-dependent enzymes.

An exemplary 96-well plate of the MTT assay shows the timepoint after the 4 h incubation with the MTT solution, evident as the formazan coloring after crystal dissolution can be observed (Figure 11).

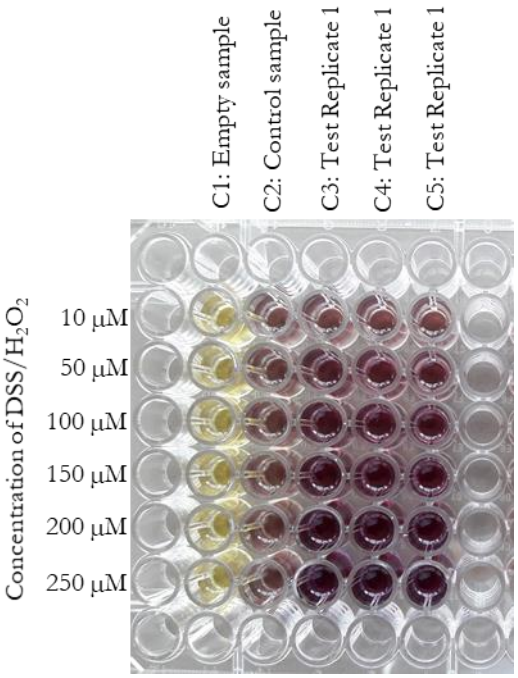

Figure 11: 96-well plate for MTT treatment protocol. The figure exemplarily illustrates the setup of the MTT assay. The blank samples are found in the far-left column, C1, containing no cells and solely cell culture DMEM with the corresponding addition of DSS or H_2O_2. The second column, C2, contains the negative control, i.e. untreated cells in cell culture DMEM. The columns C3 – C5 contain replicates of treated cells in cell culture DMEM with the addition of DSS or H_2O_2.

The wells on the far left, C1, contained solely cell culture medium (DMEM) with the corresponding supplement as a blank control. After treatment with the MTT dye, a pale-yellow color remained similar between all wells in this column. C2 contained the negative control, i.e. TK173 cells in cell culture DMEM without supplement. In comparison to C1, these wells changed

color, then exhibiting a light maroon/purple shade that remained constant within the entire column C2.

When considering the treatment wells, C3 – C5, different shades of maroon were seen with changing concentrations of the supplementary treatment. To objectify these observations, the photometric extinction of each well was measured (Figure 12). In further descriptions, extinction measurements will be presented with reference to "cell viability" as a reflection of cellular metabolism and proliferation.

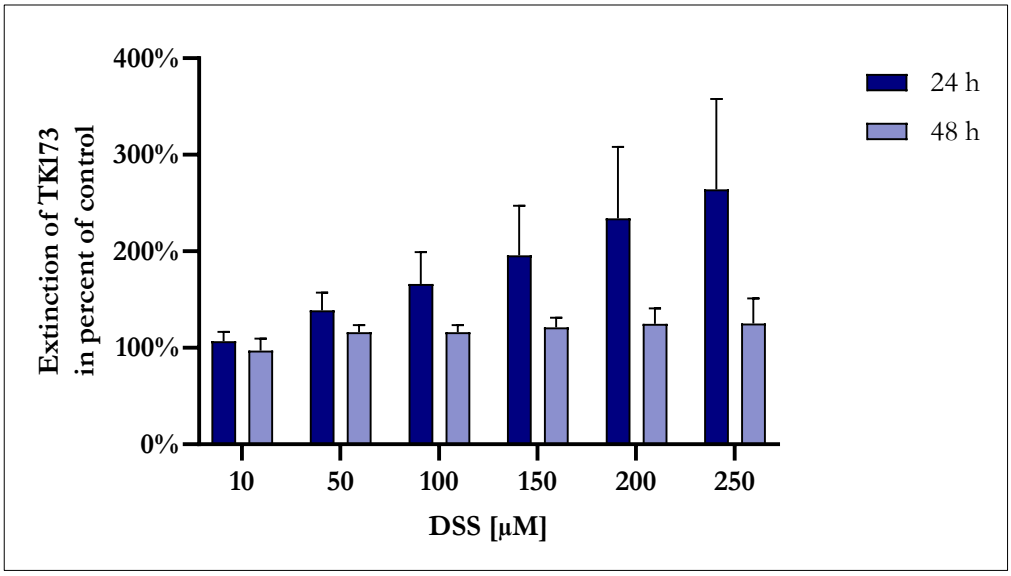

Figure 12: Cell viability and proliferation of TK173 cells treated with varying concentrations of DSS compared to control. The x-axis lists the different concentrations of DSS in µM used to treat TK173 cells. The dependent factor, the cell viability and proliferation, is shown on the y-axis as a percent of the treated cells compared to untreated control cells. MTT was repeated on three different plates with three technical replicates each. Each mean value is shown with its positive standard deviation. During the first 24 h, a nearly linear increase of cell viability in accordance with increasing DSS concentration can be observed. After 48 h, this increase in relation to increasing DSS concentration is only minimal.

Concomitant with the visual colorimetric observations, the measurements after 24 h showed a nearly linear increase of cell viability and proliferation dependent on the increasing concentration of DSS, more than doubling between the treatment with 10 µM DSS and the treatment with 250 µM DSS. A relevant increase in standard deviation with increasing DSS concentration was also noted. After 48 h there was no further significant increase in cell viability in accordance with the varied DSS concentration. This stagnation was consistent in measurements after 72 h (data not shown).

In a further experimental setting, the effect of different H_2O_2 concentrations on TK173 was analyzed (Figure 13A). Finally, a third setup evaluated the effect of DSS on cells undergoing oxidative stress through H_2O_2 by pre-treating TK173 cells with 200 μM DSS over a period of 24 h and subsequently stressing the cells with the same concentrations of H_2O_2 presented above (Figure 13B).

A reduction of the cell viability with increasing H_2O_2 concentration was evident, with values consistently < 100% at both 24 h and 48 h (Figure 13A). Between 10 – 100 μM, the decline in cell viability was steep, while after the addition of 100 μM H_2O_2, the steep decline halted and gained again insignificantly ($p > 0.05$) between 100 – 250 μM H_2O_2. When considering the treatment with 10 μM H_2O_2 at the different time frames, a notable though insignificant ($p > 0.05$) increase in cell viability was seen after 48 h in comparison to the measurement after 24 h. At an H_2O_2 concentration of 50 μM, however, the extinction after 48 h remained nearly the same as the extinction after 24 h and failed to increase.

When considering the combined treatment (Figure 13B), a similar trend could be seen: all H_2O_2 concentrations led to a reduction of the cell viability in comparison to control. However, in this case the continual decrease was evident up to 200 μM, at which the lowest cell viability and proliferation rate was reached. This signified a shift to the right on the x-axis in comparison to Figure 13A, at which the minimum was reached more quickly (at 100 μM H_2O_2). In the final increment, between 200 – 250 μM of H_2O_2 addition, a slight but insignificant increase of cell viability was observed again. Additionally, the photometric measurement after 48 h consistently showed an increase in cell viability in comparison to the measurement after 24 h. This was most evident at 10 μM, at which after 48 h the cell viability almost reached the level of the control cells.

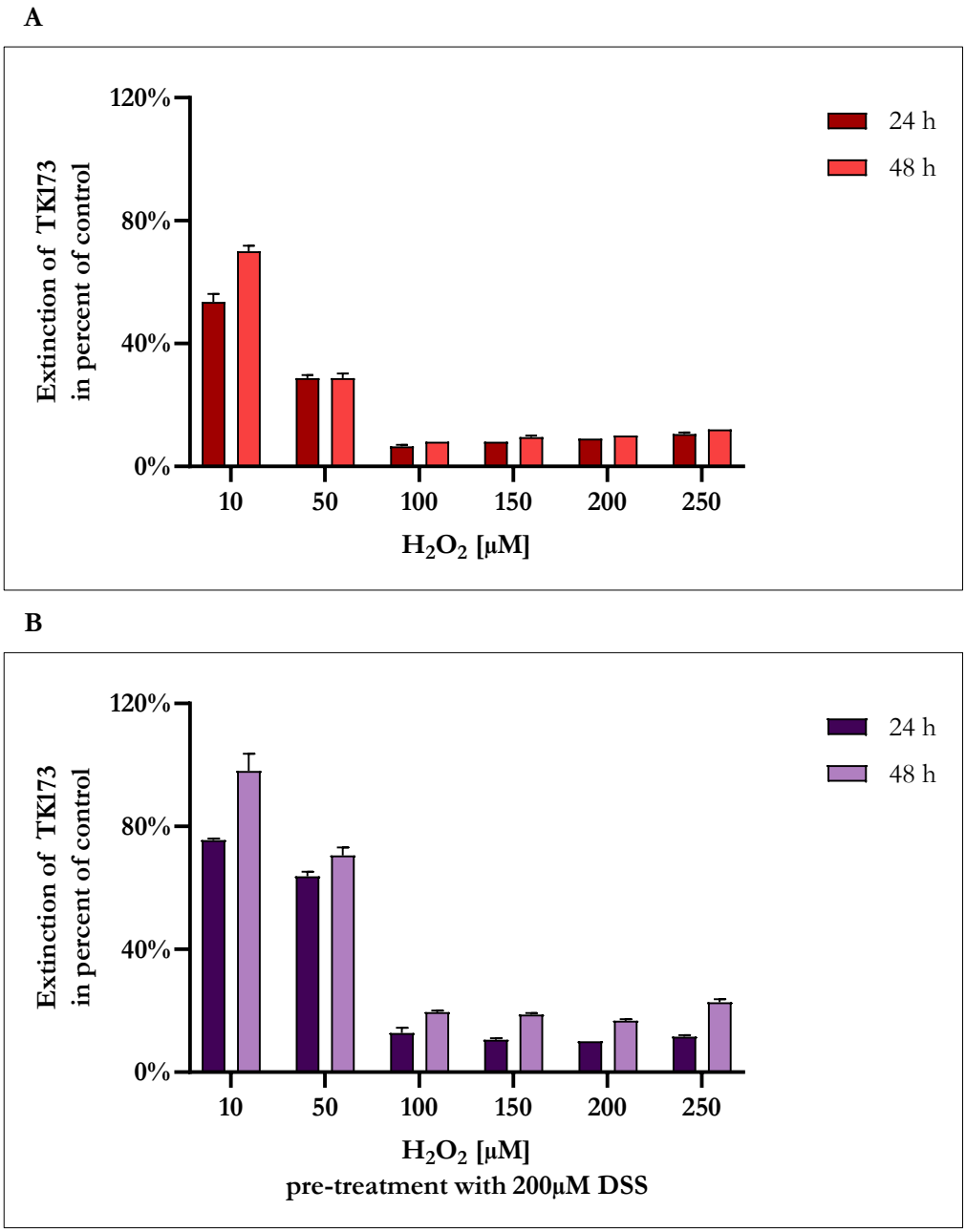

Figure 13: Cell viability ratio of TK173 cells treated with varying concentrations of H_2O_2 without and with DSS pre-treatment. The x-axes list the different concentrations of H_2O_2 in µM used to treat TK173 cells. The cell viability as the dependent factor is shown on the y-axes as a percent of the treated cells in relation to untreated control cells with its positive standard deviation. Both MTT setups were repeated on three different plates with three technical replicates each. The mean cell viability of TK173 cells after treatment with varying concentrations of H_2O_2 without DSS pre-treatment is shown (A). While it is reduced in comparison to control at all H_2O_2 concentrations (extinction < 100%), the cell viability remains relatively high at 10 µM and 50 µM. Nonetheless, a steep decline is evident between 10 – 100 µM H_2O_2 and then increases insignificantly between 100 – 250 µM. An insignificant increase in cell viability can be seen after 48 h in comparison to the measurement after 24 h. Next, the mean cell viability of TK173 cells after treatment with varying concentrations of H_2O_2 with DSS pre-treatment is presented (B). A steady decrease in cell viability is seen between 10 – 200 µM H_2O_2 concentration. After 250 µM H_2O_2 treatment, a slight increase is seen again. The measurement after 48 h consistently presents a measurable though non-significant increase in extinction in comparison to the measurement after 24 h.

The MTT cell viability assays performed on TK173 cells with and without 200 µM DSS pre-treatment were directly compared (Figure 14). Analysis is demonstrated exemplarily for H_2O_2 concentrations of 10 µM and 50 µM based on the prominent changes described in Figure 13A and Figure 13B. In all cases, a highly significant increase in cell viability was observed in the cells pre-treated with DSS in comparison to those only stressed with H_2O_2, without the pre-treatment. The effect was most apparent when considering the cells stressed with 50 µM H_2O_2. In this case, incubation for 24 h resulted in an absolute increase in cell viability of 35%, and after 48 h an absolute increase of 41.75% could be observed.

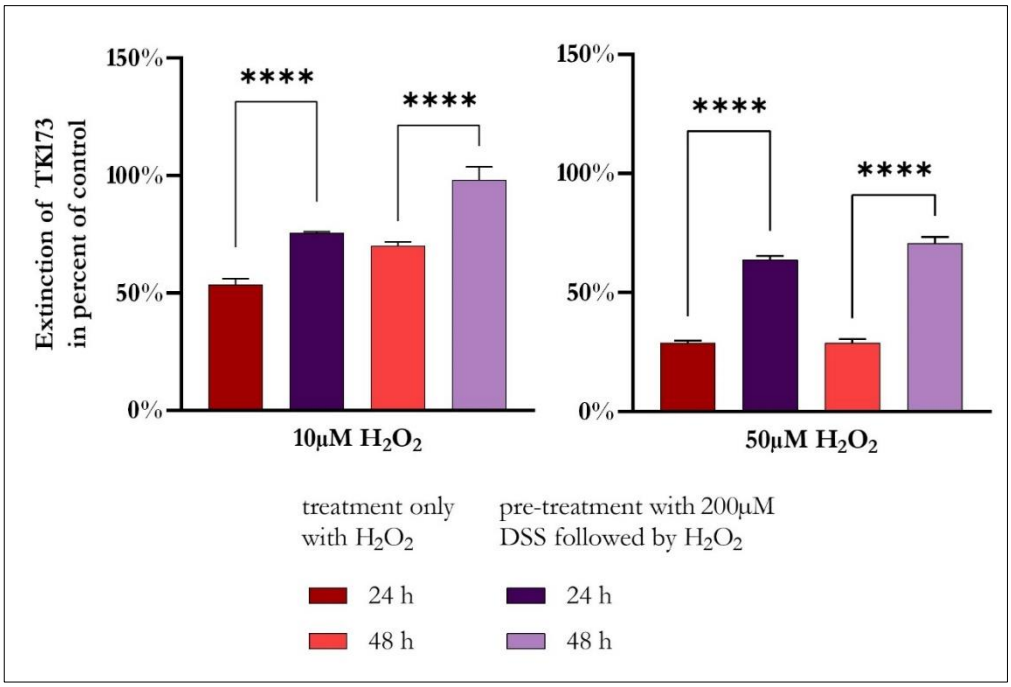

Figure 14: Comparison of cell viability in TK173 cells after H_2O_2 stress with and without DSS pre-treatment. The x-axis lists the different concentrations of H_2O_2 in µM used to treat TK173 cells. The dependent factor, the cell viability, is shown on the y-axis as a percent of the treated cells in relation to untreated control cells. The figure shows the comparison of the cell viability at H_2O_2 concentrations of 10 µM and 50 µM between cells not pre-treated and those pre-treated with 200 µM DSS over 24 h prior to the mentioned H_2O_2 exposure. A highly significant increase in cell viability was seen after both 24 h and after 48 h in cells receiving the DSS pre-treatment. Significance was defined in an unpaired, two-tailed t-test: ****$p < 0.0001$.

In the MTT cell viability assay, DSS treatment led to a linear increase in cell viability and proliferation of TK173 cells in accordance with increasing DSS concentration. While H_2O_2 consistently caused a reduction of cell viability, treatment with DSS prior to H_2O_2 exposure significantly augmented cell viability and proliferation in comparison to those cells not receiving the DSS pre-treatment.

3.2 Effect of DSS on intracellular ROS production

FACS was used to verify the potential antioxidative effect of DSS in TK173 cells stressed with H_2O_2. The method using CM-H_2DCFDA as a fluorescent marker of intracellular ROS in TK173 cells is described in section 2.2.3.

ROS levels in untreated and stressed cells were compared to those stressed and pre-treated with DSS (Figure 15). In both untreated and treated TK173 cells, exposure to H_2O_2 caused an increase in ROS detection in comparison to its unstressed counterpart; however, only in the untreated group was this difference significant. When comparing the unstressed groups ("untreated" vs. "treated"), the addition of DSS had no significant effect on cellular ROS levels. An appraisal of the stressed cells ("untreated H_2O_2 vs. treated H_2O_2") revealed that the pre-treatment with DSS led to a significant reduction of ROS of approx. 25% in comparison to the cells not receiving the DSS pre-treatment. Furthermore, among the cells treated with DSS ("treated" vs. "treated H_2O_2)", stress with H_2O_2 did not cause a significant increase of ROS.

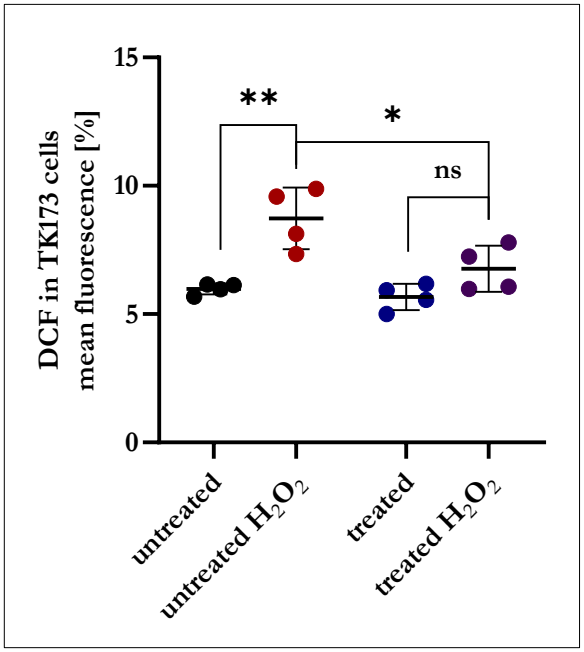

Figure 15: Mean ROS concentration in TK173 cells. The figure compares ROS concentrations, detected with a fluorescent DCF marker, in TK173 cells after undergoing different treatments. The mean was calculated from n = 4 evaluating 10,000 events per replicate. The x-axis describes the different treatment groups, i.e. TK173 cells pre-treated or not pre-treated with 200 µM DSS and cells stressed or not stressed with 100 µM H_2O_2. The y-axis defines the ROS concentration in percent of all analyzed events within the defined group. The left two data sets show ROS levels in DSS-untreated TK173 cells. The exposure to H_2O_2 led to a significant increase in ROS detection. When comparing the two sets of unstressed cells ("untreated" vs. "treated"), no significant different in ROS was observed. The right two data sets present ROS concentration in TK173 cells treated with DSS. As in the untreated groups, oxidative stress caused by H_2O_2 led to an increase in ROS levels; however, the difference was not significant. A comparison of the two stressed cells groups ("untreated H_2O_2" vs. "treated H_2O_2") shows a significant reduction of ROS levels in those TK173 cells receiving the DSS pre-treatment. Significance was defined in an unpaired, two-tailed t-test: *$p < 0.05$, **$p < 0.005$.

3.3 Effect of DSS on protein expression in TK173 cell line

For protein expression analysis, Western blot was conducted as described in section 2.2.5. VIM, FN1, and SOD1 were chosen as proteins of interest due to their involvement in the pathogenesis of tissue fibrosis and/or their role in oxidant-antioxidant homeostasis. Cells were evaluated in differentially treated groups: "untreated unstressed" (control), "treated unstressed", "untreated stressed", and "treated stressed". GAPDH was consistently used as housekeeping protein.

Regarding VIM expression, various bands with different intensities were observed (Figure 16A), representing the four different VIM forms defined by their molecular weight: VIM I has the lowest molecular weight, therefore traveling further in SDS-PAGE and transferred onto the membrane farther down. VIM II – IV have higher molecular weights and are thus seen higher on the membrane. The varying intensities correlate with the applied treatment, illustrated at the bottom of the figure.

Overall VIM protein expression in TK173 cells was analyzed in ratio to control (Figure 16B). The average of n = 3 replicates showed that the treatment with DSS led to a significant increase of VIM expression, a factor of approx. 1.9 in comparison to control. Stress with H_2O_2, on the other hand, led to no significant change of VIM expression in ratio to control. Pre-treatment with DSS prior to H_2O_2 exposure resulted in a minor but significant increase of VIM expression, of 1.18 ± 0.05. This was a slight increase in comparison to the VIM expression of untreated stressed ("H_2O_2") cells, but visibly less than the treated unstressed group. Nonetheless, analysis revealed a significance in differential VIM expression when comparing the untreated stressed and the treated stressed TK173 cells.

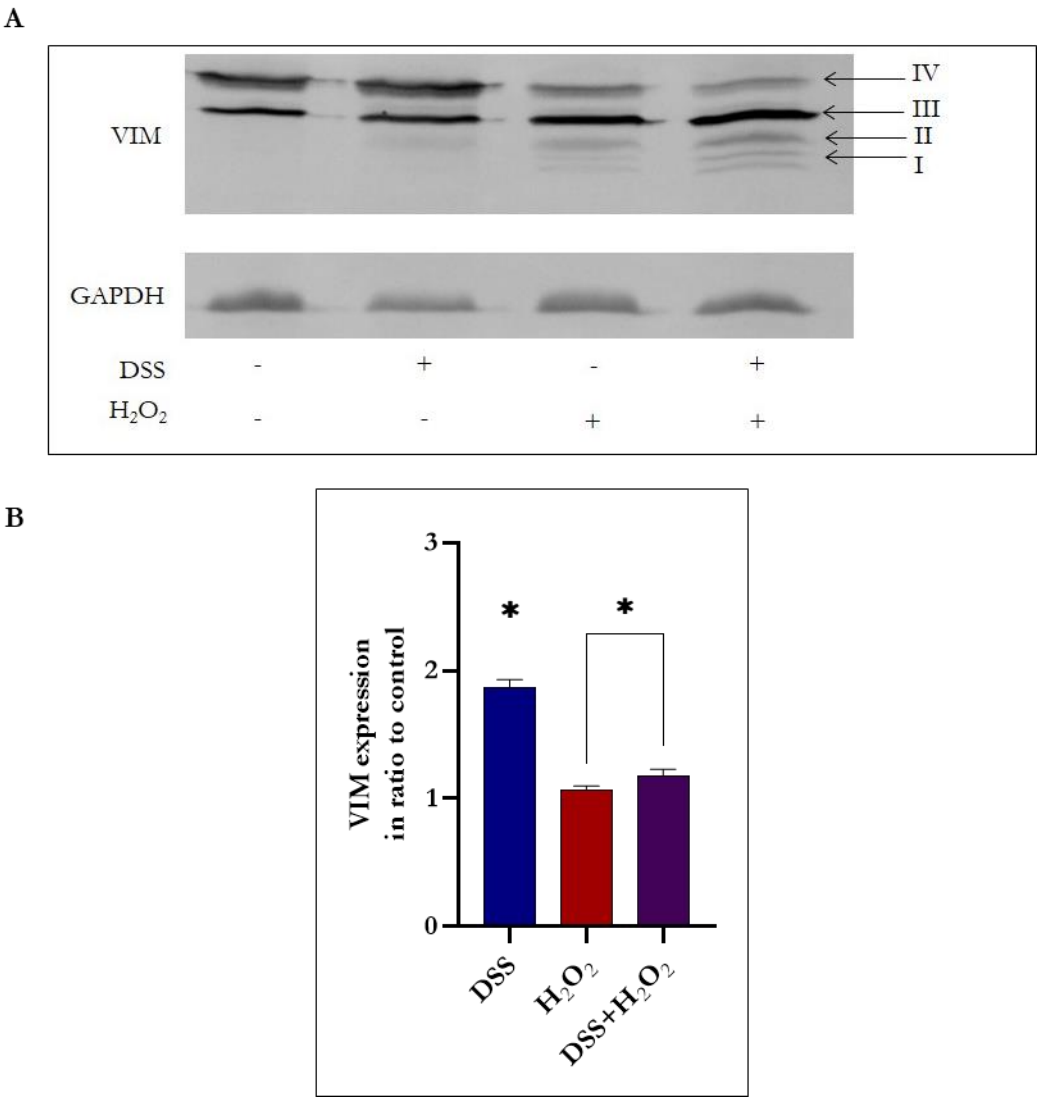

Figure 16: VIM expression in TK173 cells. In an exemplary Western blot of VIM protein expression in TK173 cells, the bands in the upper row show VIM expression in TK173 cells after treatment with the described protocol (A). Different VIM forms appear in each lane. The descriptions on the right side define the bands from lowest to highest molecular weight as VIM I (below) to VIM IV (above) (Buchmaier et al. 2013). VIM bands III and IV were highly expressed in the control group. These same two bands remained consistent in the group treated with DSS, however, a very faint band of slightly lower molecular weight, VIM II also appears. In the group treated with H_2O_2, VIM IV faded slightly, while VIM III retained the same expression level as in the control and the DSS group. We observed an increase in the expression of VIM I and II of lower molecular weight in comparison to the previous test groups. In DSS and H_2O_2 combined treatment, the expression of VIM I and II increased while VIM III and VIM IV stayed approximately the same. The middle row shows GAPDH expression for each corresponding sample, acting as the loading control. The labels in the bottommost row define the received treatment of the corresponding TK173 cells in each lane. In the bar graph analysis of VIM protein expression in TK173 cells, the x-axis designates the treatment groups (B), corresponding with the bottommost descriptions in image A. VIM expression in ratio to control TK173 cells is represented in the y-axis. These mean values, calculated from a total of n = 3, were normalized to the housekeeping protein GAPDH and calculated in ratio to the control sample. Thereby, the intensity of the control sample was equal to 1 (not shown) and the intensity of the displayed treatment groups represented as a multiple of the control. TK173 cells treated with DSS displayed a significant increase in VIM expression, while the stressed and treated stressed groups presented no significant differential VIM expression in ratio to control. Comparison of stressed and treated stressed TK173 cells, however, results in a significant increase in VIM expression in cells with the DSS pre-treatment. Significance was defined in an unpaired, two-tailed t-test: *$p < 0.05$.

In further analysis, the individual VIM forms VIM III and IV were examined, the results are presented below in Figure 17A and Figure 17B, respectively. An increase in VIM III expression in comparison to control TK173 cells was seen in all test groups (Figure 17A). Among the groups, no significant difference in VIM III intensity could be objectified. Additionally, when comparing the treated stressed treatment group with the untreated stressed cells, an unpaired two-tailed t-test revealed no statistical significance in VIM III expression changes. Finally, a relatively high standard deviation of the values, in comparison to the standard deviation of the overall VIM expression was noted (Figure 16B).

A similarly high standard deviation was seen in graph B, presenting VIM IV expression intensity in TK173 cells. As with VIM III, treatment with DSS led to a near doubling of VIM IV expression in ratio to control. Stress with H_2O_2, on the other hand, reduced VIM IV expression. In the combined treated stressed cells, VIM IV expression increased again slightly, though non-significantly in comparison to the untreated stressed cells.

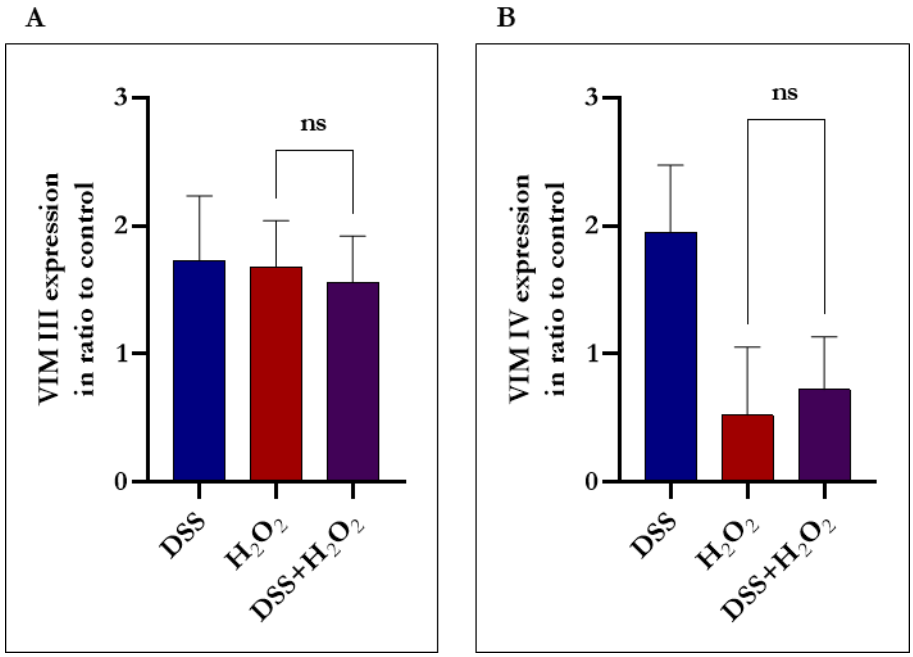

Figure 17: VIM III and VIM IV expression in ratio to control in Western blot. Bar graph representation of VIM III (A) and VIM IV (B) expression with positive standard deviation. All values were normalized to the loading control GAPDH and calculated in ratio to the control sample. Thereby, the intensity of the control sample was equal to 1 (not shown) and the intensities of the treatment groups were represented as a multiple of the control. All treatment combinations led to an insignificant increase in VIM III expression in TK173 cells. Additionally, no significance was observed between the treatment groups. When considering VIM IV in image B, DSS treatment again caused an increase in protein expression. The untreated stressed cells, on the other hand, displayed a reduction of VIM IV expression which increased slightly with the addition of DSS pre-treatment. This increase, however, was not significant. Significance was defined in an unpaired, two-tailed t-test: *$p < 0.05$.

TK173 cells appeared to express different VIM forms with varying intensities depending on the applied treatment. Overall, DSS caused an increase in VIM expression, confirmed when regarding the individual forms VIM III and VIM IV. Exposure to oxidative stress with H_2O_2 resulted in inconsistent changes in VIM expression, depending on the form of interest.

In the following, FN1 protein expression was determined and analyzed identically to above. FN1 is a protein of very high molecular weight, therefore hardly traveling through the gel in SDS-PAGE, and transferred at the top of the nitrocellulose membrane (refer to section 1.3.2). In the upper row, varying intensities of FN1 became evident (Figure 18A). Visually, the cells treated with solely DSS presented a band with slightly higher FN1 intensity than the control cells. Untreated stressed cells, on the other hand, exhibited lower FN1 expression. Treated stressed TK173 cells showed a slight increase of FN1 protein expression in comparison to the untreated stressed cells but remained downregulated in comparison to the treated unstressed cells.

These observations were objectified through analysis of the expression intensities of FN1 in TK173 cells after H_2O_2 and DSS treatments with $n = 3$ (Figure 18B). Treatment with DSS resulted in an increase of FN1 expression, doubled in ratio to control TK173 cells. Due to the high standard deviation, this change in expression was not significant ($p > 0.05$). Untreated stressed cells displayed a significant, approx. 50% reduction of FN1 expression in ratio to the control group. Comparison of untreated stressed cells to treated stressed cells did not result in a significant differential FN1 expression, although the pre-treatment with DSS led to a slight increase of FN1 expression. Overall, FN1 expression was still reduced in treated stressed cells in comparison to control.

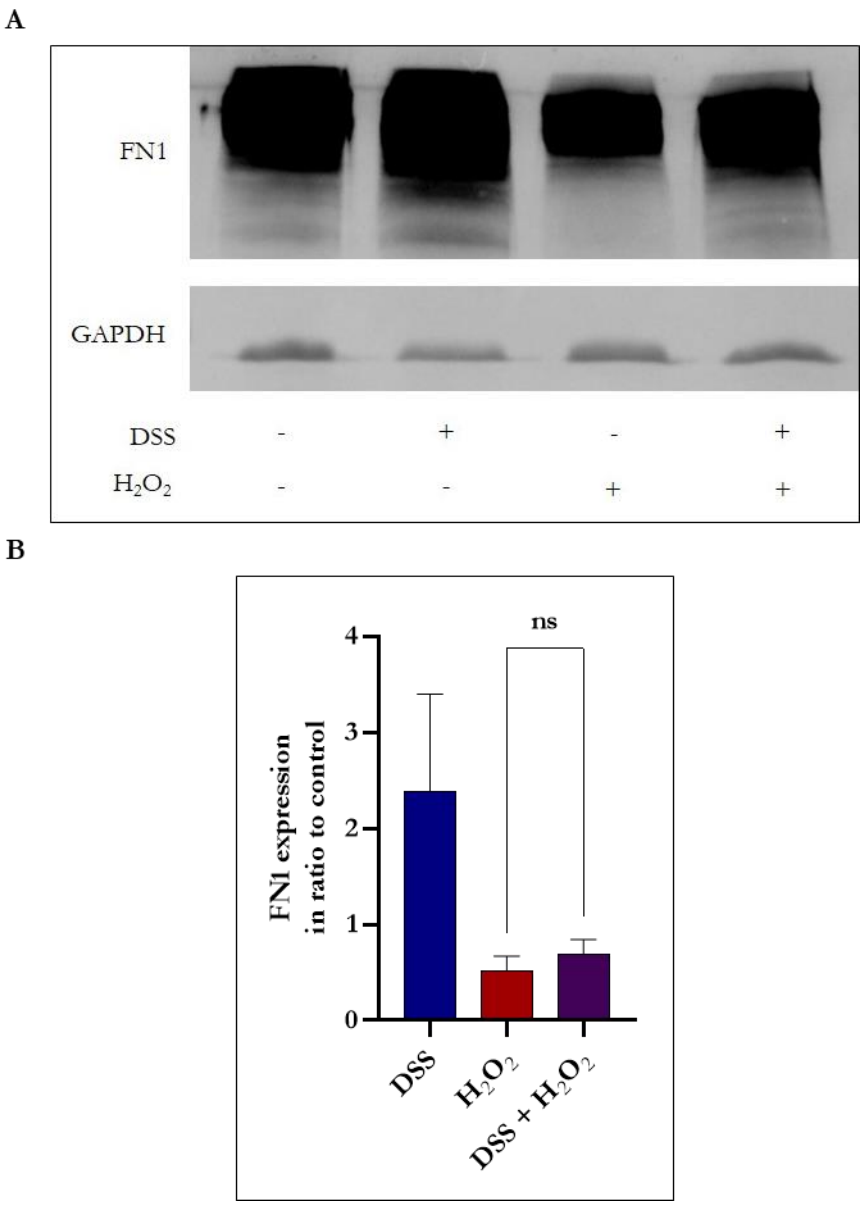

Figure 18: FN1 expression in TK173 cells. In the exemplary Western blot of FN1 protein expression in TK173 cells, the bands in the first row show FN1 expression in TK173 cells after treatment with the described protocol (A). Visually, treated unstressed cells displayed a higher intensity of FN1 expression than control, while in untreated stressed cells, FN1 expression appeared markedly reduced. Under the combined treatment, treated stressed TK173 cells showed a slightly higher FN1 expression than the untreated stressed cells, but still overall reduced in comparison to control. The middle row shows GAPDH expression for each corresponding sample, acting as the loading control. The labels farthest down define the received treatment of the corresponding TK173 cells in each lane. When quantifying the expression of FN1, the x-axis designates the treatment groups (B), corresponding with the bottommost descriptions in image A. FN1 expression in ratio to control TK173 cells is represented in the y-axis. These mean values, calculated from a total of n = 3, were normalized to the housekeeping protein GAPDH and calculated in ratio to the control sample. Thereby, the intensity of the control sample was equal to 1 (not shown) and the intensity of the displayed treatment groups represented as a multiple of the control. DSS-treated cells showed an upregulation of FN1 protein expression. In untreated stressed cells FN1 protein expression was reduced. In the treated stressed TK173 cells, FN1 expression was still reduced in ratio to control, though non-significantly elevated in relation to the untreated stressed cells. Significance was defined in an unpaired, two-tailed t-test: *$p < 0.05$.

Finally, SOD1 protein expression was analyzed (Figure 19). In comparison to the control sample, the SOD1 expression in all test groups seemed to be upregulated. Subjectively, the increase continued gradually in the samples from left to right (Figure 19A).

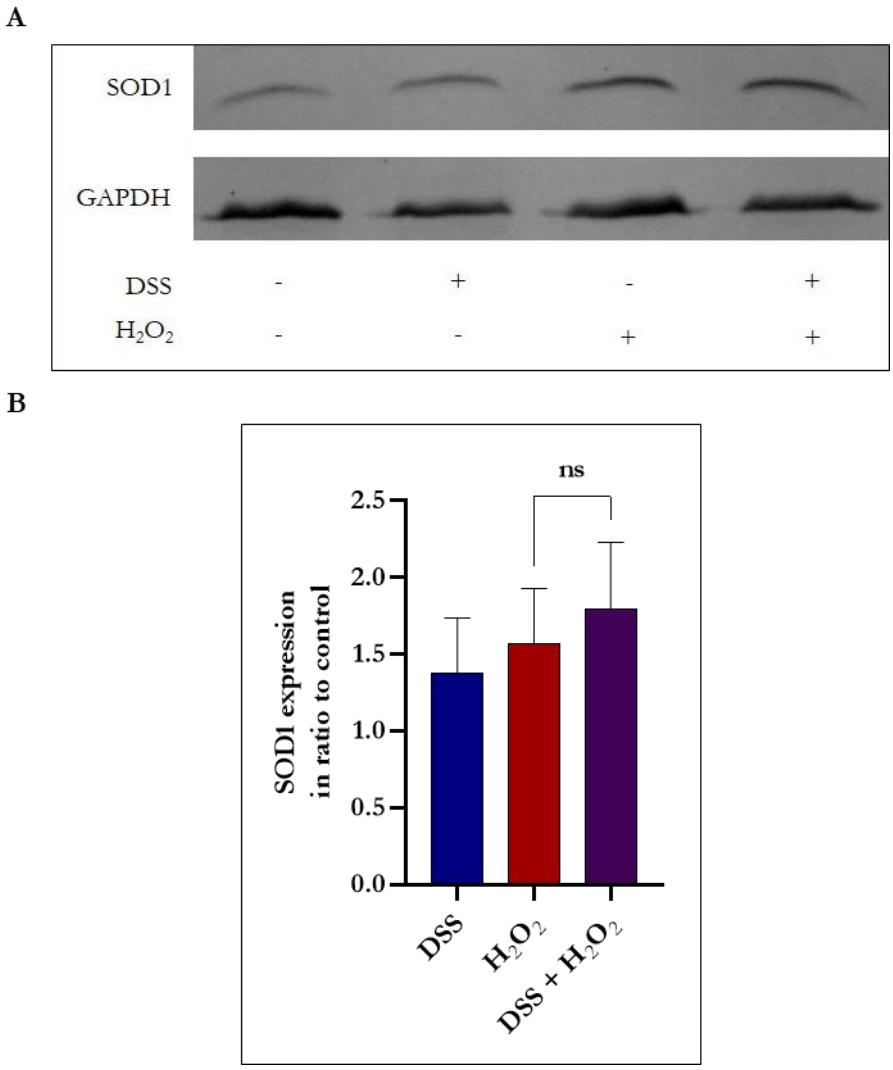

Figure 19: SOD1 expression in TK173 cells. In the exemplary Western blot of SOD1 protein expression in TK173 cells, the bands in the first row show SOD1 expression in TK173 cells after treatment with the described protocol (A). Visually, all treatment groups presented an upregulation of SOD1 expression intensity in relation to the control cells. Furthermore, a general trend of increasing intensity from left to right was seen. The middle row shows GAPDH expression for each corresponding sample, acting as the loading control. The labels farthest down define the received treatment of the corresponding TK173 cells in each lane. In the bar graph analysis of SOD1 protein expression in TK173 cells, the x-axis designates the treatment groups (B), corresponding with the bottom-most descriptions in image A. SOD1 expression in ratio to control TK173 cells is represented in the y-axis. These mean values, calculated from a total of n = 3, were normalized to the housekeeping protein GAPDH and calculated in ratio to the control sample. Thereby, the intensity of the control sample was equal to 1 (not shown) and the intensity of the displayed treatment groups represented as a multiple of the control. Corresponding with the visual analysis of image A, treated unstressed cells displayed a non-significant increase of SOD1 expression. In untreated stressed cells, SOD1 expression was increased once again. Treated stressed cells presented the highest rate of SOD1 expression intensity, though with no significant difference in comparison to control nor to untreated stressed TK173 cells. Significance was defined in an unpaired, two-tailed t-test: *$p < 0.05$.

The described observations were objectified in the same manner using a bar graph analysis of SOD1 expression intensity in ratio to control with n = 3 (Figure 19B). Treated unstressed TK173 cells showed a slight upregulation of SOD1 expression in ratio to control, by a factor of approx. 1.4. In comparison, untreated stressed cells showed again a slight up-regulation of SOD1 expression (x 1.57) compared to control. Ultimately, treated stressed cells presented the highest SOD1 expression (x 1.8) compared to control. None of these results reached significance, defined as $p < 0.05$.

3.4 Tubular Damage Scoring of PAS tissue stains

PAS tissue staining was performed on renal tissue of control and DSS-treated mice (Figure 20). Considering the extent of tubular dilation and injury to the basement membrane, a qualitative and semi-quantitative TDS was determined for each specimen objectifying the degree of tissue injury that had occurred through the UUO. For a detailed description of the TDS criteria see section 2.2.7.

When considering the PAS stained renal tissue, different trends can be observed when comparing the progression from image A to image D. In images A and B, for example, the basement membrane is clearly identifiable, building a dark margin under the tubular epithelial cells. This is not as clear in images C and D. Furthermore, changes in the nuclei and in the degree of tubular dilation are evident. In image A, the nuclei are large and condensed, and the tubules have a very narrow lumen, resulting in a picture that overall appears darker than images B – D. In image B, individual tubules with minor dilation can be seen. Thereby, and due to the less dense nuclei, the image already appears lighter. The extent of dilation as well as the absolute number of dilated tubules increases steadily when continuing from image B to C and D, so that image D shows a significant increase in lumen area in comparison.

The TDS was only applied to UUO kidneys, as the sham kidneys were only microscopically considered to rule out possible preexisting kidney damage. Ten images in three separate tissue samples were analyzed, yielding n = 30 technical replicates per biological replicate. Three biological replicates per control and treatment group, respectively, were evaluated (refer Table 12). Pie graph representation was included to reflect the TDS variance within each biological replicate (Figure 21A).

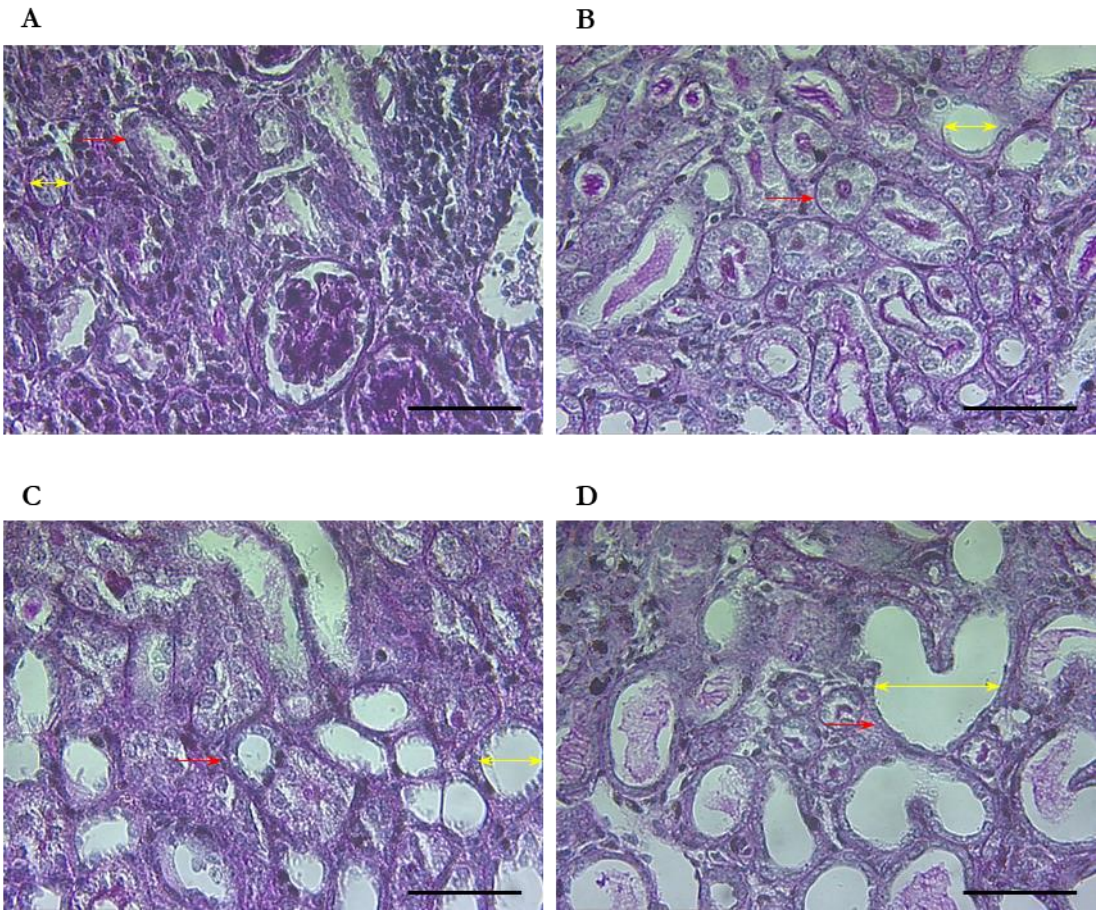

Figure 20: Examples of PAS tissue stains focusing on TDS criteria. PAS stains of mouse UUO kidneys at 400x magnification are shown. Yellow arrows indicate the diameter of a representative kidney tubule. Red arrows mark the basement membrane. The TDS of each specimen was determined according to the degree of tubular dilation and the quality of the basement membrane (Tampe et al. 2017). In the PAS stain showing a TDS of 0, representing healthy tissue, the tissue and nuclei are dense, resulting in a subjectively darker image (A). A score of 1 represents mildly damaged tissue (B), a score of 2 represents moderately damaged tissue (C), and a score of 3 represents severely damaged tissue (D). Scale bar: 50 μm.

Upon consideration of the graphs, it became evident that only one control replicate received a TDS of 0 and this in only one image. The replicates in the DSS test group, on the other hand, all received scores of zero, albeit in varying frequency. Furthermore, all biological replicates in the control group received several TDS of 3, reflecting severe tissue damage, while of the test replicates, one replicate did not receive any TDS of 3. Next, the mean TDS was determined from the abovementioned 30 technical replicates and illustrated in a bar graph diagram (Figure 21B). The replicates within the test group received a TDS ranging between 1.33 – 1.63. All mean values were therefore lower than those in control, which ranged from 1.73 – 1.83.

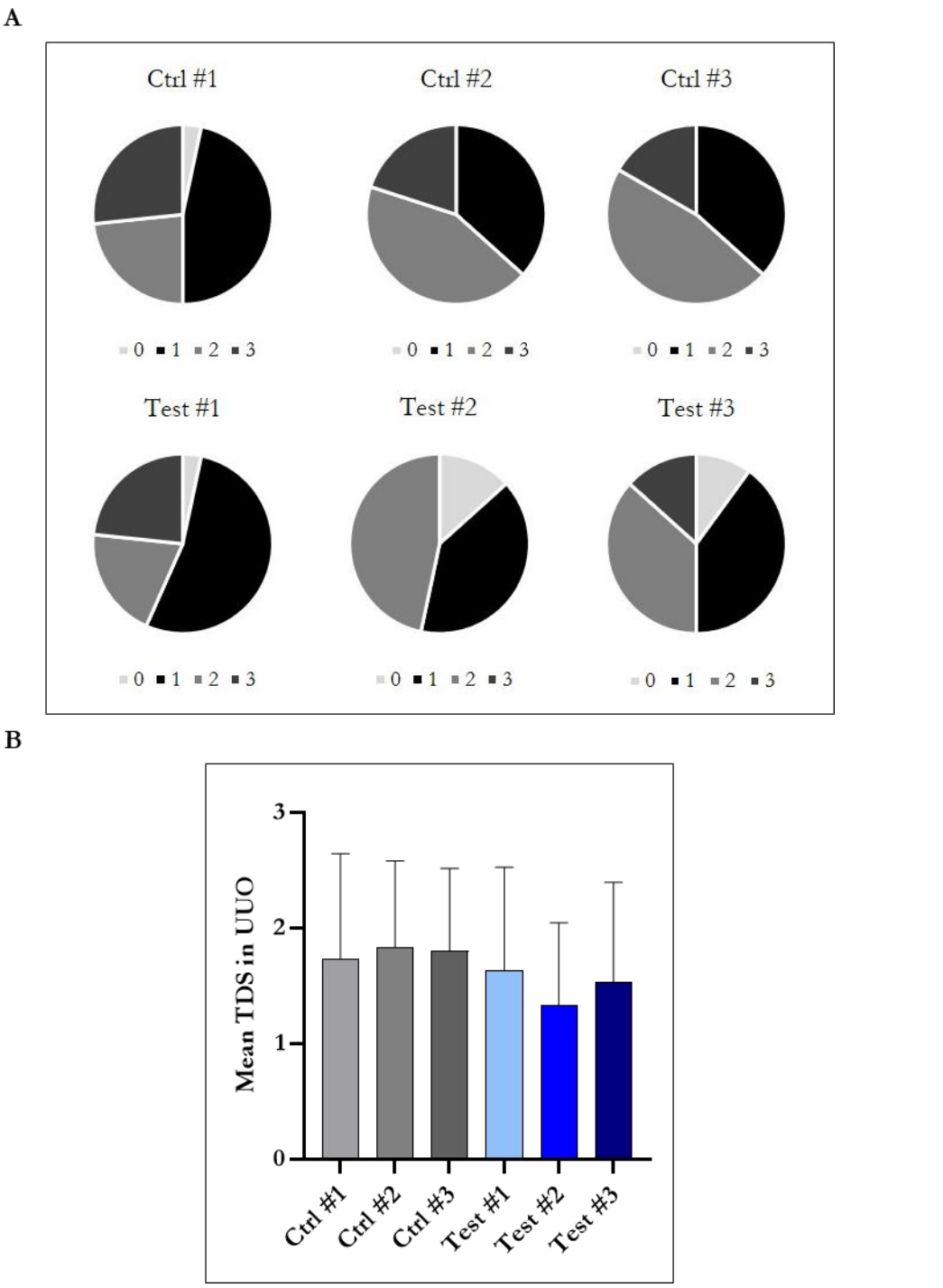

Figure 21: TDS distribution in individual UUO kidneys. Image A depicts pie graph representation of TDS scores per biological replicate. Each graph portrays the distribution of scores in a total of n = 30 analyzed images. The top row shows the TDS distribution of UUO kidney tissue of the three mouse biological control replicates treated with NaCl. The bottom row shows the TDS distribution of UUO kidney tissue of three mouse biological test replicates treated with DSS. In the control replicates, only Control#1 received a TDS of 0, reflecting healthy kidney tissue. This differs from the treatment replicates, in which all received at least one TDS of 0. Furthermore, all control replicates received a TDS of 3, representing severe tissue damage, while in the treatment group, only 2/3 of the biological replicates received a TDS of 3. Image B illustrates the mean TDS of each biological replicate. The x-axis defines the individual biological replicate and the y-axis marks the mean TDS. Each value is portrayed as mean of n = 30 with its positive standard deviation. The grey-shaded bars to the left present the mean TDS of control replicates. The blue-shaded bars to the right present the mean TDS of test replicates, treated with DSS. Overall, control replicates present a higher TDS than the test replicates. There was no significant difference in TDS between the individual replicates.

When comparing the overall mean TDS of test and control, a significant reduction was seen in the DSS-treated test group (Figure 22).

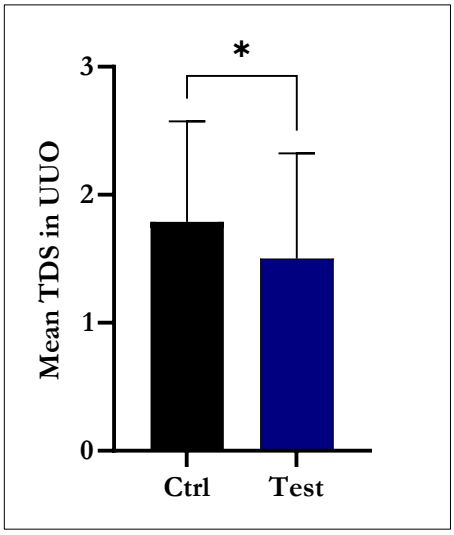

Figure 22: Mean TDS comparing control and test. The bar graph compares the mean TDS of UUO kidneys in control and test. The x-axis defines the treatment group and reflects the replicates shown in Figure 21. The y-axis marks the mean TDS, presented as a mean of 90 values (30 technical replicates per 3 biological replicates). Comparison of the mean TDS yields a significant reduction in the test group treated with DSS. Significance was defined in an unpaired, two-tailed t-test: *$p < 0.05$.

Despite biological variation within individual replicates, the mean TDS was consistently lower in DSS-treated test replicates than in control. Overall, a significant reduction of TDS in test was observed.

3.5 Quantification of immunofluorescence tissue staining

Immunofluorescent staining in mouse renal tissue was performed using α-Sma, Col1 and pSmad2 as target proteins. The percent of area positively stained for the protein of interest was used to quantify the expression of the protein of interest. Comparisons of protein quantification were drawn between UUO and sham kidneys and between control and test tissue.

The images shown exemplarily illustrate the expression of α-Sma in UUO (left) and sham (right) in mouse renal tissue (Figure 23). Visual analysis yielded an increased fraction of area positive for α-Sma in UUO. In the UUO kidney, α-Sma expression was most prominent surrounding the glomerulus as well in the interstitial space between the tubules. Furthermore, it was expressed strongly in the intraglomerular mesangium. In the sham tissue, background staining was seen throughout the image. Overall, no significant α-Sma fluorescence was observed in Sham,

as only a few areas with pronounced fluorescence were evident, i.e. in the bottom right corner (Figure 23: Sham - α-Sma). Regular DAPI staining confirmed good slicing quality.

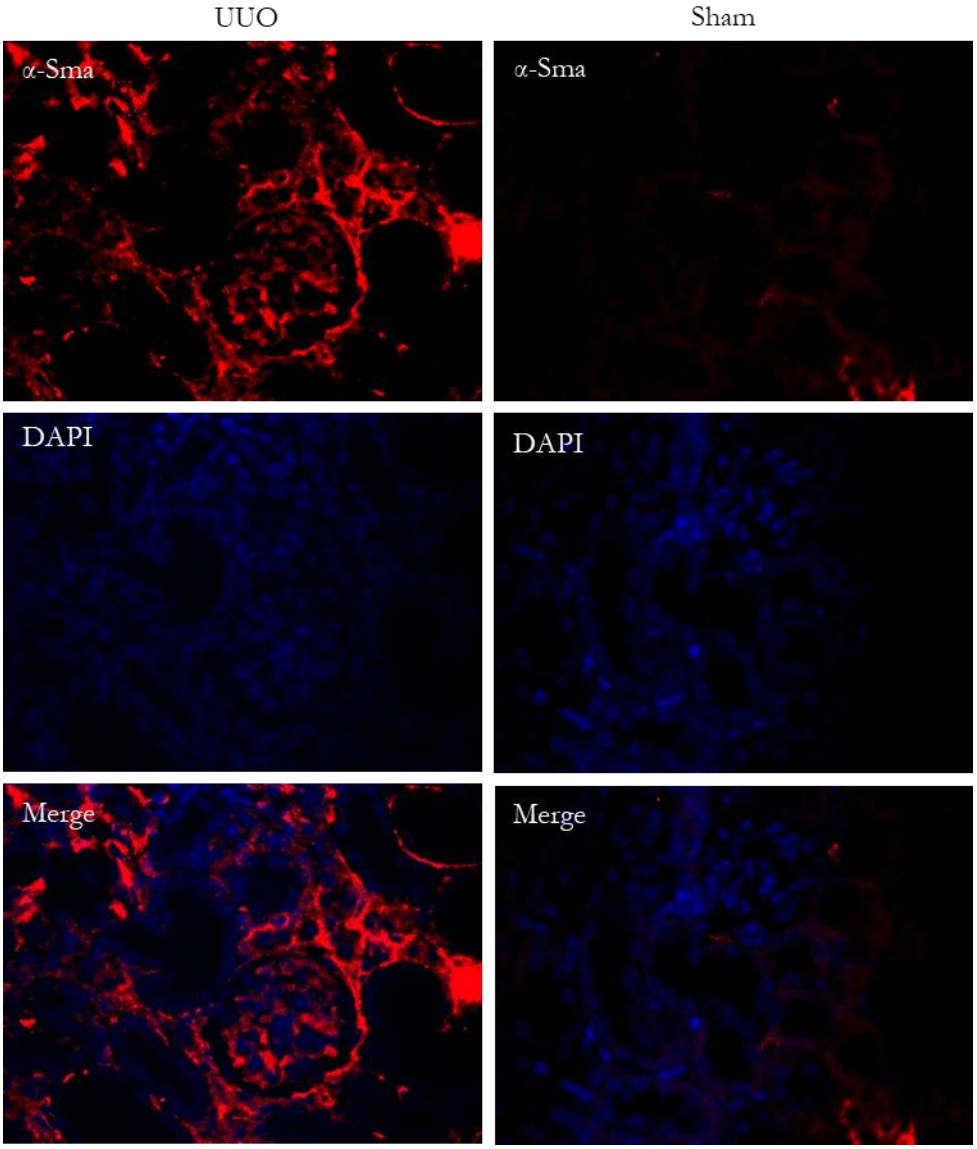

Figure 23: Immunofluorescent tissue staining of α-Sma in mouse kidney. The specimens were treated with antibodies directed at α-Sma and DAPI nuclear staining. The stains are shown individually, red areas positive for α-Sma and blue areas marking the cellular nuclei, and together in a merged image. A significant fluorescence of α-Sma in UUO kidneys was observed, with intense staining surrounding the glomerulus, in the mesangium, and in the interstitial space. It must be noted that the image of the UUO renal tissue depicts an artery that is intensely stained (encircled stained red area at the right of the image), as arterial walls physiologically have a high expression of α-Sma. In comparison to UUO, a stark reduction of α-Sma fluorescence was observed in Sham. In the presented sample, only a small area of interstitial α-Sma was relevantly stained in the bottom right corner. All images are presented at 400 x magnification. Scale bar: 50 μm.

The mean area in percent of individual UUO and sham replicates that was positive for α-Sma fluorescence after staining was determined (Figure 24).

A trend of increased mean α-Sma fluorescence in control replicates than in test replicates was observed (Figure 24A). Test #2 stood as an outlier, as its α-SMA fluorescence was higher than in the lowest control replicate. The α-Sma fluorescence in sham kidneys (Figure 24B), showed a similar trend. All test replicates showed an α-Sma fluorescence under 0.3%. Of the control mice, only Ctrl #1 remained under this margin. The high α-Sma expression in the UUO tissue of Test #2, described above, was not confirmed in its corresponding sham kidney.

In general, the high standard deviation in relation to the low mean fluorescence was evident in the sham kidneys, due to the extremely high variation of α-Sma expression depending on the region in the kidney. While some areas had a percentual α-Sma fluorescence in the range of the UUO tissue, the overall mean remained low.

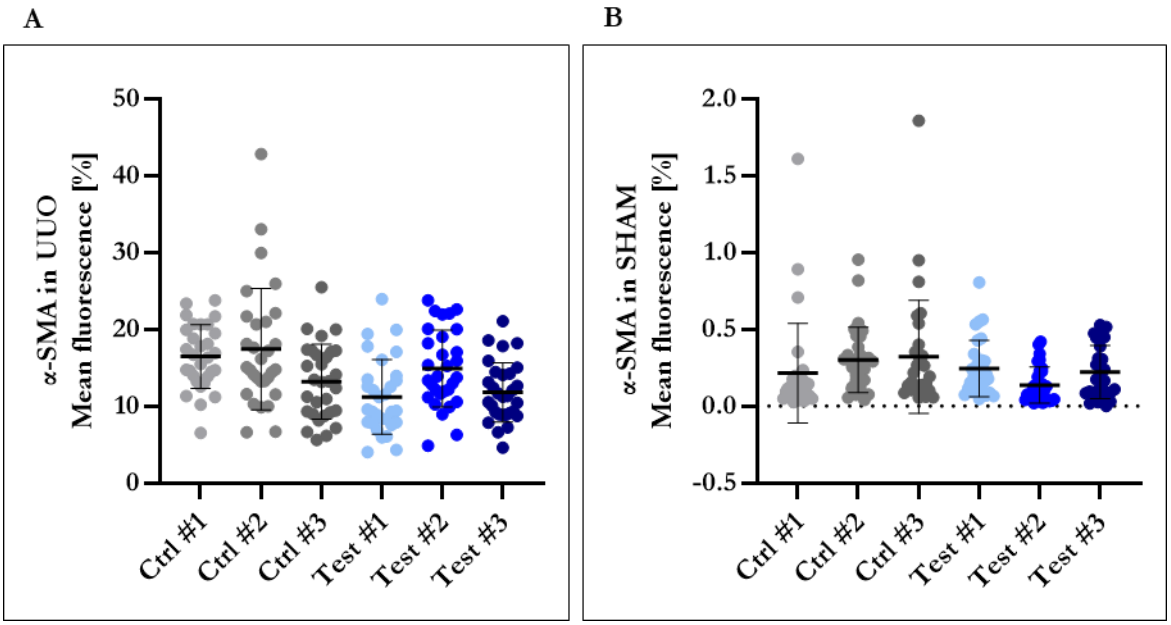

Figure 24: Percent of area positive for α-Sma expression in individual replicates. The figure illustrates mean area positive for α-Sma fluorescence in UUO and sham replicates. The grey-shaded values to the left of each graph present data from control replicates, while the blue-shades to the right present data from DSS-treated test replicates. The x-axis defines these biological replicates in control and test mice. The y-axis marks the area in percent of each image positive for α-Sma as a mean of 30 technical replicates with positive standard deviation. Image A presents the α-Sma fluorescence in UUO. Here, a trend to higher α-Sma fluorescence in control than in test replicates can be observed. A similar trend can be seen in image B, which presents the α-Sma fluorescence in sham. Significance was defined in an unpaired, two-tailed t-test: *$p < 0.05$.

In order to objectify the significance of the differential α-Sma expression in control and test replicates, the biological replicates from each treatment group were combined and analyzed with an unpaired, two-tailed t-test (Figure 25). Within UUO, DSS treatment yielded a highly significant reduction of α-Sma expression ($p < 0.0001$) by approx. 20%. Within sham (Figure 25B),

DSS treatment in the test mice also resulted in a significant decrease of α-Sma expression in comparison to control, though not as prominently as in UUO.

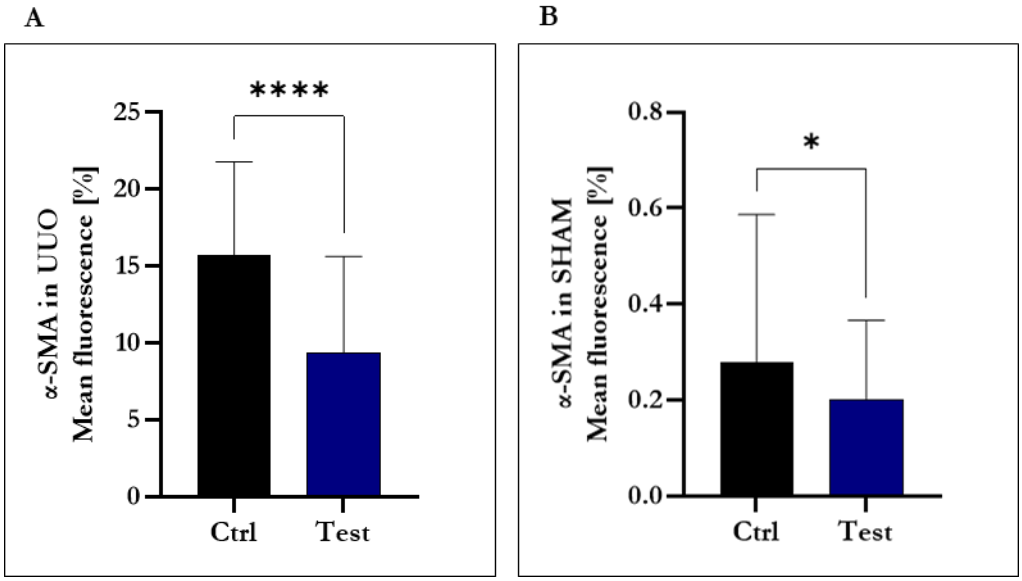

Figure 25: Percent of area positive for α-Sma fluorescence in UUO and sham. The figure compares overall α-Sma fluorescence between control and test. The x-axis defines the treatment group and the y-axis marks the α-Sma fluorescence in percent as a mean of 90 values with positive standard deviation. Image A compares the overall mean α-Sma expressions in control and test in UUO tissue. A highly significant reduction of α-Sma fluorescence in test was observed. Image B presents the same information in the corresponding sham tissue. Here, DSS treatment yielded a similar but less prominently significant reduction of α-Sma fluorescence in comparison to control. Statistical significance of the unpaired, two-tailed t-test was defined as *$p < 0.05$, ***$p < 0.0001$.

Despite biological variation between individual replicates, DSS treatment overall resulted in a significant reduction of α-Sma expression in immunofluorescent stains of both UUO and sham mouse renal tissue.

Further immunofluorescent staining was performed with Col1 as protein of interest, the images (Figure 26) illustrating Col1 immunofluorescent staining of mouse renal tissue exemplarily in a control UUO kidney (left) and the corresponding control sham kidney (right). Col1 was augmented in the UUO kidney in comparison to the sham kidney, recognizable by the increased red fluorescent staining, and was most intense in the basement membrane of the renal tubules and in the interstitial space between tubules. In the sham kidney, Col1 was also expressed along the basement membrane, but much more faintly and more thinly than in the UUO kidney.

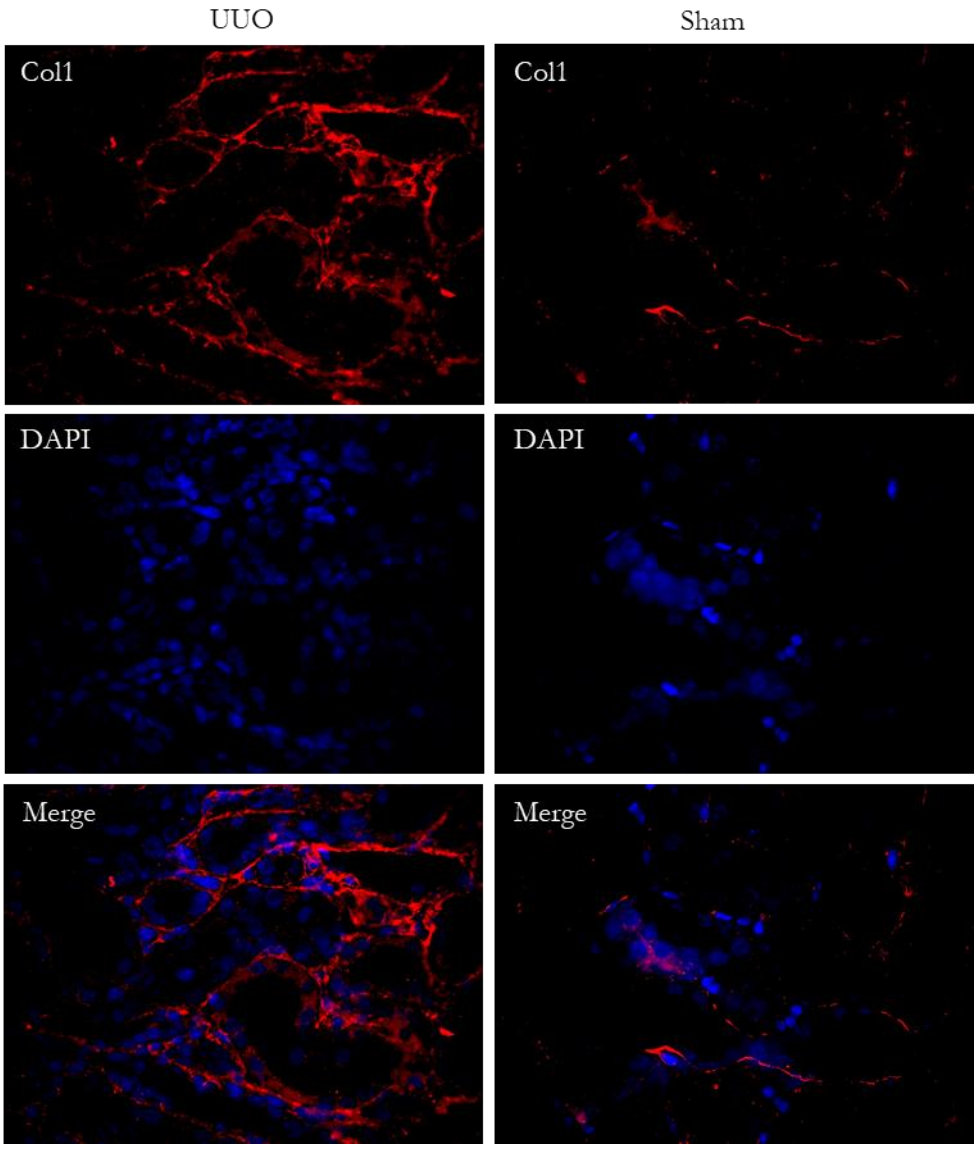

Figure 26: Immunofluorescent tissue staining of Col1 in mouse kidney. The specimens were treated with antibodies directed against Col1 followed with DAPI nuclear staining. The stains are shown individually, red areas positive for Col1 and blue areas marking the cellular nuclei, and together in a merged image. A significant fluorescence of Col1 in UUO tissue was observed, with intense staining in the tubule basement membrane and in the interstitial space. In comparison to UUO, a stark reduction of Col1 fluorescence was seen in sham, with only a small portion of interstitial fluorescence measurable. All images are presented at 400 x magnification. Scale bar: 50 μm.

Col1 expression was quantified in UUO and sham tissue of control and test replicates as a percent of the image area (Figure 27). As in the analysis of α-Sma fluorescence, a general trend to higher Col1 concentrations in control as compared to the test group in UUO tissue was observed. Test #1 remained an exception, exhibiting the highest Col1 expression in both UUO and sham kidneys among all test replicates. A similar pattern was observed in Ctrl #3, which presented the highest Col1 expression in tissue from both UUO and sham in comparison to the other control replicates. Furthermore, an overall higher standard deviation in the sham kidneys than in the UUO kidneys was observed.

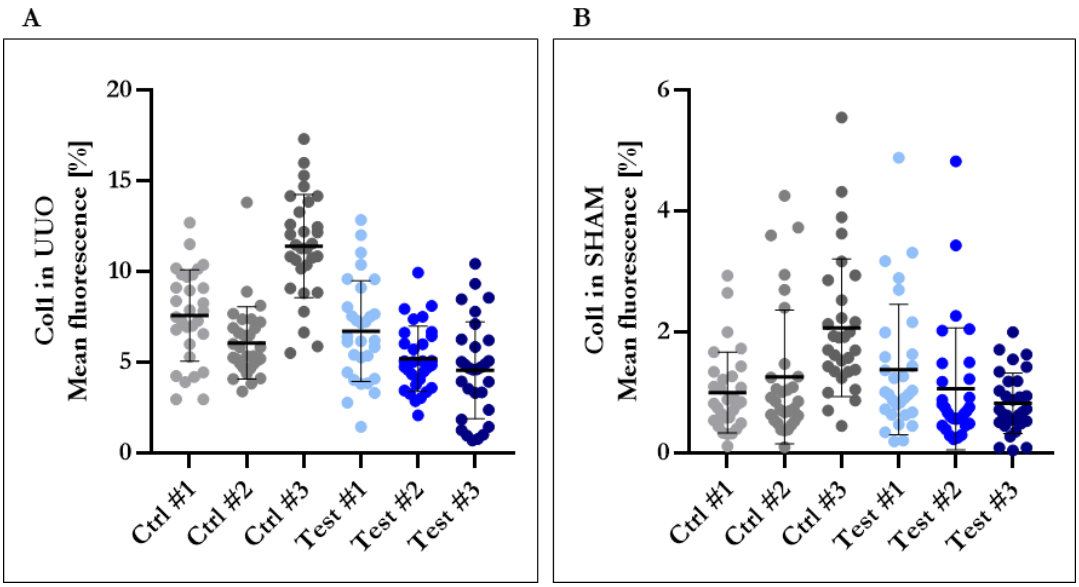

Figure 27: Percent of area positive for Col1 expression UUO and sham mouse kidney tissue. The figure illustrates mean area positive for Col1 fluorescence in UUO and sham replicates. The grey-shaded values to the left of each graph present data from control replicates, the blue-shades to the right present data from DSS-treated test replicates. The x-axis defines these biological replicates in control and test mice. The y-axis marks the area in percent of each image positive for Col1 as a mean of 30 technical replicates with its positive and negative standard deviation. Image A presents the Col1 fluorescence in UUO. Here, a trend to higher Col1 fluorescence in control than in test replicates was observed. In sham kidneys, no clear trend was evident. Significance was defined in an unpaired, two-tailed t-test: *$p < 0.05$.

A direct comparison of overall Col1 expression in control and test was performed (Figure 28). In accordance with the trend seen in individual UUO replicates, a significant reduction of Col1 expression in test was observed. In sham, a less pronounced though nonetheless significant decline was likewise seen.

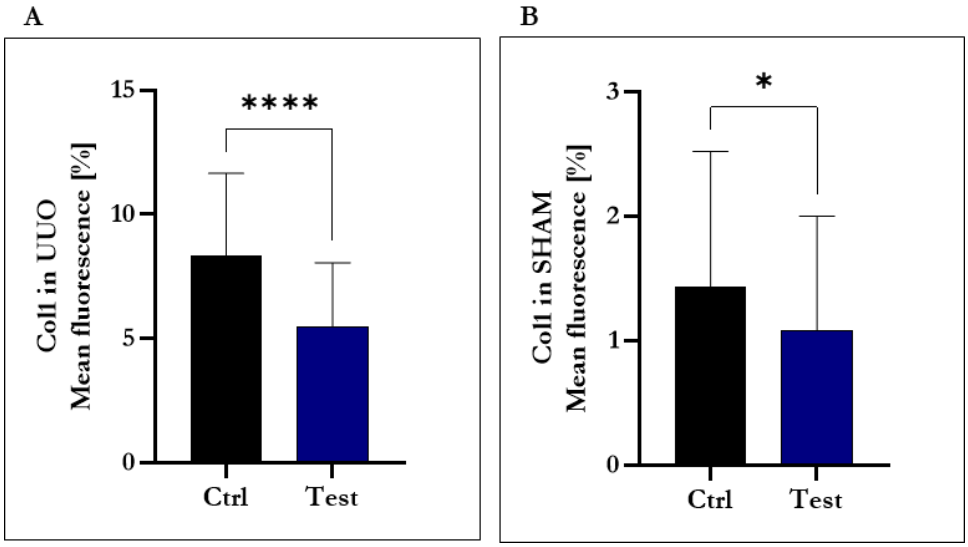

Figure 28: Percent of area positive for Col1 fluorescence in UUO combined treatment groups. The figure compares overall Col1 fluorescence between control and test. The x-axis defines the treatment group and the y-axis marks the Col1 fluorescence in percent as a mean of 90 values with positive standard deviation. Image A compares the overall mean Col1 expressions in control and test in UUO tissue. A highly significant reduction of Col1 fluorescence in test was observed. Image B presents corresponding information in sham tissue. Here, DSS treatment yielded a similar but less prominently significant reduction of Col1 fluorescence in comparison to control. Statistical significance of the unpaired, two-tailed t-test was defined as *$p < 0.05$, ***$p < 0.0001$.

Finally, immunofluorescent staining of pSmad2 was performed on UUO and sham kidney tissue of control and DSS-treated mice (Figure 29). The protein pSmad2 was found in the nucleus, as seen most evidently in the UUO images, where the red stained areas marking pSmad2 corresponded with the blue DAPI-stained markings representing the cell nucleus. The most intense staining appeared in the tubular epithelial cells lining the pathologically dilated kidney tubules. In sham, the expression of pSmad2 was reduced, with only a few red specks recognizable in individual nuclei. The tubules in the sham kidney were not dilated.

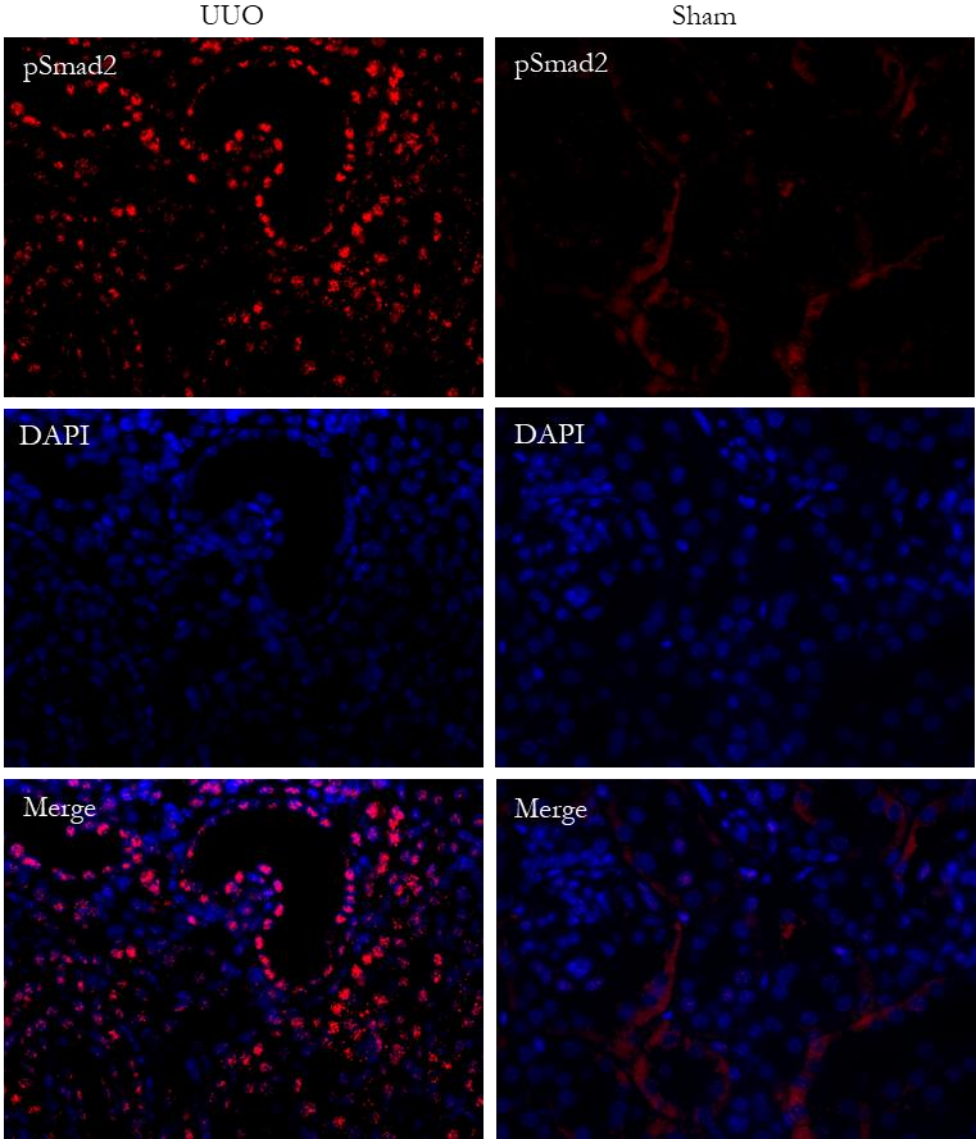

Figure 29: Immunofluorescent tissue staining of pSmad2 in mouse kidney. The specimens were treated with antibodies directed against pSmad2 followed by DAPI nuclear staining. The stains are shown individually, red areas positive for pSmad2 and blue areas marking the cellular nuclei, and together in a merged image. A significant fluorescence of pSmad2 in UUO tissue was observed, with intense staining in the nuclei of tubular epithelial cells. Hardly any pSmad2 fluorescence was recognizable in sham. Aside from the cytoplasmatic background staining, not included in quantification, only individual cells expressed measurable pSmad2 amounts. All images are presented at 400 x magnification. Scale bar: 50 μm.

The mean area positive for pSmad2 expression in percent from different regions of UUO and sham kidney tissue in individual biological replicates was determined. Analysis of UUO kidney tissue revealed a consistently lower pSmad2 expression in all DSS-treated mice than in control (Figure 30A). In sham, no general trend was identified, as test and control replicates presented a wide range of pSmad2 expression (Figure 30B).

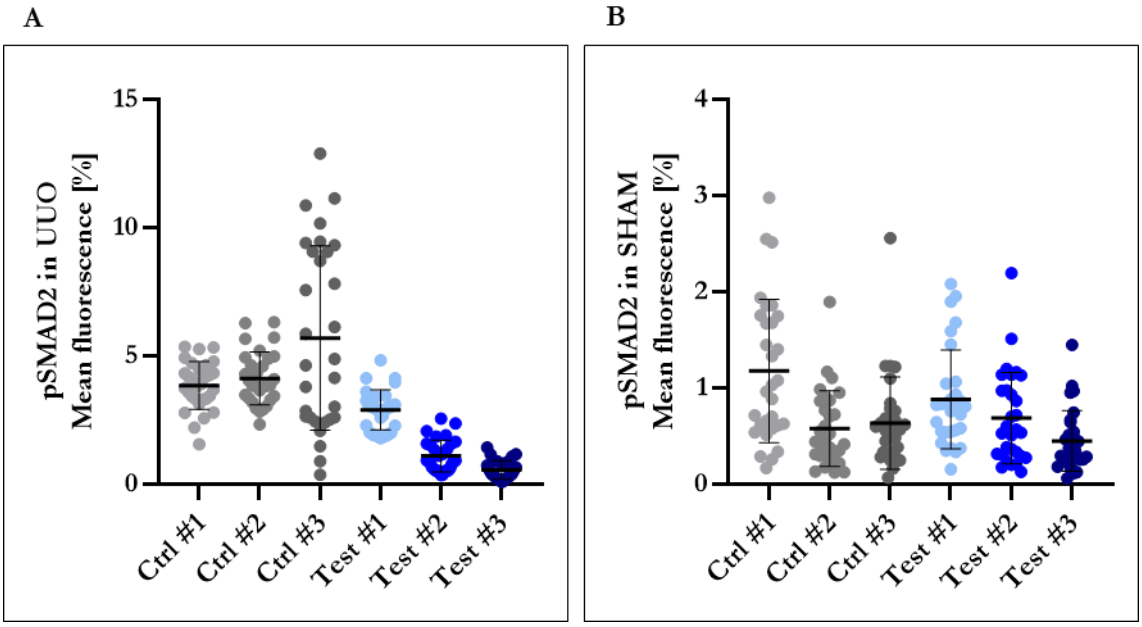

Figure 30: Percent of area positive for pSMAD2 expression in UUO and Sham kidneys. The figure illustrates the mean area positive for pSMAD2 fluorescence in UUO and sham replicates. The grey-shaded values to the left of each graph present data from control replicates, while the blue-shades to the right present data from DSS-treated test replicates. The x-axis defines these biological replicates in control and test mice. The y-axis marks the area in percent of each image positive for pSMAD2 as a mean of 30 technical replicates with its positive standard deviation. Image A presents the pSMAD2 fluorescence in UUO. Here, a trend to higher pSMAD2 fluorescence in control than in test replicates was observed. In sham kidneys, seen in image B, no clear trend was visible. Significance was defined in an unpaired, two-tailed t-test: *$p < 0.05$.

As in the analysis of α-Sma and Col1 fluorescence, overall pSmad2 fluorescence between test and control was analyzed. DSS treatment led to a highly significant reduction of pSmad2 fluorescence in UUO tissue with an approx. 67% reduction in comparison to control (Figure 31A). In sham, while a slight decline of pSmad2 fluorescence of approx. 15% under DSS treatment was likewise measurable, the difference was not assessed as significant (Figure 31B).

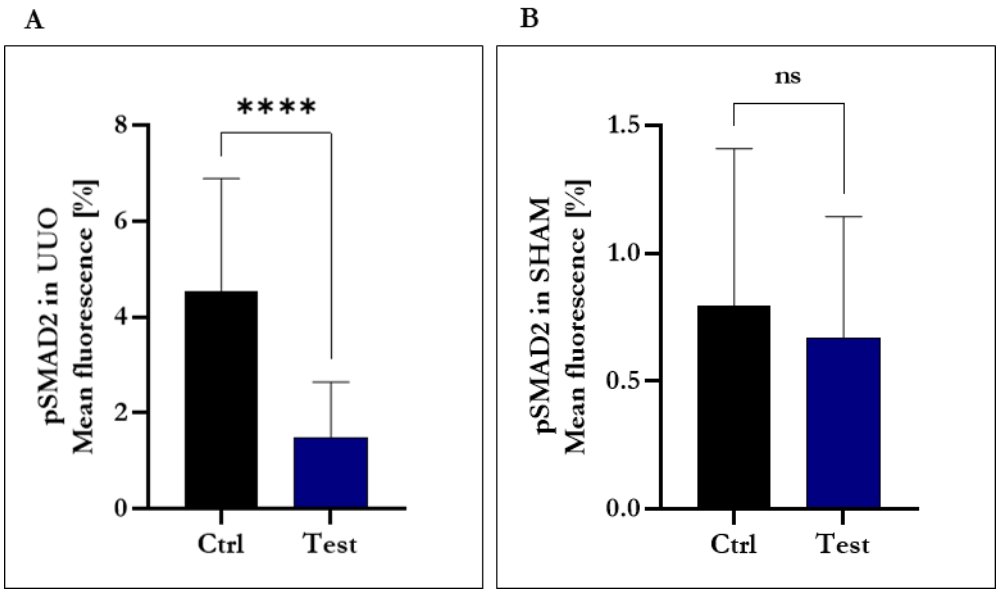

Figure 31: Percent of area positive for pSmad2 fluorescence in combined treatment groups. The figure compares overall pSmad2 fluorescence between control and test. The x-axis defines the treatment group and the y-axis marks the pSmad2 fluorescence in percent as a mean of 90 values with positive standard deviation. Image A compares the overall mean pSmad2 expressions in control and test in UUO tissue. A highly significant reduction of pSmad2 fluorescence in test was observed. Image B corresponding information in sham tissue. Here, DSS treatment did not lead to significant differential pSmad2 fluorescence. Statistical significance of the unpaired, two-tailed t-test was defined as *$p < 0.05$, ****$p < 0.0001$.

The UUO procedure led to a measurable upregulation in pSmad2 expression in both control and test. DSS treatment was able to significantly reduce this upregulation in comparison to control. In sham tissue, no significant alteration in pSmad2 expression between control and test was observed.

In conclusion, immunofluorescent staining revealed a significant reduction of α-Sma, Col1, and pSmad2 under DSS treatment in UUO mouse renal tissue. In sham tissue, significance was only observed in the downregulation of α-Sma and Col1 expression, while pSmad2 showed no significant expression alteration between test and control.

4 Discussion

4.1 Summary of Results

In-vitro and *in-vivo* models were applied to assess the effect of DSS on oxidative stress levels and fibrosis development in renal tissue. In the cell viability assay, DSS treatment had a beneficial effect on cellular metabolism and cell viability of TK173 cells regardless of H_2O_2-induced oxidative stress. FACS quantification of intracellular ROS using a CM-H_2DCFDA marker revealed a significant reduction of ROS concentration in those TK173 cells treated with DSS prior to H_2O_2 exposure suggesting an antioxidative effect of DSS. In Western blot analysis, DSS treatment led to an increase in overall VIM and FN1 expression, while the bulk increase was attributed specifically to VIM IV. Sole exposure to H_2O_2 resulted in a reduction of VIM IV and FN1 expression. SOD1 expression was increased after DSS treatment and increased further in combination with H_2O_2. Finally, PAS and immunofluorescent staining was performed on renal tissue of the UUO mouse model: When considering PAS-stained UUO tissue, a significant reduction of the TDS was observed in DSS-treated test mice. Likewise, quantification of α-Sma, Col1, and pSmad2 in UUO tissue revealed a significant reduction of all proteins of interest in DSS-treated mice kidneys suggesting an anti-fibrotic effect of the treatment. In sham tissue, only α-Sma and Col1 exhibited significant differential expression.

4.2 Validity of Material and Methods

The chosen methods and models reveal different advantages and disadvantages regarding their application in this study.

4.2.1 TK173 cell line as *in-vitro* model of kidney fibroblast responses

The immortalized human kidney fibroblast cell line TK173 is an established *in-vitro* model to perform cell viability assays, FACS analysis, and Western blot (Eltoweissy et al. 2011; Dihazi et al. 2011) and guarantee the reliability of the presented results. Because of the controlled parameter changes, in this case the oxidative stress levels, the results avoid influence through further variables thus confirming their high validation for this parameter. The advantages of using a cell line such as TK173 are its genetic cell modification leading to an infinite lifespan, rapid cell proliferation, and its resilient nature granting simple maintenance (Kaur and Dufour 2012), all allowing the high number of performed experimental replicates. Nonetheless, the genetic modification limits the validity of the results in experiments with TK173 cells in comparison to the results in an *in-vivo* context. The validity could be further compromised due to unknown further

mutations occurring after countless serial passages. Consequences of these intentional and unintentional changes in genetic makeup in cell lines were illustrated in a proteomic comparison of hepatic cell lines and primary liver cells, discovering that the cell line presents a decreased expression of ECM proteins and proteins associated with tissue homeostasis, as well as an increased expression of proteins involved in the TGF-β pathway (Pan et al. 2009). Thus, primary cells would have provided a more realistic evaluation of the effects on renal fibroblasts by eliminating the questionable factor of genetic veracity. However, their delicate nature with decreased passaging options would have limited the reliability of the results due to reduced experimental replicates. Furthermore, primary cells are much more susceptible to environmental changes, so that unexpected changes in stress levels through exogenous factors would have affected the comparability of the performed experiments. A study between primary renal cells and the TK173 renal cell line would be necessary to understand the proteomic limitations of the *in-vitro* model and objectify the extent to which the results can be applied *in-vivo*. Nonetheless, both *in-vitro* cell models lack the complex exogenous and endogenous factors of fibrosis development in a living organism and thus require an *in-vivo* model to evaluate the impact of DSS on renal fibrosis and of its therapeutic effect in the human organism.

4.2.2 UUO in mice as model of renal fibrosis

In-vivo models have a high external validity, as studies can be performed with intact tissue in mammalian model organisms, thereby most closely nearing human conditions (Nogueira et al. 2017; Yang et al. 2010). The application of DSS in living organisms shows its genuine effect within complex regulatory mechanisms of fibrosis development including undiscovered pathways, and it provides data regarding possible side effects of DSS relevant for its clinical use. A transfer of the results to renal fibrosis in humans is likely as the fibrosis induction seen in UUO is applicable in various species including the rabbit, in which it was originally developed (Chevalier 2006), and the mouse, used in this study. Additionally, the UUO model is especially relevant in regards to children, as urinary obstruction is one of the main causes of CKD in this age group (Seikaly et al. 2003). Furthermore, the key pathophysiological processes occurring in human renal fibrosis and CKD, including macrophage infiltration, fibroblast proliferation, EMT, and an increase of the ECM, are mirrored in the specific UUO models (Chevalier et al. 2009). Despite these similarities, UUO is an abrupt event with immediate implications for kidney function, objectified by measurement of renal blood flow, which is reduced within 24 h post-surgery (Vaughan et al. 2004). Within seven days, tubular dilation and atrophy as well as tubulointerstitial fibrosis becomes manifest (Yang et al. 2010), differing morphologically from other etiologies and pathogeneses of CKD for example through glomerulonephritis. This

pathophysiology differs considerably from the average development of CKD in humans, which can occur over a timespan of decades, permitting certain adaptive mechanisms in renal tissue to transpire. Therefore, the molecular changes observed in the UUO model can only partially be translated onto and compared with *in-vivo* human kidney fibrosis. An option to improve the validity of the UUO model would be a partial ureteral ligation, as *in-vivo*, a partial obstruction is much more common than a complete obstruction (Chevalier 2006). Nonetheless, the persisting benefit of the complete UUO model is precisely the abovementioned speed of fibrosis development, which is higher than in other CKD models, thereby aiding the execution of experimental replicates. Models of diabetic nephropathy, for example, often require genetic modifications, take weeks to develop nephropathy, and present systemic side effects, which themselves could affect fibrosis development (Betz and Conway 2016).

Of all organisms in which UUO has been established, use of the mouse has the advantage of decades of research experience, allowing a more precise determination of dosage in treatment application, as well as more specific and animal-friendly keeping (Fox et al. 2007). Rapid reproduction time and adequate operability of mice present further benefits of this model organism. As a placental mammal, mice have a close evolutionary relationship with humans, validated by genomic studies showing prominent similarities between mice and humans, with extensive parallels in protein expression (Perlman 2016). However, differences in monitoring networks and transcription regulation have also been observed, which could alter the reaction of the organism within clinical experiments (Rydell-Törmänen and Johnson 2019). An additional relevant metabolic difference is the naturally increased synthesis of ROS in mice in comparison to humans, due partly to the increased amount of readily oxidizable fatty acids in mice and the increased basal metabolic rate in relation to body mass (Perlman 2016). Thus, the influence of ROS leading to fibrosis in this mouse model could be greater than in humans.

Regarding this study, this background information calls for a careful interpretation and translation of results to the human organism. Overall, UUO remains an important model of renal fibrosis, and an understanding of its limitations allows a well-founded classification of the compiled data.

4.2.3 MTT cell viability assay

In this study, the MTT cell viability assay was applied to assess changes in metabolic activity in human kidney fibroblast cell line TK173 subjected to varying concentrations of DSS and H_2O_2. The assay relies on the principle that changes in extinction are due to an increase of NADPH-dependent enzymes based on an increase in the absolute amount of cells (van Meerloo et al.

2011) allowing conclusions to be drawn about the rate of cell replication and thereby about the metabolic activity and viability of the cells.

Two benefits of this assay, making it gold standard to this day, are its high statistical sensitivity and the opportunity for a great number of experimental replicates (van Tonder et al. 2015). The low number of cells seeded per well also contributes to its high sensitivity, as cellular stress through proliferation and consequent overpopulation in each well would have negatively influenced the viability, independent of oxidative stress as the primary parameter of interest. Finally, the use of a cell line further minimizes chances of external cellular stress as the high cell tolerance of TK173 cells for environmental fluctuations eliminates extraneous parameters which, likewise, could affect cellular replication and metabolism (see section 4.2.1). It is furthermore shown that the addition of DSS to cell culture DMEM has no influence on the extinction of the solution, thereby maintaining the direct correlation between extinction and metabolic activity (Figure 11).

On the other hand, limitations have been recognized in the methodology of the MTT assay which could lead to inexact results or limit the assay's relevance. While the high number of individual pipetting steps and inadequate handling of the light-sensitive MTT solution can lead to an accumulation of human err causing inaccurate results (van Meerloo et al. 2011), the MTT assay is a highly established method in the laboratory and has been performed on TK173 cells, thereby reducing the probability of error where possible (Eltoweissy et al. 2011). Additionally, the reliability of the MTT assay in certain experimental setups can be questioned, as van Tonder et al. (2015) showed that the MTT assay is less exact than other cell enumeration assays, such as the sulforhodamine B assay, when a low number of cells (<1000/well) is being analyzed. However, in this study, 5000 cells/well were initially seeded, thus avoiding possible imprecision due to low cell numbers. A further known limitation of the MTT assay is its predisposition for interference through glycolysis inhibitors because the assay relies on the presence of glucose and functioning glycolysis in the mitochondria as a source of NADH (van Tonder et al. 2015). This too is avoided in this study, as the substances tested, DSS and H_2O_2, do not belong to the family of direct glycolysis inhibitors so that no interference through external factors is expected, and all cells were treated with the same cell culture DMEM and were therefore adequately supplied with glucose for regular metabolic cell activity to occur. A final disadvantage of the MTT cell viability assay worth mentioning is the characterization of its measurement as an "endpoint-determination", because the release of the intracellular formazan crystals needed for photometric measurement relies on lysis of the cells and is therefore not suitable for continuous monitoring of cell and metabolic development (Präbst et al. 2017). While this characteristic is unavoidable, it is taken into account through the analogous application of the defined endpoint to

Western blot and FACS analysis in which TK173 cells were also used, thereby standardizing all timeframes. Furthermore, the lack of long-term analysis in the MTT cell viability assay is ameliorated through the subsequent, longer-term DSS treatment *in-vivo*.

4.2.4 CM-H_2DCFDA as a marker of ROS with FACS analysis

The effect of oxidative stress on cells can be objectified directly through quantification of intracellular ROS by fluorescent ROS staining and fluorescence quantification, thereby differing from indirect quantification through detection of changes in gene expression and protein synthesis. FACS was chosen as the method for direct fluorescence quantification due to its speed, specificity, and high statistical value owing to the high number of analyzed cells (Ameziane-El-Hassani and Dupuy 2013). Fluorescence microscopy presents another option to detect intracellular ROS, regardless of the chosen marker. This method would have allowed the direct observation of cell processes with exact localization of ROS within each cell, however, the disadvantages in this case outweigh the benefits, as it is a relatively slow method and requires an additional image processing step to complete the fluorescence quantification (Marjanovič et al. 2014). Furthermore, the exact cellular localization of ROS is irrelevant to answer the research objectives in this study, as focus is placed on the total amount of oxidative stress regardless of its cellular origin.

A fluorescent probe for direct staining of ROS must satisfy certain criteria to qualify for a valid analysis: it must be stable, possess the ability to permeate across the cell membrane, distribute itself within the cell, and not interact or affect the natural metabolism of the cell, and CM-H_2DCFDA, the marker used in this study and quantified using FACS analysis, fulfills these criteria (Chen et al. 2010). The straightforward application of CM-H_2DCFDA minimizes pitfalls and makes it a regularly used method across scientific fields (Kalyanaraman et al. 2012). Its oxidation to its fluorescent form DCF occurs through the interaction with H_2O_2 and other ROS such as hydroxyl radicals or peroxy nitrate therefore allowing a quantification of various oxidative processes (Ameziane-El-Hassani and Dupuy 2013). Amplex Red reagent is another substrate that is metabolized through ROS and can alternatively be used as a marker to quantify ROS concentration using FACS analysis, but in comparison to CM-H_2DCFDA, Amplex Red is only metabolized and converted to its fluorescent form in the presence of H_2O_2, and not by other ROS (Kalyanaraman et al. 2012). While the experimental setup applied in this study used H_2O_2 as stressor and would therefore have been more specifically registered with Amplex Red, the experiment was designed to answer the question whether DSS is able to rescue cells from all types of oxidative stress, regardless of their chemical formation. Therefore, also ROS

occurring independently of the externally applied H_2O_2 are relevant, making CM-H_2DCFDA an appropriate marker in this case.

4.2.5 Western blot

Western blotting allows the specific quantification of even minute protein amounts and enables the differentiation of individual proteins according to size within the SDS gel (Ghosh et al. 2014). This characteristic is especially valuable in this study, as the molecular weight of the proteins of interest range immensely, from SOD1 as the smallest protein with approx. 35 kDa (Tsang et al. 2014) to FN1 with 250 kDa (Potts and Campbell 1996). Furthermore, the direct correlation of the detected band to its approximate molecular weight using the electrophoresis reference marker provides additional proof of successful antibody binding. Fluorescence microscopy, in comparison, lacks this proof of specific antibody binding, as a differentiation from unspecific antibody binding can only be deduced through the appropriate protein localization within the tissue.

Despite its status as a standard experimental procedure, the Western blot method has certain disadvantages that must be considered, such as its complex design with many individual steps over several days, allowing an accumulation of errors to occur (Ghosh et al. 2014). An increase in replicates can minimize these errors (Wu et al. 2014), supporting the decision to assess three replicates in this study, thereby increasing the sensitivity and validity of the results. Additionally, the standardized use of a housekeeper protein in addition to an exact protein quantification in the sample prior to electrophoresis enhance comparability of the different test groups. However, the required use of antibodies for protein detection on the membrane offers further pitfalls including the failure to recognize post-translational modifications of the proteins, such as phosphorylation, which change the configuration of the protein, hinder antibody-antigen binding, and cause a false-negative result to ensue (Bass et al. 2017). In this study, phosphorylated proteins were only chosen as proteins of interest in immunohistochemistry and reflected as such in the choice of antibody. Real-time polymerase chain reaction (rt-PCR) is a further method supplementing Western blot that would increase validity of the results and reduce error margins occurring in the processes between gene transcription and the protein expression, as assessed with Western blot. In this case, translation and post-translational modifications are not detected, so that Western blot remains a valuable tool in this study.

4.2.6 Histological analysis

Histochemistry is an established method to perform *in-vivo* research and to analyze tissue in its natural state. In this study, PAS and immunofluorescent tissue staining were performed to gain

insight to structural changes within the mouse kidney and as a further proteomic method to quantify protein expression, respectively. While both methods require knowledge of the procedure, awareness of the possibility of error and, in the case of immunofluorescent staining, a validation of the antibodies, both methods were well established in the laboratory so that a well-proven protocol could be followed (Fitzgibbons et al. 2017).

The benefits of histochemistry include its visual control of experimental success. This can be shown graphically when considering immunohistochemistry, which allows focus on specific protein changes (Amann and Haas 2006). pSMAD2, for example, is physiologically expected to be found in the cellular nucleus, and fluorescence located outside of the nucleus after staining would therefore have been an immediate indication of error. Furthermore, the biological variance of protein expression in different renal tissues and regions can be objectified with histology. While rt-PCR, for example, assesses gene expression as a mean of the entire tissue sample, microscopical evaluation of the specimen provides an overview of fluctuations in protein expression, for example between the cortex and the medulla of the kidney. This applies likewise to PAS tissue staining and the TDS used to evaluate the tissue: analysis underlined the high spectrum of damage within each UUO kidney, with some areas presenting little to no damage and others displaying pronounced tubular dilation (Figure 21).

While the PAS stain, through its strong staining of glomerular and tubular basement membranes and its detection of vascular abnormalities (Amann and Haas 2006), is an appropriate staining method allowing the determination of a TDS, certain weaknesses of the scoring method are evident. Firstly, the TDS is primarily a qualitative analysis with only semi-quantitative consideration of the number of damaged tubules, thus limiting its objectivity. Furthermore, due to its narrow physiological structure and the natural limitations of light microscopy, analysis of the basement membrane is more difficult than analysis of the measurable tubule dilation, so that this parameter is not as equally incorporated into determination of the TDS. Despite these limitations, quantitative analysis of protein expression in the mouse renal tissue supplemented the TDS, improving the analysis quality of the *in-vivo* experiments.

4.3 Effect of DSS on *in-vitro* TK173 fibroblast cell line under oxidative stress conditions

4.3.1 Antioxidant effect of DSS on cell viability and oxidative stress pathways

Fundamental research supports the presented data demonstrating the antioxidant effect of DSS through its improvement of cell viability and reduction of ROS concentration, and furthermore

provides insight to the underlying pathways leading to differential expression of the antioxidant protein SOD1.

The negative effect of oxidative stress on cells, which is known to play a relevant role in cell senescence, carcinogenesis, atherosclerosis, and fibrotic diseases (Parascandolo and Laukkanen 2019), was markedly proven through the MTT cell viability assay performed in this study, in which a stark reduction of TK173 cell viability was caused by increasing H_2O_2 concentration (Figure 13A), confirming the results from Eltoweissy et al. (2011). In contrast, increasing DSS concentrations led to a corresponding linear increase of cell viability and metabolism in TK173 cells, agreeing with HU et al. (2016), who examines the effect of DSS on myocardial ischemia reperfusion injury, and describes a similar, linearly increasing effect in the viability of cardiomyocytes in the cell viability assay. The question remains whether a cytotoxic concentration of DSS on TK173 cells exists as no plateau in the extinction curve was seen so far, so that currently, no negative effects have been determined on cell viability and proliferation. The related Salvia miltiorrhizae extract salvianolic acid B, for example, appears to have a cytotoxic effect on an *in-vitro* tubule epithelial cell line determined by alamarBlue assay at high concentrations (Wang et al. 2010). Nonetheless, the results at the applied concentrations appear coherent, and researchers have come to focus on the antioxidant influence of DSS as explanation for its beneficial effect on cells. This is confirmed by the performed cell viability assay with DSS pre-treatment followed by varying concentrations of stress with H_2O_2, in which DSS rescues TK173 cells from oxidative stress at lower H_2O_2 concentrations, significantly increasing the cell viability. A similar positive effect is seen at higher H_2O_2 concentrations, though not as pronounced. One related study assesses the radical scavenging activity of DSS in endothelial cells, performing a slightly modified cell viability assay with variance of the concentration of DSS pre-treatment over a 4 h period while maintaining a constant concentration of H_2O_2, and despite the different experimental design, cell viability in H_2O_2-exposed cells increases under DSS treatment (Zhao et al. 2008). This study, therefore, contributes to evidence confirming the antioxidant activity of DSS and enlarging its spectrum to fibroblasts as shown in this *in-vitro* model.

FACS analysis of DCF fluorescence supports the results of the cell viability assay by showing an increased concentration of ROS after stress with H_2O_2 and by confirming the proposed antioxidant effect of DSS through an objective, significant reduction of intracellular ROS concentration in DSS-treated and H_2O_2-stressed TK173 cells. When comparing unstressed control cells to unstressed cells treated with DSS, on the other hand, no significant reduction of ROS was achieved. In comparison with the results of the cell viability assay, these results therefore raise the question of why and how DSS improves cell viability if ROS concentration remains

unaffected in unstressed cells. A possible answer lies in the consideration of DSS's antioxidative mechanisms. While DSS has an objectifiable antioxidant effect against the oxidative potency of H_2O_2, studies have also shown that the oxygen-free radical scavenging trait of DSS, attributed to its phenol group, plays a much larger role in its protective effect on cell injury, and this trait is not reflected in the DCF fluorescent quantification of ROS, as free radicals are not stained by DCF (Li et al. 2016; Zhao et al. 2008). It can therefore be assumed that a protective antioxidant effect still takes place in unstressed cells regardless of the detection of ROS in this experimental setup. Aside from the direct scavenging antioxidant effect, DSS has a further indirect effect through influence on oxidative stress pathways and subsequent shifting of the expression of antioxidant proteins.

In Western blot, treatment of TK173 cells with DSS leads to a measurable, while non-significant, upregulation of SOD1 expression, suiting its antioxidant function. This upregulation is maintained under treatment with the oxidative stressor H_2O_2, accordant with its feedback regulation of SOD1 (Dell'Orco et al. 2016), and increased further in the combination of DSS and H_2O_2 treatment. Lu et al. (2014) confirm this effect of DSS in an *in-vitro* model of cardiac fibroblasts stressed with pro-fibrotic and oxidative stress stimulant isoproterenol, hereby observing an identical non-significant increase in SOD1 expression, just as H_2O_2 and DSS in the present study, while a combined treatment showed a further upregulation. Furthermore, the same study examines intracellular ROS concentration using dihydroethidium incubation and quantification with inverted light microscopy, and consistent with the presented FACS analysis of DCF fluorescence, DSS reduces the isoproterenol-induced increase in ROS concentration (Lu et al. 2014). The described effect of DSS can be expanded to other pathologies as well. One study examining kidney damage due to iron overload as a model of the complications from β-thalassemia likewise reports a recovery of the SOD concentration in renal tissue after DSS treatment (Guan et al. 2013). Combined, these studies show a wide range of applications in which DSS has a beneficial effect on the SOD1 expression, thereby reducing oxidative stress and improving kidney function. From these results, the exact mechanism leading to an increase in SOD1 expression through DSS stays unclear. Three prominent explanations for the increased expression of SOD1 are the NF-κB, p38-MAPK pathways, which are also prevalent fibrosis pathways (Figure 4), and the transcription factor Nrf2: (1)NF-κB is one of the primary transcriptional factors regulating the expression of SOD proteins, however, it also has a potent influence on the transcription of proinflammatory cytokines and promotes the recruitment of leukocytes (Miao and St Clair 2009; Ruiz et al. 2013). Regarding various reports, it appears that DSS executes its effect on NF-κB primarily through inhibition, leading on one hand to a downregulation of SOD1

expression, but on the other hand also to repression of inflammatory processes, maintaining its beneficial effect on fibrosis development (Xu et al. 2016; Wang et al. 2012). Therefore, DSS does not appear to regulate SOD1 expression through means of NF-κB. (2) The same contradiction applies to the p38-MAPK pathway. The stimulation of the p38-MAPK pathway is highly complex, leading, for example, to either apoptosis or cell survival depending on the duration and strength of the activating signal and depending on the p38 isoform involved (Kyriakis and Avruch 2012). Using mouse embryonic fibroblasts, one study reported signaling through the p38α-MAPK pathway to be responsible for the low-dose H_2O_2-induced increase of SOD1, SOD2 and catalase expression in Western blot, and that a knockout of p38α led to a depletion of these enzymes and a decrease in cell viability through the increased vulnerability for oxidative stress (Gutiérrez-Uzquiza et al. 2012). On one hand, this study confirms the presented data that treatment with H_2O_2 leads to an increased SOD1 expression in Western blot; however, DSS does not appear to carry out its upregulation of SOD1 by means of the p38-MAPK pathway, as various studies show that DSS prevents fibrotic development through inhibition of this pathway (Gao et al. 2016; Lu et al. 2014). (3) Extensive research has therefore identified the transcription factor nuclear factor-erythroid-2-related factor 2 (Nrf2) as the most likely candidate explaining DSS's influence on the upregulation of antioxidant proteins. Nrf2 plays a central role in the coordination of cellular antioxidant responses, regulating the expression of over 250 antioxidant genes, including the SOD enzymes (Ruiz et al. 2013; Jaramillo and Zhang 2013). The presence of ROS in the cytoplasm leads to the liberation of Nrf2 from repressor proteins (Keap1 and Keap2) normally facilitating ubiquitination, allowing Nrf2 to enter the nucleus and execute its effect as transcription factor (Ruiz et al. 2013). Regarding inflammation as a contributing pathogenetic factor in CKD, Nrf2 has been shown to be reduced in *in-vivo* mouse studies with a kidney failure model using five-sixths nephrectomy, thereby proposing a lack of Nrf2 upregulation to contribute to kidney failure, and correspondingly, mouse kidney tissue after Nrf2 knockout presented increased tissue inflammation causing CKD (Ruiz et al. 2013). Various cardiologic studies have demonstrated a positive effect of DSS on Nrf2 concentration, thereby decreasing inflammation and improving tissue recovery, for example, in isoproterenol-induced myocardial infarction in rats, a combination of DSS with paeonol led to a decrease in Keap1 and a subsequent increase in Nrf2 concentrations (Li et al. 2016). A further study confirmed these results in analysis of ischemia-reperfusion injury in rat hearts (HU et al. 2016). Nonetheless, research regarding the relationship between DSS and Nrf2 in kidneys remains scarce, as primary focus thus far has been on the renal effects of salvianolic acid B (Xiao et al. 2020; Pang et al. 2020). In regards to the results in this study, it remains to distinguish the mechanism of SOD1 upregulation seen in both the DSS and H_2O_2 treatment groups in Western blot, thereby

attributing the H_2O_2-induced effect to the p38-MAPK pathway, as presented by Gutiérrez-Uzquiza et al. (2012), while the DSS effect is most likely attributed to the transcription factor Nrf2 (Dell'Orco et al. 2016). Ultimately, to confirm the interaction of DSS with these pathways in TK173 cells, further Western blot or rt-PCR experiments should be performed.

4.3.2 Effect of DSS and H_2O_2 on the expression of fibrosis markers VIM and FN1

VIM and FN1 were the two fibrosis-related proteins examined in the *in-vitro* model to evaluate the effect of DSS and H_2O_2 on protein expression in the TK173 renal cell line.

VIM, an intermediate filament found in mesenchymal cells, shows an increased expression in different forms of organ fibrosis but it is also specifically relevant for the process of EMT in kidneys, as Wang et al. (2018) show in a murine UUO model that VIM knockout in mice leads to a decrease of Col1 expression, suggesting an arrest of fibrosis development in the absence of VIM, i.e. reflecting a crucial role of VIM in fibrosis progression (Wang et al. 2018). In the model presented, this pro-fibrotic effect is seen in the upregulation of VIM III expression as a response to H_2O_2 exposure. Beyond its role in fibrosis development, research has expanded knowledge about VIM function, providing an understanding about its beneficial contribution to cell signaling and communication, regulation of wound healing, and cell resistance and apoptosis (Eriksson et al. 2009). These benefits providing a better resistance against fibrosis, seen exemplarily in cytoskeleton alterations in intermediate filaments such as VIM as a reaction to cellular stress (Welch et al. 1985), may in some cases be lost. Especially VIM IV plays an important role in renal cell resistance: a VIM IV downregulation leads to a decrease in cell viability and a rise in cell apoptosis (Buchmaier et al. 2013), so that oxidative stress caused by H_2O_2 as a fibrosis inductor may also lead to a downregulation, possibly explaining the results in this study. As a reaction to DSS treatment, the studied VIM forms are upregulated, suiting, in the case of VIM IV, its protective effect on renal cells as an antioxidant, whereas in the case of VIM III, the discussion about positive and negative effects of continues. Furthermore, the addition of DSS causes a recovery of the VIM IV expression significantly downregulated by H_2O_2, thus signifying an improvement of cell resistance and protection. The results so far show a positive effect of DSS on TK173 cells, so that the upregulation of VIM expression under its influence can be deemed protective.

TK173 cells consistently react with a decrease in FN1 expression in Western blot after exposure to H_2O_2-induced oxidative stress although an increase in FN1 expression would be expected due to the ROS-mediated activation of the TGF-β pathway (Podkowińska and Formanowicz 2020). However, this *in-vitro* model and experimental setup reflects early stages of an oxidative

stress-induced upregulation of fibrotic proteins, whereas most published studies focus on long-term process fibrosis progression. Thus, the short-term experimental setup reveals only initial effects of H_2O_2 because of its short half-life, so that this one-time application and analysis after 48 h primarily may not reflect the long-term influence of the ROS representative H_2O_2 on protein synthesis, thus contributing to an explanation of the presented results. While the result may indicate that these cells have efficient mechanisms to prevent fibrosis, the applied H_2O_2 concentration of 100 µM, chosen on the basis of the cell viability assay as an appropriate stress level, can be discussed since the determined concentration to treat human fibroblast cell lines plays a prominent role in the observed change of FN1 synthesis: lower concentrations lead to cell senescence and initially to an increase in FN1 synthesis, while higher concentrations cause apoptosis and a decrease in FN1 synthesis (Bladier et al. 1997). Additionally, a high range of and unreliable tolerance for H_2O_2 depending on the cell line must be considered: While Bladier et al. (1997) saw a high degree of apoptosis in the fibroblasts beginning at a concentration of 200 µM H_2O_2, Eltoweissy et al. (2011) still registered a 75% viability of the tested fibroblast cell line in the MTT assay at that concentration, thus demonstrating the varying reactions of different fibroblast lines. In this study, 100 µM H_2O_2 in the cell viability assay already led to a markable reduction of cell viability, so a beginning apoptosis of TK173 cells in this experimental setup could be a possible explanation for the decrease in fibronectin concentration. The non-significant increase in FN1 expression after DSS treatment contradicts most reports in which FN1 was reduced in, for example, models of diabetic nephropathy, although in these studies, a combined Salvia miltiorrhizae treatment with all its extracts was examined thus limiting a direct comparison (Nie and Li 2018; Xu et al. 2016). Nevertheless, one study presents equivalent data to that shown here: in an *in-vivo* mouse model of CKD applying five-sixth nephrectomy, FN1 was increased in Western blot after DSS treatment, although all clinical markers showed improved kidney function and histological indicators revealed a reduction of kidney damage in comparison to control (Guan et al. 2015). It therefore can be argued that FN1 is not necessarily a valid marker to assess overall clinical improvement despite its role as an ECM protein, and therefore, that the FN1 upregulation in TK173 cells under DSS treatment may not reflect the true health of the cells. The cytoprotective effect of DSS is seen again in the combined Western blot setup, as the stark reduction of FN1 concentration in TK173 cells after H_2O_2 exposure slightly increases again when adding the DSS pre-treatment. Based on the theory that the applied concentration of H_2O_2 leads to apoptosis in the cells, justifying the downregulation of FN1 in Western blot, DSS therefore improves cell viability and rescues the cells from apoptosis.

4.4 Effect of DSS on the TGF-β pathway and on *in-vivo* synthesis of ECM proteins

Immunohistochemical staining in mouse renal tissue of α-Sma and Col1, both relevant interstitial proteins in the pathogenesis of organ fibrosis, and pSmad2, as a central player in TGF-β signaling, reveals differential protein expression based on fibrosis induction through UUO and DSS treatment. α-SMA is a key protein marking the occurrence of EMT in fibroblasts, and Col1 is an abundant ECM protein upregulated in fibrotic tissue and also synthesized by myofibroblasts after undergoing EMT (Liu 2011). In the applied *in-vivo* UUO mouse model, both proteins were significantly down-regulated under DSS treatment, thus suggesting a prevention of fibrosis progression. This degree of fibrosis correlates directly with the TDS evaluated using PAS tissue staining, in which the mice treated with DSS maintain a higher proportion of healthy kidney tissue (TDS = 0 or 1) in comparison to the control mice, allowing the conclusion that DSS treatment has a protective effect on kidney tissue in the UUO mouse model. Interestingly, the sham kidney also presents a significant reduction of these fibrotic proteins, although the fibrotic stimulus through UUO is not present. The validation of these results remains difficult as most published studies quantify Col1 and α-SMA in other tissue than the kidney, thus hindering a direct comparison: The degree of Col1 and α-SMA accumulation in carbon tetrachloride-induced hepatic fibrosis, for example, was significantly attenuated under DSS treatment, correlating with improvement of liver function and a reduction of liver enzymes (Qu et al. 2014). In context of renal function, increased interstitial expression of α-SMA is associated with reduced renal function in patients with glomerulonephritis, an illness which can lead to fibrosis development and CKD (Novakovic et al. 2012). Combining this evidence, a measurement of creatinine levels and other uremic markers in the DSS-treated UUO mice to generate a relation between α-SMA expression and renal function would further enhance the clinical relevance of the presented results. A further example describes the rt-PCR-quantified downregulation of Col1 expression in DSS-treated cardiac fibroblasts after isoproterenol-induced fibrosis (Lu et al. 2014). Further organ responses have been evaluated after treatment with other or combined Salvia miltiorrhizae extracts, including salvianolic acid B, but not with purified DSS extract. However, as salvianolic acid B contains prominent biochemical similarities to DSS, including the phenol group responsible for the antioxidant activity, similar effects between the two substances have been observed and parallels between them may be drawn (Zhao et al. 2008). Combined Salvia miltiorrhizae components including salvianolic acid B and DSS demonstrate a reduction of α-SMA and Col1 expression in Western blot in a study on vascular remodeling and oxidative stress in spontaneously hypertensive rats (Zhang et al. 2016). While evidence of the beneficial influence of DSS on heart, liver, and vessels have hereby been shown, one major report evaluates

the effect of a combined Salvia miltiorrhizae injection, including a prominent proportion of DSS, on fibrosis development in a model of diabetic nephropathy in rats, revealing a significant reduction of Col1 in Masson trichrome staining in the fibrotic area of the kidney after DSS treatment (Xu et al. 2016). Combined, the mentioned studies provide evidence of a wide application range for DSS treatment and support the results presented here in the *in-vivo* UUO mouse model.

As in the *in-vitro* model, the matter regarding the action mode of DSS resulting in Col1 and α-SMA reduction is in its entirety still unanswered. Recently, an in-depth proteomics study contributed to answering this question through an *in-vivo* rat model undergoing an induced myocardial infarction and treated with DSS: Proteome microarray and metabolomic profiling identified hydrolases, transferases, and enzyme modulators to be the main DSS-bound protein classes, and potential metabolite biomarkers of myocardial infarction also influenced by DSS were primarily related to phospholipid, lipid, and fatty acid metabolism. (Jia et al. 2019). As these metabolic pathways are relevant sources of ROS synthesis, linking the antioxidant effect of DSS to these pathways seems plausible. Regarding the concrete signaling pathways involved, studies have expressed varying possibilities such as the JAK/STAT pathway explaining the beneficial effect of DSS on hepatofibrosis (Qu et al. 2014), confirmed recently by Cao et al. (2019). Many studies focus on the TGF-β pathway as the primary pathway defining DSS activity, supporting the results of this study demonstrating a significant reduction of pSmad2 in UUO renal tissue after DSS treatment. As an important pathway involved in the pathogenesis of renal fibrosis, the TGF-β pathway also lies in the focus as central mediator of α-SMA and Col1 synthesis, so that its inhibition would further explain the downregulation of these proteins under DSS influence (Meng et al. 2015). The effect of DSS on the TGF-β pathway has been analyzed in other organs, while the effect on renal tissue remains comparatively unclear. Based on the effect of DSS on arterial endothelium, it has the potential to reduce TGF-β activation and SMAD expression (Zhang et al. 2018). Furthermore, the effect of salvianolic acid B on the TGF-β pathway in a model of $HgCl_2$-induced renal interstitial fibrosis was analyzed. Similarly, not only α-SMA but also TGF-β and pSMAD2 are significantly downregulated in comparison to control (Wang et al. 2010). Regarding the clinical relevance of DSS treatment, one current report shows that a significant reduction of TGF-β in an *in-vivo* model of hypoxic pulmonary hypertension is only achieved through preventative DSS treatment, and not as post-diagnostic treatment; once TGF-β has been induced, the levels are reduced through DSS, but do not return to normal (Liu et al. 2020). Transferring these findings to CKD using the UUO model, an *in-vivo* study comparing the effect of DSS on TGF-β levels in early-stage and late-stage kidney failure would further categorize the relevance of DSS in a clinical setting.

The results of this study illustrate an antifibrotic effect of DSS with downregulation of α-Sma and Col1 in mouse renal tissue corresponding with a reduction of tubular damage, most likely mediated through inhibition of the TGF-β signaling pathway as demonstrated through the reduction of pSmad2 nuclear translocation. Further studies could supply additional data quantifying the clinical relevance of these proteome changes and assess the true prospects of DSS as a treatment for renal fibrosis in humans.

5 Summary

The purpose of this study is to examine a promising candidate, DSS, as treatment opportunity of chronic kidney disease (CKD) and its precursor stages. The focus lays on understanding the influence of DSS on pathogenetic processes of renal fibrosis and investigating the potential effect of DSS on renal fibrosis progression. Thus, the effect of DSS on TK173 kidney fibroblasts (*in-vitro*) stressed by ROS, as a contributing cause of oxidative stress and fibrosis, and on mouse kidneys with UUO-induced fibrosis (*in-vivo*) was analyzed.

DSS treatment increased TK173 cell viability and improved cell viability after exposure to H_2O_2-induced oxidative stress, as shown in the MTT cell viability assay. Correspondingly, FACS quantification of DCF-marked ROS showed a reduction of intracellular oxidative stress under DSS treatment. As an important protein in the cellular first line of defense against oxidative stress, SOD1 expression was analyzed in Western blot, revealing upregulation after DSS treatment. Expression of ECM proteins FN1 and VIM was also increased under DSS. In the *in-vivo* UUO mouse model, DSS treatment resulted in a downregulation of the TGF-β pathway, determined indirectly through the reduction of nuclear pSmad2 localization in immunohistochemical staining. Furthermore, α-Sma and Col1 expressions were significantly downregulated in the renal tissue as a sign of fibrosis attenuation, complementing the reduction of tubular damage analyzed in PAS tissue stains.

These observations are supported through data confirming effects of DSS in other models and organs. This study proves that DSS rescues renal cell lines from oxidative stress through reduction of intracellular ROS and upregulation of SOD1 expression. Through its indirect effect on the expression of ECM proteins α-Sma and Col1, DSS has a beneficial effect on fibrosis progression *in-vivo*. In context with the downregulation of pSmad2 under DSS treatment, these results provide evidence that DSS triggers the inhibition of the TGF-β pathway and its downstream regulation of prominent ECM proteins. In contrast, the fibrosis marker proteins such as VIM are upregulated *in-vitro* and thus support the cytoprotective effect of proteins in renal cells as recently shown in the case of VIM. These results demonstrate the complexity of the pathogenesis of renal fibrosis and prove the need for further research to clarify the role of the contrarily acting ECM proteins. However, the positive effects seen in the UUO model treated with DSS allows the hope of establishing DSS as a treatment opportunity for CKD caused by urinary obstruction as a feared complication in children and by other causes of renal fibrosis such as the common lifestyle diseases in adults.

6 References

Amann K, Haas CS (2006): What you should know about the work-up of a renal biopsy. Nephrol Dial Transplant 21, 1157–1161

Ameziane-El-Hassani R, Dupuy C (2013): Detection of Intracellular Reactive Oxygen Species (CM-H2DCFDA). Bio Protoc 3, e313

Bass JJ, Wilkinson DJ, Rankin D, Phillips BE, Szewczyk NJ, Smith K, Atherton PJ (2017): An overview of technical considerations for Western blotting applications to physiological research. Scand J Med Sci Sports 27, 4–25

Betz B, Conway BR (2016): An Update on the Use of Animal Models in Diabetic Nephropathy Research. Curr Diab Rep 16, 18

Bidani AK, Griffin KA (2004): Pathophysiology of hypertensive renal damage: implications for therapy. Hypertension 44, 595–601

Biernacka A, Dobaczewski M, Frangogiannis NG (2011): TGF-β signaling in fibrosis. Growth Factors 29, 196–202

Bladier C, Wolvetang EJ, Hutchinson P, Haan JB de, Kola I (1997): Response of a primary human fibroblast cell line to H2O2: senescence-like growth arrest or apoptosis? Cell Growth Differ 8, 589–598

Bradford MM (1976): A rapid and sensitive method for the quantitation of microgram quantities of protein utilizing the principle of protein-dye binding. Anal Biochem 72, 248–254

Branton MH, Kopp JB (1999): TGF-β and fibrosis. Microbes Infect 1, 1349–1365

Brunelle JL, Green R (2014): One-dimensional SDS-polyacrylamide gel electrophoresis (1D SDS-PAGE). Methods Enzymol 541, 151–159

Buchmaier BS, Bibi A, Müller GA, Dihazi GH, Eltoweissy M, Kruegel J, Dihazi H (2013): Renal Cells Express Different Forms of Vimentin: The Independent Expression Alteration of these Forms is Important in Cell Resistance to Osmotic Stress and Apoptosis. PLoS ONE 8, e68301

Cao G, Zhu R, Jiang T, Tang D, Kwan HY, Su T (2019): Danshensu, a novel indoleamine 2,3-dioxygenase1 inhibitor, exerts anti-hepatic fibrosis effects via inhibition of JAK2-STAT3 signaling. Phytomedicine 63, 153055

Chan K, Chui SH, Wong DYL, Ha WY, Chan CL, Wong RNS (2004): Protective effects of Danshensu from the aqueous extract of Salvia miltiorrhiza (Danshen) against homocysteine-induced endothelial dysfunction. Life Sci 75, 3157–3171

Chen X, Zhong Z, Xu Z, Chen L, Wang Y (2010): 2',7'-Dichlorodihydrofluorescein as a fluorescent probe for reactive oxygen species measurement: Forty years of application and controversy. Free Radic Res 44, 587–604

Chevalier RL (2006): Pathogenesis of renal injury in obstructive uropathy. Curr Opin Pediatr 18, 153–160

Chevalier RL, Forbes MS, Thornhill BA (2009): Ureteral obstruction as a model of renal interstitial fibrosis and obstructive nephropathy. Kidney Int 75, 1145–1152

Cohen T, Loutochin O, Amin M, Capolicchio JP, Goodyer P, Jednak R (2007): PAX2 is reactivated in urinary tract obstruction and partially protects collecting duct cells from programmed cell death. Am J Physiol Renal Physiol 292, F1267-73

Dell'Orco M, Milani P, Arrigoni L, Pansarasa O, Sardone V, Maffioli E, Polveraccio F, Bordoni M, Diamanti L, Ceroni M et al. (2016): Hydrogen peroxide-mediated induction of SOD1 gene transcription is independent from Nrf2 in a cellular model of neurodegeneration. Biochim Biophys Acta 1859, 315–323

Dihazi H, Dihazi GH, Mueller C, Lahrichi L, Asif AR, Bibi A, Eltoweissy M, Vasko R, Mueller GA (2011): Proteomics characterization of cell model with renal fibrosis phenotype: osmotic stress as fibrosis triggering factor. J Proteomics 74, 304–318

Eltoweissy M, Müller GA, Bibi A, van Nguye P, Dihazi GH, Müller CA, Dihazi H (2011): Proteomics analysis identifies PARK7 as an important player for renal cell resistance and survival under oxidative stress. Mol Biosyst 7, 1277–1288

Eriksson JE, Dechat T, Grin B, Helfand B, Mendez M, Pallari H-M, Goldman RD (2009): Introducing intermediate filaments: from discovery to disease. J Clin Invest 119, 1763–1771

Finnson KW, Almadani Y, Philip A (2020): Non-canonical (non-SMAD2/3) TGF-β signaling in fibrosis: Mechanisms and targets. Semin Cell Dev Biol 101, 115–122

Fitzgibbons PL, Goldsmith JD, Souers RJ, Fatheree LA, Volmar KE, Stuart LN, Nowak JA, Astles JR, Nakhleh RE (2017): Analytic Validation of Immunohistochemical Assays: A Comparison of Laboratory Practices Before and After Introduction of an Evidence-Based Guideline. Arch Pathol Lab Med 141, 1247–1254

Fox JG, Davisson MT, Quimby FW, Barthold SW, Newcomer CE, Smith AL (eds.) (2007): The mouse in biomedical research (American college of laboratory animal medicine series), 2nd edition; Elsevier Academic Press, Amsterdam 2007

Gao F, Wang Y, Li S, Wang Z, Liu C, Sun D (2016): Inhibition of p38 mitogen-activated protein kinases attenuates renal interstitial fibrosis in a murine unilateral ureteral occlusion model. Life Sci 167, 78–84

Genovese F, Manresa AA, Leeming DJ, Karsdal MA, Boor P (2014): The extracellular matrix in the kidney: a source of novel non-invasive biomarkers of kidney fibrosis? Fibrogenesis Tissue Repair 7, 4

Ghosh R, Gilda JE, Gomes AV (2014): The necessity of and strategies for improving confidence in the accuracy of western blots. Expert Rev Proteomics 11, 549–560

Guan S, Ma J, Zhang Y, Gao Y, Zhang Y, Zhang X, Wang N, Xie Y, Wang J, Zhang J et al. (2013): Danshen (Salvia miltiorrhiza) injection suppresses kidney injury induced by iron overload in mice. PLoS ONE 8, e74318

Guan Y, Wu XX, Duan JL, Yin Y, Guo C, Wei G, Wang YH, Zhu YR, Weng Y, Xi MM et al. (2015): Effects and Mechanism of Combination of Rhein and Danshensu in the Treatment of Chronic Kidney Disease. Am J Chin Med 43, 1381–1400

Gueutin V, Deray G, Isnard-Bagnis C (2012): Physiologie rénale. Bull Cancer 99, 237–249

Gutiérrez-Uzquiza Á, Arechederra M, Bragado P, Aguirre-Ghiso JA, Porras A (2012): p38α mediates cell survival in response to oxidative stress via induction of antioxidant genes: effect on the p70S6K pathway. J Biol Chem 287, 2632–2642

Haugen E, Nath KA (1999): The involvement of oxidative stress in the progression of renal injury. Blood Purif 17, 58–65

Hayden MS, Ghosh S (2004): Signaling to NF-κB. Genes Dev. 18, 2195–2224

He F, Fan M, Jin Y, Wang H, Ding L, Fan J, Gu S, Xu W (2019): Sphingosine kinase 1 inhibition decreases the epithelial-mesenchymal transition and ameliorates renal fibrosis via modulating NF-κB signaling. Am J Transl Res 11, 5879–5887

Hill NR, Fatoba ST, Oke JL, Hirst JA, O'Callaghan CA, Lasserson DS, Hobbs FDR (2016): Global Prevalence of Chronic Kidney Disease - A Systematic Review and Meta-Analysis. PLoS ONE 11, e0158765

Hitomi H, Kiyomoto H, Nishiyama A (2007): Angiotensin II and oxidative stress. Curr Opin Cardiol 22, 311–315

Hu T, Wei G, Xi M, Yan J, Wu X, Wang Y, Zhu Y, Wang C, Wen A (2016): Synergistic cardioprotective effects of Danshensu and hydroxysafflor yellow A against myocardial ischemia-reperfusion injury are mediated through the Akt/Nrf2/HO-1 pathway. Int J Mol Med 38, 83–94

Ighodaro OM, Akinloye OA (2018): First line defence antioxidants-superoxide dismutase (SOD), catalase (CAT) and glutathione peroxidase (GPX): Their fundamental role in the entire antioxidant defence grid. Alexandria Journal of Medicine 54, 287–293

Jaramillo MC, Zhang DD (2013): The emerging role of the Nrf2-Keap1 signaling pathway in cancer. Genes Dev. 27, 2179–2191

Jha V, Garcia-Garcia G, Iseki K, Li Z, Naicker S, Plattner B, Saran R, Wang AYM, Yang CW (2013): Chronic kidney disease: global dimension and perspectives. The Lancet 382, 260–272

Jia D, Xiong L, Yu X, Chen X, Wang T, Chen AF, Chai Y, Zhu Z, Zhang C (2019): Cardioprotective mechanism study of salvianic acid A sodium based on a proteome microarray approach and metabolomic profiling of rat serum after myocardial infarction. Mol Omics 15, 271–279

Kalyanaraman B, Darley-Usmar V, Davies KJA, Dennery PA, Forman HJ, Grisham MB, Mann GE, Moore K, Roberts LJ, Ischiropoulos H (2012): Measuring reactive oxygen and nitrogen species with fluorescent probes: challenges and limitations. Free Radic Biol Med 52, 1–6

Kaur G, Dufour JM (2012): Cell lines: Valuable tools or useless artifacts. Spermatogenesis 2, 1–5

Ketteler M, Block GA, Evenepoel P, Fukagawa M, Herzog CA, McCann L, Moe SM, Shroff R, Tonelli MA, Toussaint ND et al. (2017): Executive summary of the 2017 KDIGO Chronic Kidney Disease-Mineral and Bone Disorder (CKD-MBD) Guideline Update: what's changed and why it matters. Kidney Int 92, 26–36

Khan S, Amedia CA (2008): Economic burden of chronic kidney disease. J Eval Clin Pract 14, 422–434

Kristiansen KA, Jensen PE, Møller IM, Schulz A (2009): Monitoring reactive oxygen species formation and localisation in living cells by use of the fluorescent probe CM-H(2)DCFDA and confocal laser microscopy. Physiol Plant 136, 369–383

Kyriakis JM, Avruch J (2012): Mammalian MAPK signal transduction pathways activated by stress and inflammation: a 10-year update. Physiol Rev 92, 689–737

Levey AS, Coresh J, Balk E, Kausz AT, Levin A, Steffes MW, Hogg RJ, Perrone RD, Lau J, Eknoyan G (2003): National Kidney Foundation Practice Guidelines for Chronic Kidney Disease: Evaluation, Classification, and Stratification. Ann Intern Med 139, 137

Li GH, Li YR, Jiao P, Zhao Y, Hu HX, Lou HX, Shen T (2018): Therapeutic Potential of Salviae Miltiorrhizae Radix et Rhizoma against Human Diseases Based on Activation of Nrf2-Mediated Antioxidant Defense System: Bioactive Constituents and Mechanism of Action. Oxid Med Cell Longev 2018, 1–13

Li H, Song F, Duan LR, Sheng JJ, Xie YH, Yang Q, Chen Y, Dong QQ, Le Zhang B, Wang SW (2016): Paeonol and danshensu combination attenuates apoptosis in myocardial infarcted rats by inhibiting oxidative stress: Roles of Nrf2/HO-1 and PI3K/Akt pathway. Sci Rep 6, 23693

Liu G, Zhang Q, Zhang J, Zhang N (2020): Preventive but nontherapeutic effect of danshensu on hypoxic pulmonary hypertension. J Int Med Res 48, 1-8

Liu RM, Desai LP (2015): Reciprocal regulation of TGF-β and reactive oxygen species: A perverse cycle for fibrosis. Redox Biol 6, 565–577

Liu T, Zhang L, Joo D, Sun SC (2017): NF-ϰB signaling in inflammation. Signal Transduct Target Ther 2, e17023

Liu Y (2006): Renal fibrosis: new insights into the pathogenesis and therapeutics. Kidney Int 69, 213–217

Liu Y (2011): Cellular and molecular mechanisms of renal fibrosis. Nat Rev Nephrol 7, 684–696

Lu H, Tian A, Wu J, Yang C, Xing R, Jia P, Yang L, Zhang Y, Zheng X, Li Z (2014): Danshensu Inhibits β-Adrenergic Receptors-Mediated Cardiac Fibrosis by ROS/p38 MAPK Axis. Biol Pharm Bull 37, 961–967

Marjanovič I, Kandušer M, Miklavčič D, Keber MM, Pavlin M (2014): Comparison of flow cytometry, fluorescence microscopy and spectrofluorometry for analysis of gene electrotransfer efficiency. J Membr Biol 247, 1259–1267

Massagué J (2012): TGFβ signalling in context. Nat Rev Mol Cell Biol 13, 616

Mehring M, Donnachie E, Bonke FC, Werner C, Schneider A (2017): Disease management programs for patients with type 2 diabetes mellitus in Germany: a longitudinal population-based descriptive study. Diabetol Metab Syndr 9, 37

Meng XM, Tang PMK, Li J, Lan HY (2015): TGF-β/Smad signaling in renal fibrosis. Front Physiol 6, 82

Meran S, Steadman R (2011): Fibroblasts and myofibroblasts in renal fibrosis. Int J Exp Pathol 92, 158–167

Miao L, St Clair DK (2009): Regulation of superoxide dismutase genes: implications in disease. Free Radic Biol Med 47, 344–356

Mishra M, Tiwari S, Gomes AV (2017): Protein purification and analysis: next generation Western blotting techniques. Expert Rev Proteomics 14, 1037–1053

Montorfano I, Becerra A, Cerro R, Echeverría C, Sáez E, Morales MG, Fernández R, Cabello-Verrugio C, Simon F (2014): Oxidative stress mediates the conversion of endothelial cells into myofibroblasts via a TGF-β1 and TGF-β2-dependent pathway. Lab Invest 94, 1068–1082

Mosmann T (1983): Rapid colorimetric assay for cellular growth and survival: Application to proliferation and cytotoxicity assays. J Immunol Methods 65, 55–63

Moukarbel GV, Yu ZF, Dickstein K, Hou YR, Wittes JT, McMurray JJV, Pitt B, Zannad F, Pfeffer MA, Solomon SD (2014): The impact of kidney function on outcomes following high risk myocardial infarction: findings from 27 610 patients. Eur J Heart Fail 16, 289–299

Müller GA, Frank J, Rodemann HP, Engler-Blum G (1995): Human renal fibroblast cell lines (tFKIF and tNKF) are new tools to investigate pathophysiologic mechanisms of renal interstitial fibrosis. Exp Nephrol 3, 127–133

Nguyen HT, Kogan BA (1998): Upper urinary tract obstruction: experimental and clinical aspects. Br J Urol 81 Suppl 2, 13–21

Nie JM, Li HF (2018): Therapeutic effects of Salvia miltiorrhiza injection combined with telmisartan in patients with diabetic nephropathy by influencing collagen IV and fibronectin: A case-control study. Exp Ther Med 16, 3405–3412

Nogueira A, Pires MJ, Oliveira PA (2017): Pathophysiological Mechanisms of Renal Fibrosis: A Review of Animal Models and Therapeutic Strategies. In Vivo 31, 1–22

Novakovic ZS, Durdov MG, Puljak L, Saraga M, Ljutic D, Filipovic T, Pastar Z, Bendic A, Vukojevic K (2012): The interstitial expression of alpha-smooth muscle actin in glomerulonephritis is associated with renal function. Med Sci Monit 18, CR235-40

Okamura DM, Pennathur S (2015): The balance of powers: Redox regulation of fibrogenic pathways in kidney injury. Redox Biol 6, 495–504

Ozbek E (2012): Induction of oxidative stress in kidney. Int J Nephrol 2012, 465897

Pan C, Kumar C, Bohl S, Klingmueller U, Mann M (2009): Comparative proteomic phenotyping of cell lines and primary cells to assess preservation of cell type-specific functions. Mol Cell Proteomics 8, 443–450

Pang Y, Zhang PC, Lu RR, Li HL, Li JC, Fu HX, Cao YW, Fang GX, Liu BH, Wu JB et al. (2020): Andrade-Oliveira Salvianolic Acid B Modulates Caspase-1-Mediated Pyroptosis in Renal Ischemia-Reperfusion Injury via Nrf2 Pathway. Front Pharmacol 11, 541426

Pankov R, Yamada KM (2002): Fibronectin at a glance. J Cell Sci 115, 3861–3863

Parascandolo A, Laukkanen MO (2019): Carcinogenesis and Reactive Oxygen Species Signaling: Interaction of the NADPH Oxidase NOX1-5 and Superoxide Dismutase 1-3 Signal Transduction Pathways. Antioxid Redox Signal 30, 443–486

Pawlak K, Pawlak D, Mysliwiec M (2007): Impaired renal function and duration of dialysis therapy are associated with oxidative stress and proatherogenic cytokine levels in patients with end-stage renal disease. Clin Biochem 40, 81–85

Perlman RL (2016): Mouse models of human disease: An evolutionary perspective. Evol Med Public Health 2016, 170–176

Podkowińska A, Formanowicz D (2020): Chronic Kidney Disease as Oxidative Stress- and Inflammatory-Mediated Cardiovascular Disease. Antioxidants (Basel) 9, 752

Pohlers D, Brenmoehl J, Löffler I, Müller CK, Leipner C, Schultze-Mosgau S, Stallmach A, Kinne RW, Wolf G (2009): TGF-beta and fibrosis in different organs - molecular pathway imprints. Biochim Biophys Acta 1792, 746–756

Potts JR, Campbell ID (1996): Structure and function of fibronectin modules. Matrix Biol 15, 313–320

Präbst K, Engelhardt H, Ringgeler S, Hübner H (2017): Basic Colorimetric Proliferation Assays: MTT, WST, and Resazurin. Methods Mol Biol 1601, 1–17

Qu W, Huang H, Li K, Qin C (2014): Danshensu-mediated protective effect against hepatic fibrosis induced by carbon tetrachloride in rats. Pathol Biol 62, 348–353

Ratliff BB, Abdulmahdi W, Pawar R, Wolin MS (2016): Oxidant Mechanisms in Renal Injury and Disease. Antioxid Redox Signal 25, 119–146

Rojo AI, Salinas M, Martín D, Perona R, Cuadrado A (2004): Regulation of Cu/Zn-superoxide dismutase expression via the phosphatidylinositol 3 kinase/Akt pathway and nuclear factor-kappaB. J. Neurosci. 24, 7324–7334

Ruiz S, Pergola PE, Zager RA, Vaziri ND (2013): Targeting the transcription factor Nrf2 to ameliorate oxidative stress and inflammation in chronic kidney disease. Kidney Int 83, 1029–1041

Rydell-Törmänen K, Johnson JR (2019): The Applicability of Mouse Models to the Study of Human Disease. Methods Mol Biol 1940, 3–22

Sagoo MK, Gnudi L (2020): Diabetic Nephropathy: An Overview. Methods Mol Biol 2067, 3–7

Said A, Desai C, Lerma EV (2015): Chronic kidney disease. Dis Mon 61, 374–377

Saran R, Robinson B, Abbott KC, Bragg-Gresham J, Chen X, Gipson D, Gu H, Hirth RA, Hutton D, Jin Y et al. (2020): US Renal Data System 2019 Annual Data Report: Epidemiology of Kidney Disease in the United States. Am J Kidney Dis 75, A6-A7

Scott RP, Quaggin SE (2015): Review series: The cell biology of renal filtration. J Cell Biol 209, 199–210

Seikaly MG, Ho PL, Emmett L, Fine RN, Tejani A (2003): Chronic renal insufficiency in children: the 2001 Annual Report of the NAPRTCS. Pediatr Nephrol 18, 796–804

Steinert PM, Roop DR (1988): Molecular and cellular biology of intermediate filaments. Annu Rev Biochem 57, 593–625

Tampe B, Steinle U, Tampe D, Carstens JL, Korsten P, Zeisberg EM, Müller GA, Kalluri R, Zeisberg M (2017): Low-dose hydralazine prevents fibrosis in a murine model of acute kidney injury-to-chronic kidney disease progression. Kidney Int 91, 157–176

Towbin H, Staehelin T, Gordon J (1979): Electrophoretic transfer of proteins from polyacrylamide gels to nitrocellulose sheets: procedure and some applications. Proc Natl Acad Sci U S A 76, 4350–4354

Tsang CK, Liu Y, Thomas J, Zhang Y, Zheng XFS (2014): Superoxide dismutase 1 acts as a nuclear transcription factor to regulate oxidative stress resistance. Nat Commun 5, 3446

United States Renal Data System (2019): Chapter 5: Mortality. American Journal of Kidney Diseases 73, S411-S426

van Meerloo J, Kaspers GJL, Cloos J (2011): Cell sensitivity assays: the MTT assay. Methods Mol Biol 731, 237–245

van Tonder A, Joubert AM, Cromarty AD (2015): Limitations of the 3-(4,5-dimethylthiazol-2-yl)-2,5-diphenyl-2H-tetrazolium bromide (MTT) assay when compared to three commonly used cell enumeration assays. BMC Res Notes 8, 47

Vaughan ED, Marion D, Poppas DP, Felsen D (2004): Pathophysiology of unilateral ureteral obstruction: studies from Charlottesville to New York. J Urol 172, 2563–2569

Wang H, Naghavi M, Allen C, Barber RM, Bhutta ZA, Carter A, Casey DC, Charlson FJ, Chen AZ, Coates MM et al. (2016): Global, regional, and national life expectancy, all-cause mortality, and cause-specific mortality for 249 causes of death, 1980–2015: a systematic analysis for the Global Burden of Disease Study 2015. The Lancet 388, 1459–1544

Wang QL, Tao YY, Yuan JL, Shen L, Liu CH (2010): Salvianolic acid B prevents epithelial-to-mesenchymal transition through the TGF-beta1 signal transduction pathway in vivo and in vitro. BMC Cell Biol 11, 31

Wang T, Fu F, Han B, Zhang L, Zhang X (2012): Danshensu ameliorates the cognitive decline in streptozotocin-induced diabetic mice by attenuating advanced glycation end product-mediated neuroinflammation. J Neuroimmunol 245, 79–86

Wang Z, Divanyan A, Jourd'heuil FL, Goldman RD, Ridge KM, Jourd'heuil D, Lopez-Soler RI (2018): Vimentin expression is required for the development of EMT-related renal fibrosis following unilateral ureteral obstruction in mice. Am J Physiol Renal Physiol 315, F769-F780

Welch WJ, Feramisco JR, Blose SH (1985): The mammalian stress response and the cytoskeleton: alterations in intermediate filaments. Ann N Y Acad Sci 455, 57–67

Wu L, Hu X, Tang H, Han Z, Chen Y (2014): Valid application of western blotting. Mol Biol Rep 41, 3517–3520

Xiao Z, Liu W, Mu YP, Zhang H, Wang XN, Zhao CQ, Chen JM, Liu P (2020): Pharmacological Effects of Salvianolic Acid B Against Oxidative Damage. Front Pharmacol 11, 572373

Xu L, Shen P, Bi Y, Chen J, Xiao Z, Zhang X, Wang Z (2016): Danshen injection ameliorates STZ-induced diabetic nephropathy in association with suppression of oxidative stress, pro-inflammatory factors and fibrosis. Int Immunopharmacol 38, 385–394

Yang HC, Zuo Y, Fogo AB (2010): Models of chronic kidney disease. Drug Discov Today Dis Models 7, 13–19

Zeisberg M, Neilson EG (2010): Mechanisms of tubulointerstitial fibrosis. J Am Soc Nephrol 21, 1819–1834

Zhang H, Sun SC (2015): NF-κB in inflammation and renal diseases. Cell Biosci 5, e63

Zhang J, An SJ, Fu JQ, Liu P, Shao TM, Li M, Li X, Jiao Z, Chai XQ (2016): Mixed Aqueous Extract of Salvia Miltiorrhiza Reduces Blood Pressure through Inhibition of Vascular Remodelling and Oxidative Stress in Spontaneously Hypertensive Rats. Cell Physiol Biochem 40, 347–360

Zhang J, Zhang Q, Liu G, Zhang N (2019): Therapeutic potentials and mechanisms of the Chinese traditional medicine Danshensu. Eur J Pharmacol 864, 172710

Zhang N, Dong M, Luo Y, Zhao F, Li Y (2018): Danshensu prevents hypoxic pulmonary hypertension in rats by inhibiting the proliferation of pulmonary artery smooth muscle cells via TGF-β-smad3-associated pathway. Eur J Pharmacol 820, 1–7

Zhao GR, Zhang HM, Ye TX, Xiang ZJ, Yuan YJ, Guo ZX, Zhao LB (2008): Characterization of the radical scavenging and antioxidant activities of danshensu and salvianolic acid B. Food Chem Toxicol 46, 73–81

Zhou D, Liu Y (2016): Renal fibrosis in 2015: Understanding the mechanisms of kidney fibrosis. Nat Rev Nephrol 12, 68–70

Zhou G, Li C, Cai L (2004): Advanced Glycation End-Products Induce Connective Tissue Growth Factor-Mediated Renal Fibrosis Predominantly through Transforming Growth Factor β-Independent Pathway. Am J Pathol 165, 2033–2043

Zhou L, Zuo Z, Chow MSS (2005): Danshen: an overview of its chemistry, pharmacology, pharmacokinetics, and clinical use. J Clin Pharmacol 45, 1345–1359

Zhou X, Chan SW, Tseng HL, Deng Y, Hoi PM, Choi PS, Or PMY, Yang JM, Lam FFY, Lee SMY et al. (2012): Danshensu is the major marker for the antioxidant and vasorelaxation effects of Danshen (Salvia miltiorrhiza) water-extracts produced by different heat water-extractions. Phytomedicine 19, 1263–1269

Acknowledgements

First and foremost, I would like to extend my sincere thanks to my supervisor and mentor Dr. Hassan Dihazi. Ever since he opened his laboratory door to me, I was greeted with kind words and unwavering support. He created a comfortable atmosphere in the lab, making all of us feel welcome. Especially in the final phase, Hassan extended a great amount of assistance and gave me the needed push to ultimately complete the project. I also thank Prof. Dr. Michael Müller for his helpful advice throughout my research.

Furthermore, I cannot begin to express my thanks to Hanna Beißwenger. As my partner in the lab, she was always there to bounce ideas off of, to double-check my calculations, to lighten the mood with a smile and a laugh, or to comfort my frustration after a Western Blot-gone-bad.

Special thanks also go to Christina Decker, Elke Brunst-Knoblich, and Jens Mahrt for training me in my first weeks in the lab and for sticking by my side and sharing their experiences further on. I greatly appreciate the helpful and cooperative relationship we shared.

Frederike Weber and Ruben Plöger cannot be forgotten – thank you for your patience and unwavering support in all aspects.